

2015-08-06

Peptide-Capped Nanoparticles for Catalysis and Assembly

Beverly D. Briggs

University of Miami, bbriggs@umiami.edu

Follow this and additional works at: https://scholarlyrepository.miami.edu/oa_dissertations

Recommended Citation

Briggs, Beverly D., "Peptide-Capped Nanoparticles for Catalysis and Assembly" (2015). *Open Access Dissertations*. 1502.
https://scholarlyrepository.miami.edu/oa_dissertations/1502

This Open access is brought to you for free and open access by the Electronic Theses and Dissertations at Scholarly Repository. It has been accepted for inclusion in Open Access Dissertations by an authorized administrator of Scholarly Repository. For more information, please contact repository.library@miami.edu.

UNIVERSITY OF MIAMI

PEPTIDE-CAPPED NANOPARTICLES FOR CATALYSIS AND ASSEMBLY

By

Beverly D. Briggs

A DISSERTATION

Submitted to the Faculty
of the University of Miami
in partial fulfillment of the requirements for
the degree of Doctor of Philosophy

Coral Gables, Florida

August 2015

©2015
Beverly D. Briggs
All Rights Reserved

UNIVERSITY OF MIAMI

A dissertation submitted in partial fulfillment of
the requirements for the degree of
Doctor of Philosophy

PEPTIDE-CAPPED NANOPARTICLES FOR CATALYSIS AND ASSEMBLY

Beverly D. Briggs

Approved:

Marc R. Knecht, Ph.D.
Associate Professor of Chemistry

Roger LeBlanc, Ph.D.
Professor of Chemistry

Angel Kaifer, Ph.D.
Professor of Chemistry

Dean of the Graduate School

Onur Tigli, Ph.D.
Assistant Professor of Electrical-
Computer Engineering

BRIGGS, BEVERLY D.

(Ph.D., Chemistry)

Peptide-Capped Nanoparticles for Catalysis and Assembly

(August 2015)

Abstract of a dissertation at the University of Miami.

Dissertation supervised by Professor Marc R. Knecht

No. of pages in text. (187)

Nature possesses methods for the formation and manipulation of inorganic materials with controlled size, shape, and compositions. Biomolecules, such as peptides, are known to be responsible for the generation of such inorganic materials on the nanoscale, where the enhanced properties can be exploited for various applications. Pd nanoparticles, capped with the Pd-specific Pd4 peptide (TSNAVHPTLRHL), were found to be active catalysts for Stille coupling, where the debated mechanism of oxidative addition was explored. Furthermore, the same Pd4-capped nanoparticles were found to be active in Suzuki coupling, another C-C coupling reaction that undergoes catalysis following a similar mechanism. Other considerations with peptide-capped metal catalysis involved the role of the reductant and the subsequent effects on morphology and reactivity, as seen by use of Au nanoparticles capped with a library of peptides. The role of the reductant was studied using varied reductants and was found to directly affect the catalytic activity. Additionally, such Au and Ag materials-binding peptides were expanded to generate multi-domain biomolecules capable of metal-specific binding and nanoparticle assembly. Such in-depth studies of peptide-capped nanomaterials and their uses in catalysis and assembly is important for optimized functionality and application.

In loving memory of Don Jennings

Acknowledgements

As this chapter of my life comes to a close, I am overwhelmed with gratitude for all those who helped and supported me through this time.

First of all, I would like to thank my advisor, Dr. Marc Knecht, for guiding and mentoring me throughout my Ph.D. studies. Also I would like to acknowledge my committee members: Dr. Roger LeBlanc, Dr. Angel Kaifer and Dr. Onur Tigli for giving me their time and sharing their expertise. Furthermore, I would like to acknowledge our collaborators: Dr. Nicholas Bedford, Dr. Rajesh Naik, Dr. Frenkel Anatoly, Dr. Soenke Seifert, Dr. Tiffany Walsh and Dr. Mark Swihart for their invaluable contributions to my work. And specifically I would like to thank my lab members, past and present, for making the Knecht lab a great place to spend the last five years. I would like to especially thank Nick (Ginger) Merrill, who has been my sounding board and awesome friend, and Michelle Nguyen, who was always had a willing ear when I was feeling stressed.

Personally I am very blessed to have a huge amount of support from my large family. Thanks to my mom, Diane Jennings, for helping me to get to Miami and always encouraging me. Thanks to my bonus mom, Kristi Briggs, for sharing her experience and understanding my frustrations. Thanks to my dad, Lowell Briggs, for having complete faith in me and expecting nothing less than excellence. A very special thank you to James Penland, for listening to me day and night and motivating me to keep going. Also to his wonderful parents, David and Christine Outler - thank you for making me feel so supported. Finally, a tearful thank you to Don Jennings, who was always so excited and proud of me. I miss you every day.

TABLE OF CONTENTS

	Page
List of Figures.....	x
List of Tables.....	xiii
List of Abbreviations.....	xiv
Summary.....	1
Chapter 1: Introduction.....	5
1.1 Biocombinatorial Isolation of Materials Binding Peptides.....	5
1.2 Pd and Pt Noble Metals.....	6
1.3 Au and Ag Noble Metals.....	27
1.4 Metal Oxides.....	45
1.5 Catalytic Applications.....	54
1.5.1 Stille Coupling.....	54
1.5.2 Suzuki Coupling.....	55
1.5.3 Heck Coupling.....	56
1.5.3 4-Nitrophenol Reduction.....	57
1.6 Summary and Conclusions.....	58
Chapter 2: Atomic-Scale Identification of Pd Leaching in Nanoparticle Catalyzed C-C Coupling: Effects of Particle Surface Disorder.....	59

2.1 Overview of Study.....	59
2.2 Motivation.....	59
2.3 Methods.....	63
2.3.1 Materials.....	63
2.3.2 Peptide Synthesis.....	63
2.3.3 Particle Synthesis.....	64
2.3.4 Stille Coupling to Isolate Oxidative Addition.....	64
2.3.5 Standard Stille Coupling Reaction.....	64
2.3.6 Characterization.....	65
2.3.7 EXAFS.....	65
2.3.8 SAXS.....	66
2.3.9 Computational Analysis of Coordination Numbers.....	66
2.4 Results and Discussion.....	68
2.4.1 Pd Nanoparticle Synthesis.....	68
2.4.2 Isolation of Oxidative Addition Step.....	69
2.4.3 EXAFS Studies.....	71
2.4.4 SAXS Studies.....	78
2.5 Summary and Conclusions.....	81

Chapter 3: Examination of Transmetalation Pathways and Effects in Aqueous

Suzuki Coupling Using Biomimetic Pd Nanocatalysts.....	82
3.1 Overview of Study.....	82
3.2 Motivation.....	82

3.3 Methods.....	86
3.3.1 Chemicals.....	86
3.3.2 Peptide-Capped Nanoparticle Synthesis.....	87
3.3.3 Citrate-Capped Nanoparticle Synthesis.....	87
3.3.4 Suzuki Coupling.....	88
3.3.5 TOF Studies.....	89
3.3.6 Recycling Studies.....	89
3.3.7 Characterization.....	89
3.3.8 ¹¹ B NMR Experiments.....	90
3.4 Results and Discussion.....	90
3.5 Summary and Conclusions.....	108

Chapter 4: Reductant and Sequence Effects on the Morphology and Catalytic

Activity of Peptide-Capped Au Nanoparticles.....	110
4.1 Overview of Study.....	110
4.2 Motivation.....	110
4.3 Methods.....	115
4.3.1 Materials.....	115
4.3.2 Peptide Synthesis.....	115
4.3.3 Nanoparticle Synthesis.....	115
4.3.4 Characterization.....	116
4.3.5 4-Nitrophenol Reduction Reaction.....	116
4.4 Results and Discussion.....	117

4.4.1 Nanoparticle Synthesis and Characterization.....	117
4.4.2 Reduction of 4-Nitrophenol.....	128
4.5 Summary and Conclusions.....	135
Chapter 5: Towards a Modular Multimaterial Nanoparticle Synthesis and Assembly Strategy via Bionanocombinatorics: Effects of Bifunctional Peptides for Au and Ag Materials.....	
5.1 Overview of Study.....	137
5.2 Motivation.....	137
5.3 Methods.....	140
5.3.1 Materials.....	140
5.3.2 Peptide Synthesis.....	141
5.3.3 PARE Molecule Synthesis.....	141
5.3.4 QCM Binding Analysis.....	142
5.3.5 Nanoparticle Synthesis.....	142
5.3.6 Characterization.....	143
5.4 Results and Discussion.....	143
5.4.1 PARE Synthesis.....	143
5.4.2 Binding Quantification.....	145
5.4.3 Nanoparticle Synthesis.....	146
5.4.4 Multimaterial Nanostructures.....	151
5.5 Summary and Conclusions.....	161

Chapter 6: Additional Information.....	162
6.1 Supporting Information for Chapter 1.....	162
6.2 Supporting Information for Chapter 2.....	163
6.3 Supporting Information for Chapter 3.....	164
6.4 Supporting Information for Chapter 4.....	167
6.5 Supporting Information for Chapter 5.....	172
References.....	178

List of Figures

Figure 1.1 Schematic of approaches employed for phage display.....	5
Figure 1.2 TEM images of Pd nanoparticles made using the Q7 peptide.....	7
Figure 1.3 CN trends of Pd nanoparticles capped with Pd4, A6, All and A6,11 peptides.	14
Figure 1.4 TEM images of Pd nanomaterials generated with the R5 peptide.....	17
Figure 1.5 Electron microscopy images of the peptide bolaamphiphile hydrogel and with Pd nanoparticles.....	22
Figure 1.6 Approach used for the isolation of Pt facet-specific peptides T7 and S7.....	24
Figure 1.7 Chiroptical characterization of the FlgA3 binding to Au nanoparticles.....	29
Figure 1.8 Schematic depiction and TEM images of C ₁₂ -PEP _{Au} Au helices.....	31
Figure 1.9 Schematic depiction and TEM images of C ₆ -PEP _{Au} Au hollow nanospheres..	34
Figure 1.10 TEM analysis of Au ₃₀ and Au ₆₀ nanoparticle networks.....	38
Figure 1.11 TEM analysis of the curled Ag nanomaterials formed by the Ge8 peptide....	43
Figure 1.12 TEM images of cells with MBPp and MBP-AgBP2p with AgNO ₃	44
Figure 1.13 SEM and TEM analysis of BaTiO ₃ fabricated using peptides.....	53
Figure 1.14 Suggested mechanism of Stille coupling with nanoparticles.....	55
Figure 1.15 Typical mechanism for Heck coupling.....	56
Figure 2.1 TEM Characterization of peptide-capped Pd nanoparticles.....	68
Figure 2.2 Isolation of oxidative addition step using peptide-capped Pd nanoparticles....	69
Figure 2.3 EXAFS r-space analysis at the Pd k-edge.....	73

Figure 2.4 SAXS analysis.....	78
Figure 2.5 Schematic representation of Pd atom leaching Stille coupling mechanism.....	80
Figure 3.1 Characterization of Pd ⁴⁺ -capped Pd nanoparticles.....	91
Figure 3.2 Suzuki coupling analysis as a function of the base.....	93
Figure 3.3 ¹¹ B NMR of 0.1 M PhB(OH) ₂ over the range of base concentrations.....	99
Figure 3.4 Schematic representation of competing transmetalation pathways and associated equilibria.....	101
Figure 3.5 Analysis of Suzuki coupling using the citrate-capped Pd nanoparticles.....	104
Figure 4.1 UV-vis analysis of Au nanoparticle formation.....	118
Figure 4.2 TEM images of the Au nanoparticles prepared as a function of peptide passivant and reductant.....	120
Figure 4.3 Comparison of the rate of Au nanoparticle formation as measured via the growth of the plasmon band.....	125
Figure 4.4 Determination of activation energies (E_a) for the 4-nitrophenol reduction reaction catalyzed by the peptide-capped Au nanoparticles.....	129
Figure 4.5 Comparison of the pseudo-first order rate constants for the 4-nitrophenol reduction reaction for each of the peptide-capped Au nanoparticle catalyst..	131
Figure 5.1 Protocol for PARE and multimetallic nanoparticle synthesis.....	144
Figure 5.2 UV-vis spectra of PARE-capped monometallic nanoparticles.....	148
Figure 5.3 TEM images of the PARE-capped monometallic nanoparticles.....	149
Figure 5.4 UV-vis spectra of PARE-capped multimetallic assemblies.....	152
Figure 5.5 TEM images of the PARE-capped multimetallic assemblies.....	154

Figure 5.6 Dark-field TEM and EDS mapping of <i>cis</i> PARE (Ag, Au) assemblies.....	155
Figure 5.7 SAXS analysis of PARE assemblies at the 2 ratio.....	157
Figure 6.1 UV-vis analysis of the Pd ₄ -capped Pd nanoparticles before and after reduction.....	163
Figure 6.2 Biphenylcarboxylic acid product formation over time with all three bases....	164
Figure 6.3 Recycling analysis for Suzuki coupling.....	165
Figure 6.4 Graphical representation of product yield with varying base molarity and pH.....	165
Figure 6.5 Suzuki coupling studies varying the ratio of KOH and K ₃ PO ₄	166
Figure 6.6 Characterization of the citrate-capped Pd nanoparticles.....	166
Figure 6.7 Au nanoparticle particle sizing analysis histograms.....	167
Figure 6.8 SAED patterns for the peptide-capped Au nanoparticles.....	168
Figure 6.9 Calculated UV-vis spectra for AuBP1 and AuBP2-capped nanoparticles.....	168
Figure 6.10 Analysis of AuBP1 and AuBP2 with Au and no reductant.....	169
Figure 6.11 Control 4-nitrophenol reduction studies conducted using the peptide only..	169
Figure 6.12 UV-vis of first and last spectra from 4-nitrophenol reduction studies.....	170
Figure 6.13 <i>k</i> values obtained from recycling studies of 4-nitrophenol reduction.....	171
Figure 6.14 Dark-field TEM imaging and EDS mapping of <i>trans</i> PARE (Ag, Au).....	172
Figure 6.15 Dark-field TEM imaging and EDS mapping of <i>trans</i> PARE (Au, Ag).....	172
Figure 6.16 Dark-field TEM imaging and EDS mapping of <i>cis</i> PARE (Au, Ag).....	173
Figure 6.17 UV-vis spectra of no PARE control samples.....	173
Figure 6.18 TEM of no PARE control samples.....	174

Figure 6.19 SAXS analysis of no PARE control samples.....	175
Figure 6.20 UV-vis spectra of physical mixture control samples.....	176
Figure 6.21 TEM images of physical mixture control samples.....	176
Figure 6.22 SAXS analysis of physical mixture control samples.....	177

List of Tables

Table 1 CNs and bond lengths from EXAFS analysis.....	74
Table 2 Suzuki coupling reactions catalyzed by the Pd4-capped Pd nanoparticles.....	106
Table 3 Comparison of the activation energies for each NP catalyst.....	132
Table 4 Binding energies calculated from QCM studies using the PARE peptide.....	146
Table 5 Materials-directing peptides discussed in Chapter 1.....	162
Table 6 Solubility of 4-iodobenzoic acid in varying base concentrations.....	164

List of Abbreviations

Abbreviation	Definition
AFM	atomic force microscopy
ASAXS	anomalous small-angle x-ray scattering
C-C	carbon-carbon
CCD	charge coupled device
CD	circular dichroism
CN	coordination number
DCM	dichloromethane
DEN	dendrimer-encapsulated nanoparticle
DIPEA	<i>N,N</i> -diisopropylethylamine
DLS	dynamic light scattering
DMF	<i>N,N</i> -dimethylformamide
EDS	energy dispersive spectroscopy
EDT	1,2-ethanedithiol
EXAFS	extended x-ray absorption fine structure spectroscopy
FCC	face centered cubic
FE-SEM	field-emission scanning electron microscopy
Fmoc	9-fluorenylmethoxycarbonyl
FTIR	fourier transform infrared spectroscopy
GC	gas chromatography
HBTU	<i>N,N,N',N'</i> -tetramethyl- <i>O</i> -(1H-benzotriazol-1-yl)uronium hexafluorophosphate

HEPES	4-(2-hydroxyethyl)piperazine-1-ethanesulfonic acid
HOBt	hydroxybenzotriazole
HPLC	high performance liquid chromatography
HR-TEM	high resolution transmission electron microscopy
4-IBA	4-iodobenzoic acid
LMCT	ligand to metal charge transfer
LSPR	localized surface plasmon resonance
MALDI-TOF	matrix assisted laser desorption/ionization – time of flight
MAM	maleimide azobenzene maleimide
MS	mass spectroscopy
MSTFA	<i>N</i> -methyl- <i>N</i> -(trimethylsilyl)-trifluoroacetamide
NMR	nuclear magnetic resonance
NP	nanoparticle
NPN	nanoparticle network
PAMAM	polyamidoamine
PARE	peptide assembly responsive element
PDF	pair distribution function
PIPS	passivated implanted planar silicon
PMPI	<i>N</i> -(<i>p</i> -maleimidophenyl) isocyanate
QCM	quartz crystal microbalance
RMC	reverse Monte Carlo
SAED	selected area electron diffraction
SAXS	small angle x-ray scattering

TEAA	triethylammonium acetate
TEM	transmission electron microscopy
TFA	trifluoroacetic acid
TGA	thermogravimetric analysis
TIS	tri-isopropyl silane
TOF	turnover frequency
WANG	4-hydroxymethylphenoxy acetyl
XPS	x-ray photoelectron spectroscopy
XRD	x-ray diffraction

Summary

The main aim of my research is to probe the synthesis and applications of peptide-capped metal nanoparticles in detail. Peptides are known for their ability to control the size and morphology of inorganic materials at the nanoscale level, exploiting principles designed in nature. These peptides generally fabricate nanomaterials under ambient conditions where intricate interactions between the biomolecules and inorganic materials lead to precisely designed structures. The ability to mimic the formation of precise nanomaterials is highly desired as such materials could be employed in numerous applications such as catalysis, assembly, and sensing. Unfortunately, the population of naturally abundant peptides with affinity and specificity to inorganic materials is limited, thus methods have been developed to elucidate these peptides in the laboratory. **Chapter 1** discusses the most commonly used method, phage display, exploited to isolate peptide sequences with affinities to an inorganic material of choice. The chapter then continues on to discuss relevant materials-binding peptides and their varied applications.

Using phage display, the Pd-binding peptide Pd4 (TSNAVHPTLRHL) was isolated. The use of Pd4 as a capping agent for Pd nanoparticle synthesis yielded small, nearly-monodisperse nanoparticles synthesized under benign conditions. Modeling studies of the peptide interaction with the Pd surface suggested that the Pd4 passivates the metal through the histidines at the six and eleven positions. This is beneficial as it helps to control the size and limit aggregation of the nanoparticles while leaving the catalytic surface area exposed. Thus, the Pd4-capped Pd nanoparticles were employed in Stille C-C coupling. While active for catalysis across a variety of substrates, the mechanism of Stille coupling remains controversial. It is well accepted that there are three steps: oxidative addition,

transmetalation, and reductive elimination. The controversy lies in the oxidative addition step, where it is hotly debated whether nanoparticles undergo a leaching or surface-based mechanism. **Chapter 2** details an in-depth study of the oxidative addition step of Stille coupling using Extended X-ray Absorbance Fine Structure Spectroscopy (EXAFS) and Small-Angle X-ray Scattering (SAXS) to spectroscopically probe the structure of the nanoparticles during this controversial step, where evidence of a leaching mechanism was achieved.

A useful catalyst needs to be versatile in many reactions and in order to advance this capability, each reaction needs to be studied and optimized for that catalytic system. In this manner, Suzuki C-C coupling was next explored using the Pd₄-capped Pd nanoparticles. Suzuki coupling is very similar to Stille coupling, having a very similar mechanism, with the exception of using an organoboron compound for transmetalation over an organostannane complex. The use of Suzuki coupling results in the entire system (catalyst and reaction) being significantly more environmentally friendly; boron is less toxic than tin. Optimization of Suzuki coupling occurred through turnover frequency (TOF) studies varying the base concentration of three species: KOH, NaCO₃, and K₃PO₄, and through ¹¹B NMR studies. This work revealed a unique relationship with the strength of the base employed, as discussed in **Chapter 3**, where a stronger base was observed to disrupt the equilibria required to maximize product yield.

From the previous work discussed in **Chapter 1 and 2** on peptide-capped Pd nanoparticles, it was determined that the sequence of the peptide has substantial effects on the inorganic material morphology. It should be considered, though, that the capping agent

is not the only factor in shape development; the strength of the reductant plays a pivotal role as it is intimately involved in nanoparticle nucleation and growth. Previous studies have not explored the intertwined roles of the reductant and peptide-capping agent in a concise manner. One limitation, especially with Pd, is the lack of surface characterization methods for the *in situ* process. Thus, switching to Au nanoparticles, which are known to have distinct localized surface plasmon resonance (LSPR) bands in the visible region of the UV-vis spectrum, is a logical step. In **Chapter 4**, I discuss the study of Au nanoparticles capped with three different peptides: AuBP1 (WAGAKRLVLRRE), AuBP2 (WALRRIRRQSY), and Pd4. AuBP1 and AuBP2 were isolated for their affinity for Au while Pd4, as previously mentioned, was isolated to bind Pd. Additionally, three different reductants were used in the generation of these peptide-capped Au nanoparticles: NaBH₄, hydrazine, and ascorbic acid. From a thorough study of the LSPR formation and catalytic activity of the surface-based 4-nitrophenol reduction, the interplay between the reductant and peptide capping agent for the formation of the Au nanoparticles was elucidated.

Based upon the previously described studies, the ability of peptides to passivate nanoparticle surfaces and influence morphology and, subsequently, catalytic activity has been determined. While catalysis is a potential application for nanomaterials, not all inorganic metals are strongly catalytically active, thus other applications should be explored for use with materials-binding peptides. One such application is assembly, where in **Chapter 5**, I describe the synthesis of a two domain peptide linked through a photoresponsive molecule, where the assembly of the nanoparticles could potentially be influenced by an external stimulus. This new peptide, termed Peptide Assembly Responsive Element (PARE), is the combination of AuBP1 and AgBP1

(TGIFKSARAMRN), a peptide isolated for an affinity to Ag. The peptides are joined together through use of MAM, a maleimide-azobenzene-maleimide molecule, where the addition of cysteine to the peptides allows for easy attachment via maleimide-thiol coupling. **Chapter 5** details the formation of monometallic Au and Ag nanoparticles as well as multimetallic assemblies through the use of UV-vis, TEM, Quartz Crystal Microbalance (QCM), Energy Dispersion Spectroscopy (EDS), and SAXS analysis. The use of the PARE shows distinct Au and Ag nanoparticles, although the azobenzene linker does not appear to exert a high level of control over the assembly process. Nonetheless, this study represents the first step in combining peptides with externally actuable molecules for assembly applications.

Chapter 1. Introduction

1.1 Biocombinatorial Isolation of Materials Binding Peptides

Numerous naturally occurring peptides that bind to inorganic surfaces such as CaCO_4 and SiO_2 are present in the biosphere.¹⁻² These peptides can be used to generate inorganic nanomaterials of selected compositions in the laboratory;³⁻⁴ however, they are unable to fabricate materials of all compositions that are important for various applications. While these compositions are interesting, a complete set of peptides that bind to technologically important materials is not available in Nature. As a result, biocombinatorial methods have been developed to identify peptides that recognize non-natural materials compositions.² For the most part, phage display and cell surface display methods, shown in Figure 1.1,

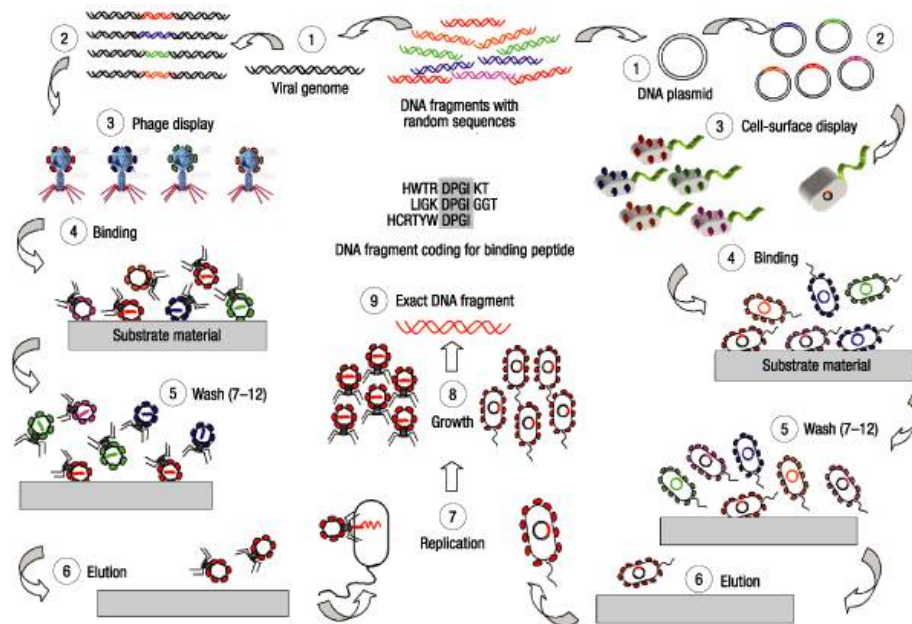


Figure 1.1. Approaches used for the biocombinatorial isolation of materials binding peptides. Reprinted by permission from Macmillan Publishers Ltd: Nature Materials, Sarikaya, M.; Tamerler, C.; Jen, A. K.-Y.; Schlten, K.; Baneyx, F. Molecular Biomimetics: Nanotechnology Through Biology. *Nat. Mater.* **2003**, *2*, 577-585, copyright 2003

have been employed to isolate novel peptides that bind additional inorganic materials.^{2, 5} Such approaches have been extensively used to isolate peptide sequences that recognize and bind both biological and non-biological species such as polystyrene, albumin, streptavidin, and biotin.⁶ These combinatorial methods employ peptide libraries that possess billions of individual sequences for target binding. For materials chemistry, the targets typically include inorganic compositions of interest for nanoparticle formation; however, this method can be applied to isolate peptides that recognize and bind species that can be supported on a solid surface. In a typical study, the library is added to the target, from which the phage or cells that specifically bind remain, while those that do not bind are washed from the system. The bound species are then released from the surface using an astringent wash and subsequently amplified. This process continues for multiple steps where the astringency of the elution step is increased to remove non-specific binders. After multiple elutions, the DNA of the phage or cells is harvested and sequenced to identify the peptides that recognize and bind the substrate. From this, a peptide library is identified that possesses increased binding strength for the material of interest. As a result, selective and tunable bioligand binding capabilities can potentially be achieved as a function of the peptide sequence.

1.2 Pd and Pt Noble Metals

Pd and Pt nanomaterials are attractive due to their wide range of applications including catalysis, energy storage, and gas sensing. By constraining the size of the materials on the nanoscale, optimization of the surface-to-volume ratio occurs to maximize the exposure of the catalytic materials for enhanced reactivity. Furthermore, different particle

morphologies can be used to alter the catalytic properties;⁷⁻⁸ the placement of the atoms in the nanomaterial structure, such as at edges or vertices, plays a key role in the application, and could potentially be tuned by the peptide binding event. Peptide-capped Pd nanoparticles are attractive for catalytic applications by adapting the materials for functionality at ambient conditions. Recently, a selection of Pd-binding peptides has been isolated to drive the production of Pd nanoparticles in water.^{5,9} For instance, Huang and coworkers have isolated the Q7 peptide (QQSWPIS) through phage display with affinity for Pd.¹⁰ Interestingly, the peptide acts as both a capping agent and as a reductant for nanoparticle formation. To confirm Pd nanoparticle formation, Pd²⁺ ions were reduced by NaBH₄ under three conditions: in the absence of peptide, in the presence of a nonspecific peptide (SLKLAYP), and in the presence of the Pd-specific Q7.

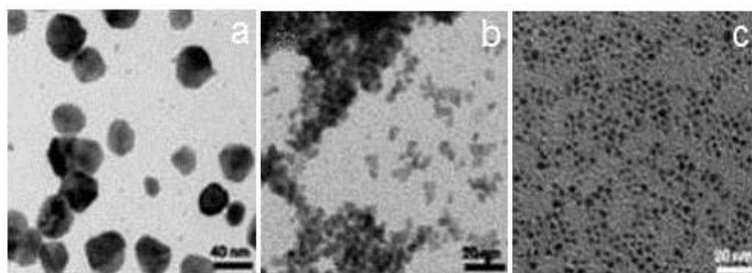


Figure 1.2. Parts (a-c) display TEM images of Pd nanoparticles using the Q7 peptide. Part (a) presents the materials formed in the absence of peptide (scale bar 40 nm), part (b) displays the Pd nanoparticles generated using a nonspecific peptide (scale bar 20 nm), while part (c) shows the particles capped with the Pd-specific Q7 peptide (scale bar 20 nm). (Reprinted with permission from Chiu, C.-Y.; Li, Y.; Huang, Y. Size-controlled Synthesis of Pd Nanocrystals Using a Specific Multifunctional Peptide. *Nanoscale*, **2010**, *2*, 927-930. - Reproduced by permission of The Royal Society of Chemistry (RSC).)

Transmission Electron Microscopy (TEM) images (Figure 1.2a) from the control reaction without peptide displayed irregular Pd nanoparticles with a large size of 36 ± 9 nm. Analysis of the materials prepared with the nonspecific peptide resulted in amorphous Pd

aggregates of poorly defined shape (Figure 1.2b); however, the materials generated using the Q7 peptide yielded well-dispersed Pd nanoparticles with a small size of 2.9 ± 0.4 nm (Figure 1.2c).¹⁰ This suggests that the surface specificity of the peptide is important in generating optimized nanoparticle structures, where the amino acids of the sequence control the binding capabilities.

Beyond surface binding, the Q7 peptide contains a tryptophan residue, which is known to reduce Ag and Au ions.¹¹ This capability could be exploited to control metal ion reduction and thus particle size to engender the peptide sequence with multiple functionalities. To ascertain this functionality with Pd, separate Pd²⁺ solutions were incubated with tryptophan, the Q7 peptide, and a control Q6 sequence. The Q6 peptide is based upon the Q7 sequence; however, the tryptophan residue is removed. Both the tryptophan and Q7-based solutions turned from the pale yellow color of the unreduced Pd²⁺ metal salt to dark brown, indicating metal ion reduction. No change in the solution color was observed for the Q6 reaction in the absence of tryptophan, suggesting its requirement for reduction capabilities.¹⁰ Further studies of the tryptophan and Q6 systems employing BH₄⁻ reduction for nanoparticle formation demonstrated changes in particle morphology as compared to the Q7. When using tryptophan as the capping agent, large aggregated Pd particles are observed; however, when employing the Q6 peptide, Pd nanoparticles were generated with a size of ~10 nm that eventually coalesced.¹⁰ Together, this indicates that the tryptophan residue is capable of reducing Pd²⁺ ions and is important for controlling the particle morphology and size, thus serving a dual role in materials fabrication.

Huang and colleagues further exploited the dual functionality of the Q7 sequence to control Pd nanoparticle size.¹⁰ Size tuning capabilities were achieved using a modified

seed-mediated nanoparticle synthesis approach. Here, a fraction of the Pd²⁺ ions in the reaction solution were reduced using NaBH₄ to form seeds from which the tryptophan residues of the peptide could reduce the additional Pd²⁺ ions. By controlling the Pd nanoparticle seed size as a function of the amount of reductant added, and the amount of additional Pd²⁺ ions, Pd nanoparticles of sizes between 2.6 nm and 6.6 nm could be readily prepared.¹⁰ The smallest sizes, 2.6 nm, represent the seeds from which tryptophan-based reduction was used to grow particles of up to 6.6 nm. Taken together, this multifunctional capability of the peptide to cap nanoparticle growth and finely tune the size of the materials is quite unique and difficult to achieve using non-specific ligands.

In addition to the septamer Q7 sequence, Pacardo *et al.* identified the dodecamer Pd4 sequence (TSNAVHPTLRHL) as having high affinity for Pd through phage display.¹² Extensive high-resolution characterization studies of the Pd4/Pd system have demonstrated that the sequence has strict control over the structure of the materials, as well as their catalytic functionality. The Pd4 peptide is able to generate zerovalent Pd nanoparticles through reduction of Pd²⁺ ions in the presence of the peptide.¹² Spectroscopic analysis of the materials before and after reduction indicated that the coordination environment of the Pd²⁺ to the peptide prior to NaBH₄ addition can affect the final Pd⁰ materials. As monitored via UV-vis analysis, titration of the Pd4 peptide with K₂PdCl₄ indicated that a maximum of 4 Pd²⁺ ions can coordinate to the peptide.¹³ This was observed via the formation of a Ligand to Metal Charge Transfer (LMCT) band that arises from complexation of the Pd²⁺ ions to the amines of the sequence. Imaging of the materials generated at Pd:peptide ratios of 1 – 4 demonstrated that particles of ~2 nm in diameter were generated for each sample, regardless of the metal concentration in the reaction. This unique result was surprising as

larger particles were anticipated from reactions with higher metal concentrations following standard nanoparticle nucleation and growth kinetics.¹⁴ This sizing event was suggested to arise from the crystallographic recognition capabilities of the Pd4 peptide for the face-centered cubic (fcc) Pd surface, which is likely achieved during the phage isolation process. Once the fcc structure is displayed, immediate peptide binding would occur to cap particle growth. Computational analysis of the Pd system indicated that stable fcc facets are presented by 2 nm particles, corresponding well with the experimental results.¹³

To further examine the Pd4 binding to the Pd particle surface, Extended X-ray Absorbance Fine Structure Spectroscopy (EXAFS) analysis was conducted of the peptide-capped materials prepared at Pd:peptide ratios of 1-4.¹³ EXAFS identified the presence of two different Pd materials in the sample corresponding to the presence of a mixture of Pd⁰ from the nanoparticles and Pd²⁺ from unreduced Pd²⁺/peptide complex. Furthermore, the fraction of Pd²⁺ ions that were reduced was directly proportional to the Pd:peptide ratio used to synthesize the materials.¹³ To that end, at the highest ratios, more Pd²⁺ was reduced to fabricate the nanoparticles, while at the lowest ratios, more Pd²⁺ remained unreduced and complexed to the peptide. While identical particles are generated in each sample regardless of the ratio employed, a higher fraction of the metal atoms became incorporated into the particles at higher ratios. This effect was likely due to the binding event of the Pd²⁺ ions to the peptide, which could shift the reduction potential based upon the degree of complexation. This indicates that the composition and morphology of the materials throughout the synthesis can have dramatic impacts on the structure and function of the final nanoparticles. As a result complete structural characterization at every step is necessary to optimize the individual system.

Further work using the nanoparticles synthesized with the Pd4 revealed high activity for use as catalysts in the Stille coupling reaction.^{12, 15-16} Pacardo *et al.* have proposed a leaching mechanism where a Pd atom is abstracted from the nanoparticle surface and utilized in the C-C coupling scheme.¹⁶ For this abstraction event to occur, the reagents must have unhindered access to the catalytic inorganic core of the materials. Theoretical modeling of the biotic/abiotic surface of the materials indicates that the histidines of the Pd4 sequence have the highest affinity for Pd.⁹ To that end, this binding creates a loop like structure on the particle surface to expose the reactive materials. The mechanism was supported by Quartz Crystal Microbalance (QCM) analysis, where Pd mass loss was monitored in the presence of 4-iodobenzoic acid.¹⁶ This suggests that the site-specific binding of the histidines to the Pd nanoparticle surface occurs, which exposes the Pd core for catalytic functionality.

Studies on Stille coupling using the Pd4-capped Pd nanoparticles were continued by Knecht and group, where substrate selectivity effects were explored as a function of both halogen and temperature.¹⁷ It was shown that brominated substrates were active for Stille coupling using the peptide-capped catalysts, but an increase in temperature to 40 °C was required. At this increased temperature, reactivity was found to be equal for iodo- and bromo-substituted aryl halides.¹⁷ Furthermore, a level of intramolecular selectivity was revealed when employing di-substituted substrates (*i.e.* 3-bromo-5-iodobenzoic acid) where an activating effect occurred such that full conversion could be seen with the less active bromine at room temperature when the other halogen was iodine.¹⁷

The specific role of the amino acids in the Pd4 binding sequence (TSNAVHPTLRHL) was studied more in depth by altering the peptide. Coppage *et al.* modified the sequence

by selectively interchanging the histidines at the 6 and 11 positions with nonpolar alanine residues, which is anticipated to alter the binding motif of the sequence. Three new peptides were formed where the histidine at position six was exchanged to create the A6 peptide, the histidine at position eleven was exchanged to create the A11 sequence, and both histidines were exchanged to create the A6,11 peptide.¹⁵ Surprisingly, the spherical Pd nanoparticles that resulted from the three new peptide analogues were similar in size. TEM analysis revealed the diameters to be 2.2 ± 0.4 nm, 2.4 ± 0.5 nm and 3.7 ± 0.9 nm for A6-, A11- and A6,11-capped particles, respectively.¹⁵ TOF studies were subsequently conducted monitoring the Stille coupling reaction using these materials. From this analysis, values of 5224 ± 381 mol product $(\text{mol Pd} \times \text{h})^{-1}$, 1298 ± 107 mol product $(\text{mol Pd} \times \text{h})^{-1}$, and 361 ± 21 mol product $(\text{mol Pd} \times \text{h})^{-1}$ resulted from the particles prepared by the A6, A11 and A6,11 peptides, respectively. These values can be directly compared to the TOF observed employing the Pd₄-based particles, which demonstrated a value of 2234 ± 99 mol product $(\text{mol Pd} \times \text{h})^{-1}$. This suggests that while the histidine residues are important for particle binding, removing these residues does not prevent the fabrication of stable nanoparticles; should this binding motif be removed, additional residues of the sequence, such as asparagine and arginine, can become more intimately involved in particle binding. Such changes, however, are anticipated to substantially alter the peptide structure once bound on the nanoparticle surface, which is likely to affect the catalytic activity. By modifying the surface peptide structure, changes to the biotic/abiotic interface are anticipated, which could substantially influence the ability for Pd atoms to be leached and participate in catalysis, thus changing the TOF values for the different materials. Indeed

changes in the Circular Dichroism (CD) spectra of the surface bound peptides and the TOF values were noted for comparison of the materials capped with the different peptides.

Further work by Coppage *et al.* on the Pd4 peptide and alanine analogs, which explored Pd nanoparticle formation across varying ratios of Pd:peptide, showed a specific binding behavior that controlled the size of the nanoparticle produced based upon which Pd4 mutant was used.¹⁸ With Pd4, a diameter of 1.9-2.1 nm was observed across the ratios, while with A6, the diameter increased to a range of 2.1-2.4 nm.¹⁸ Using A11, the nanoparticle size further increased to 2.3-2.6 nm.¹⁸ Finally with A6,11, the largest diameter range was observed at 2.8-3.1 nm, revealing a size increase based upon the number and location of the histidines in the peptide sequence.¹⁸ EXAFS studies revealed different levels of reduction as seen in the different coordination numbers (CN) that were determined for each analog across the Pd:peptide ratios (Figure 1.3).¹⁸ Previously with Pd4, it was observed that the CN for Pd-Pd increased as the Pd:peptide ratio increased, indicative of a greater amount of reduction.¹³ With the A6 peptide (Figure 1.3, green line), regardless of the amount of Pd²⁺ added, a Pd-Pd CN of ~6 was determined. Moving on to A11 (Figure 1.3, blue line), the CN for Pd-Pd varied further with no evident trend except that the values were the lowest noted across all Pd4 analogs.¹⁸ Interestingly with A6,11 (Figure 1.3, light blue line), the Pd-Pd CN was similar to that of the A6. Overall, this work with Pd4 and alanine analogs revealed a size selectivity based upon the peptide sequence as well as the ability to specifically change the coordination environment based upon these sequences.

Continuing the focus on specific residues in the Pd4 sequence, Knecht and group explored the changes to Pd nanoparticle formation by generating peptides where the

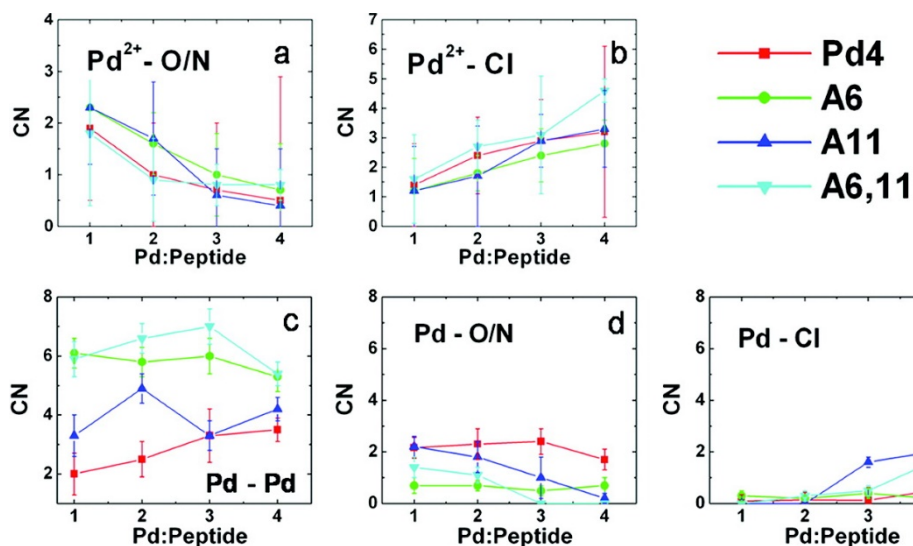


Figure 1.3. CN trends from EXAFS analysis for Pd4, A6, A11 and A6,11-capped Pd materials. Parts (a-b) shows the complexed materials while parts (c-e) show trends for reduced nanoparticles. Reprinted (adapted) with permission from Coppage, R.; Slocik, J. M.; Briggs, B. D.; Frenkel, A. I.; Naik, R. R.; Knecht, M. R. Determining Peptide Sequence Effects That Control the Size, Structure, and Function of Nanoparticles. *ACS Nano* **2012**, *6*, 1625-1636. Copyright 2012 American Chemical Society.

histidines in Pd4 were replaced by cysteines.¹⁹ In this manner, C6 (where cysteine replaced histidine at position 6), C11 (where cysteine replaced histidine at position 11) and C6,11 (where cysteines replaced histidines at positions 6 and 11) peptides were synthesized as well as A6C11 and C6A11 peptides, combining previous studies with alanine substitution with the new studies involving cysteine substitution. TEM analysis of Pd nanoparticles made using these analogs as the capping ligands and NaBH₄ as a reductant were explored to elucidate any size effects from the introduction of cysteines into the peptides.¹⁹ Interestingly, all nanoparticles with the cysteine in the peptide sequence have similar diameters, ranging from 2.2 – 2.4 nm. This is slightly increased from the native Pd4 peptide average of 2.0 ± 0.4 nm.¹³ The catalytic activity of these Pd nanoparticles was examined using Stille coupling as a model reaction. C11 and A6C11 materials were found to have the highest activity, yielding TOFs at 6138 ± 55 mol product (mol Pd × h)⁻¹ and 6097 ± 65

mol product (mol Pd \times h)⁻¹,¹⁹ respectively, which was a significant increase over the activity for materials with the native Pd4 peptide (2234 \pm 99 mol product (mol Pd \times h)⁻¹). C6, C11 and C6A11 also exhibited a higher activity for Stille coupling than Pd4, with TOFs of 3963 \pm 28 mol product (mol Pd \times h)⁻¹, 3974 \pm 280 mol product (mol Pd \times h)⁻¹, and 4147 \pm 340 mol product (mol Pd \times h)⁻¹, respectively.¹⁹ Along with modeling studies and QCM experiments, it was seen that replacing the histidine at position 11 with a strong binding residue such as cysteine and replacing the histidine at position 6 with a weak binding residue such as alanine could produce the highest activity.¹⁹ These sequence changes exemplify how simple modifications can be implemented to affect how the capping ligand binds to the surface and alters the reactivity.

Additional studies involving the Pd4 peptide were done by Janairo, *et al.* where the peptide was connected to 3D assembly controlling peptide to generate Pd nanoparticles with a specific supermolecular structure.²⁰ In this manner, Pd4 was fused to the N-terminus of the tetramerization domain of the tumor suppressor protein p53 (residues 324-358) with the aim of forming tetrahedron shapes.²⁰ The peptide was stabilized in HEPES buffer to which Pd²⁺ was added as well as an excess of NaBH₄ as a reductant. The resultant particles were amorphous, coral-like, branched structures with an average filament thickness of 104 \pm 21 nm.²⁰ It was postulated that the addition of the section of p53 to Pd4 limited the ability of Pd4 to generate the single-crystalline nanoparticles previously reported.¹² These coral-like nanoparticles were found to be active catalysts for the reduction of 2-, 3-, and 4-nitrophenol, yielding TOFs of 2390 \pm 440 h⁻¹, 6650 \pm 300 h⁻¹ and 6510 \pm 440 h⁻¹ respectively.²⁰ Overall this work exemplifies that peptides, such as Pd4, can be further

functionalized for additional uses without compromising the ability to generate nanoparticles, although the crystallinity may be affected.

While spherical nanoparticles typically possess property enhancement as compared to their bulk counterparts, altering the shape of the material can further alter these properties, as seen in the previously discussed study.²¹ This shape alteration is especially true for catalytic nanoparticles where non-spherical structures tend to have greater numbers of highly reactive defect atoms.⁷ Such capabilities have recently been observed using peptide-based methods,^{10, 22-27} where the R5 peptide (SSKKSGSYSKSKRRIL) has been shown to produce non-spherical materials of Pd.²² This peptide was isolated from the aquatic diatom *Cylindrotheca fusiformis* for the formation of silica.¹ Interestingly, the R5 is able to self-assemble via the C-terminal –RRIL motif, which generates large biological frameworks on the order of ~800 nm as observed via dynamic light scattering (DLS).²²⁻²³ These structures possess numerous free amine groups, which are well known to coordinate Pd²⁺ ions. In this sense, the peptide scaffold acts as a materials template by sequestering the metal within the structure via Pd²⁺/amine complexation. Using different Pd:peptide ratios during the synthesis, zerovalent materials of different shapes can be realized, including spheres, ribbons, and nanoparticles networks (NPNs).²² For instance, TEM characterization of the structures fabricated at a ratio of 60 (termed Pd60) demonstrated the formation of spherical Pd nanoparticles with a diameter of 2.9 ± 0.6 nm (Figure 1.4a). Analysis of the structures prepared at ratios of 90 (Pd90; Figure 1.4b) and 120 (Pd120; Figure 1.4c) yielded nanoribbons with an average width of 3.9 ± 0.8 nm and NPNs with average widths of 4.1 ± 1.2 nm, respectively.²³ These non-spherical particle morphologies likely develop due to the template-based synthesis. In this event, the Pd²⁺ ions are

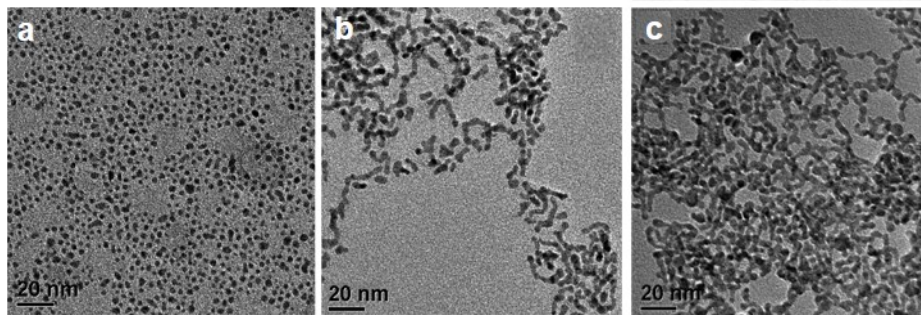


Figure 1.4. TEM images of the Pd nanomaterials generated using the template-based approach of the R5 peptide using Pd:peptide ratios of (a) 60, (b) 90, and (c) 120 (scale bar 20 nm). (Reprinted and adapted with permission from Bhandari, R.; Knecht, M. R., Effects of the Material Structure on the Catalytic Activity of Peptide-Templated Pd Nanomaterials. *ACS Catal.* **2011**, *1*, 89-98. Copyright 2011 American Chemical Society)

sequestered within the peptide framework that upon reduction begin to form nanoparticles at nucleation sites. At low Pd:peptide ratios, these nanoparticles are highly dispersed within the structure to prevent aggregation; however, as the ratio increases, the interparticle spacing decreases. Once this spacing is sufficiently diminished, the nanoparticles can aggregate in a linear fashion due to the peptide branches to form the nanoribbons and NPNs.²³ Under this mechanism, elongated structures with increased branching would be anticipated at higher Pd:peptide ratios, which is observed.

Catalytic testing of the differently shaped nanoparticles using both Stille coupling and the 4-nitrophenol reduction reaction demonstrated enhanced reactivity for the Pd60 nanospheres and Pd120 NPNs over the Pd90 nanoribbons.²²⁻²³ This differential reactivity was attributed to the structure of the composite materials where the catalytic surface area and reagent diffusion within the template control the functionality. For instance, for the Pd60 nanospheres, the largest metallic surface area is available; however, a higher degree of reagent diffusion is required to reach a catalytic site. These nanospheres had TOF values of 452 ± 16 mol product $(\text{mol Pd} \times \text{h})^{-1}$. For the Pd120 NPNs, while the catalytic surface

area decreases, the metallic structures are situated closer to the peptide/water interface to minimize reagent diffusion effects. The TOF values for the Pd120 NPNs were 437 ± 14 mol product $(\text{mol Pd} \times \text{h})^{-1}$. For both of these materials, one of the structural considerations is maximized; however, the Pd90 nanoribbons have a lower surface area as compared to the Pd60 particles and increased reagent diffusion as compared to the NPNs. As a result, diminished catalytic reactivity is observed for the nanoribbons on average as compared to the other structures. This is seen in lower TOF values of 334 ± 38 mol product $(\text{mol Pd} \times \text{h})^{-1}$.²²

Thereafter, the R5 peptide was used to fabricate Pt nanomaterials and Pd nanostructures for use in alcohol hydrogenation.²⁸ Similar protocols were followed, as previously described, where the amount of metal was varied at ratios of 60-120 versus the amount of R5. Interestingly, all Pt materials (Pt60-120) were spherical in nature with diameters averaging between 1.4 and 1.6 nm. This is drastically different from the structures seen from Pd where Pd60 yielded nanoparticles spherical in nature, Pd70-80 were elongated structures but not connected, Pd90-100 yielded nanoribbons, and nanoparticle networks were seen with Pd110-120.²⁸ The lack of morphological differences between Pt and Pd likely arises from the rate of reduction for Pt being slower, thus suggesting that the different structure formation can be controlled kinetically. Both sets of materials were further examined as catalysts for the conversion of allyl alcohol to 1-propanol. At a standard catalyst loading of 0.05 mol%, it was seen that the Pd materials (Pd60-120) all exhibited high activity for this hydrogenation, with TOF values ranging from 2860-3136 mol product $(\text{mol Pd} \times \text{h})^{-1}$.²⁸ These frequencies were approximately three fold that observed with the Pt materials (Pt60-120), which yielded a TOF range of 792-1202 mol product $(\text{mol Pt} \times \text{h})^{-1}$.

¹.²⁸ The differences in activity between Pt and Pd were suggested to arise from Pt being less active for the alcohol hydrogenation in general as well as a potential facilitation of the catalytic activity from the peptide framework acting as a scaffold for allyl alcohol to load into.²⁸

The study of R5-templated Pd materials for hydrogenation of small alcohols was broadened by Pacardo *et al.* where Pd60, Pd90 and Pd120 were used to study the effects of 2° and 3° alcohols in comparison to previously examined 1° alcohol, allyl alcohol.²⁹ For allyl alcohol, similar TOFs for hydrogenation compared to previous works²⁸ were observed of ~3000 mol product (mol Pd × h)⁻¹ for all three ratios.²⁹ Next, 2° alcohols were analyzed, starting with 3-buten-2-ol, where all three R5-templated materials yielded TOFs of ~3500 mol product (mol Pd × h)⁻¹. An additional 2° alcohol, 1-penten-3-ol, had similar results with TOFs of 3292 ± 298 mol product (mol Pd × h)⁻¹ for Pd60, 3328 ± 409 mol product (mol Pd × h)⁻¹ for Pd90 and 2632 ± 283 mol product (mol Pd × h)⁻¹ for Pd120.²⁹ Interestingly, the activity here was significantly lower for Pd120. Continuing with 3° alcohols, 2-methyl-3-buten-2-ol was first employed for hydrogenation with TOFs of 4892 ± 433 mol product (mol Pd × h)⁻¹ for Pd60, 4418 ± 763 mol product (mol Pd × h)⁻¹ for Pd90 and 4426 ± 1439 mol product (mol Pd × h)⁻¹ for Pd120.²⁹ Finally, the activity for 3-methyl-1-penten-3-ol was studied. Results equaled 3748 ± 469 mol product (mol Pd × h)⁻¹, 3912 ± 350 mol product (mol Pd × h)⁻¹, and 3256 ± 474 mol product (mol Pd × h)⁻¹ for Pd60, Pd90 and Pd120 respectively.²⁹ Collectively, these changes in alcohol structure revealed a general trend of increasing TOF with increasing alcohol order.

In that regard, competition studies were also conducted with R5-templated Pd60, Pd90 and Pd120 to explore the effects of two factors: substrate isomerization and molecular

size.²⁹ The TOFs were determined for studies comprised of solutions of allyl alcohol mixed with 4-penten-1-ol, 1-penten-3-ol or 3-methyl-1-penten-3-ol. The general trend of reactivity resulted in Pd60 retaining its activity, despite competition interactions, while yields were diminished with Pd90 and Pd120.²⁹ This was hypothesized to arise from curvature affects interfering with the interaction of the substrates with the metal surface, recalling that Pd60 particles were spherical in shape while Pd90 resulted in nanoribbons and Pd120 NPNs.²⁹ Interestingly, this work shows how material structure and substrate structure can both play a pivotal role in catalysis.

While the use of biomimetic peptides such as R5 work to exemplify nature in terms of self-assembling biomolecules, naturally-occurring biomolecules are typically attached to a larger molecule. In this way, Bedford *et al.* strived to mimic nature by creating a molecule in which the R5 peptide was covalently attached to a G4-PAMAM-OH dendrimer.³⁰ A cysteine was attached to the N-terminus of R5, leaving the C terminus sequence RRIL free to self-assemble in solution, as previously described. Using *N*-(*p*-maleimidophenyl) isocyanate (PMPI), the thiol on CR5 was then linked to the hydroxyl group of G4-PAMAM-OH to generate peptide-modified dendrimers. These hybrid molecules were created in ratios of R5:DEN of 4:1, 8:1 and 16:1 where infrared (IR) spectroscopy, fluorescence, and CD were used to verify attachment.³⁰ DLS studies were then conducted in which it was shown that the size of the fusion peptide, on average, decreased with increasing ratio. Pd was then added the CR5-DEN conjugates, reduced, and TEM imaged. In that manner, 16R5 (which is a ratio of R5:DEN of 16:1), was stable at Pd:16R5 ratios of 10, 30, and 60.³⁰ Similarly, 8R5 was found to be stable at ratios of Pd:8R5 at 30, 60, and 90, and 4R5 was found to be stable at Pd:R5 ratios of 60, 90, and 120.³⁰ Overall it was noted that the

morphology changed from particles to nanoparticle networks as the metal concentration increased, regardless of the CR5:DEN ratio employed. Furthermore, hydrogenation studies were conducted where all TOFs were approximately the same (but greater than R5 alone), ranging from 4100 ± 400 mol product $(\text{mol Pd} \times \text{h})^{-1}$ to 4800 ± 400 mol product $(\text{mol Pd} \times \text{h})^{-1}$. Overall, the studies using these fusion peptides suggested that the CR5:DEN conjugate was capable of enhancing activity by altering the spatial arrangement based upon changes to the R5 template.³⁰

Another study that explored the use of a self-assembling peptide system for the support of Pd nanoparticles was done by the Das group, where they generated a peptide bolaamphiphile through the combining of hydrophobic amino acid residues with hydrophilic groups at either end.³¹ The resulting peptide bolaamphiphile 1 (HO-F-Y-Suc-Y-F-OH) included succinic anhydride which, through hydrolysis, was used to lower the pH and form a hydrogel network under aqueous conditions.³¹ Field-Emission Scanning Electron Microscopy (FE-SEM) revealed the formation of peptide nanofibers that were intertwined and helical in nature (Figure 1.5a-b).

Addition of Pd^{2+} yielded the formation of Pd nanoparticles that were monodispersed on the peptide bolaamphiphile hydrogel, ranging in diameter between 4 and 7 nm (Figure 1.5c-d).³¹ These materials were then used as catalysts for Suzuki coupling. In a 1:1 solvent of H_2O :methanol along with K_2CO_3 , 0.0024 mmol of catalyst was mixed with 0.08 mmol of various aryl halides and 0.12 mmol of various aryl boronic acids.³¹ It was found that the aryl halides with iodine required 2 h at 40 °C to reach 100% conversion while the aryl halides with bromine required 4 h at 50 °C.³¹ As seen, controlling the self-assembly of the

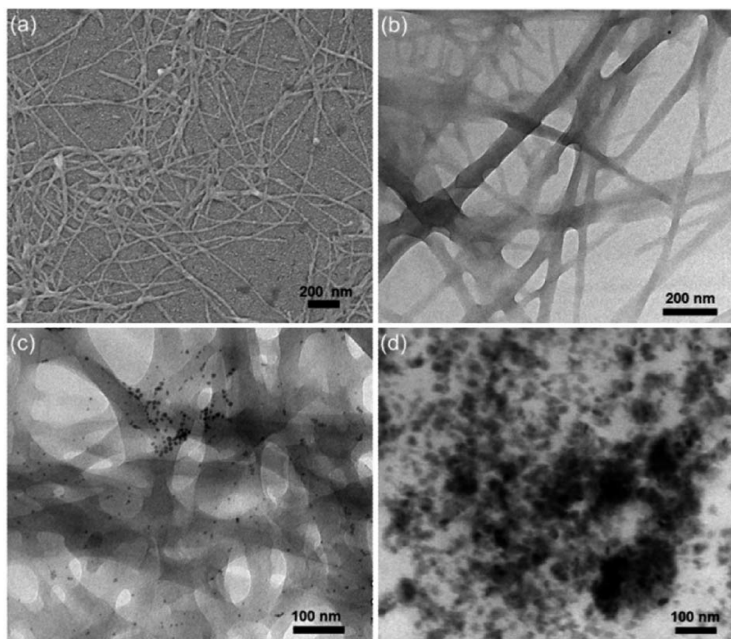


Figure 1.5. Electron microscopy images of the peptide bolaamphiphile hydrogel network. (a) FE-SEM showing the nanofibrillar network (b) TEM of hydrogel (c) TEM of hydrogel with Pd nanoparticles (d) TEM of aggregated Pd yielded without presence of hydrogel. Reproduced from Ref 31 with permission of The Royal Society of Chemistry.

peptide hydrogel through the use of succinic anhydride represents a unique manner of shape-direction of such Pd nanomaterials, which were then found to be very effective catalysts for C-C coupling reactions.

While the R5 peptide and other bio-inspired molecules were able to form non-spherical materials, its structure-direction capabilities are dependent upon the formation of a template.²³ To increase particle shape diversity, the ability for individual peptides to recognize and bind crystallographic facets could be useful to generate unique particle morphologies, such as cubes and tetrahedra. In this event, the facet-specific peptides could bind such surfaces to arrest particle growth in that direction, thus only allowing metal deposition at selected facets. This selectivity can be challenging to achieve using traditional ligands; however, by employing biocombinatorial selection techniques using well

characterized single crystal surfaces, the identification of such peptides is possible. Recent studies by Huang and coworkers have employed these approaches for Pt-based materials.²⁴⁻

26

One of the first shape directing peptides isolated was the BP7A sequence (TLHVSSY), identified by phage display using a Pt wire target by Li and Huang. This sequence preferentially binds the {110} facet of Pt, resulting in the formation of multipod structures.²⁵ By reducing K_2PtCl_4 with $NaBH_4$ in the presence of the BP7A, multipods were formed based upon particle growth in the {111} and {100} directions. In general, pod extensions were preferred along the {111} direction over the {110} due to the energetics of the respective facets. Interestingly, the concentration of the peptide in the materials synthesis also led to particle shape control. In this event, multipods were favored at low peptide concentrations; however, as the BP7A concentration in the reaction increased, the formation of spherical particles resulted.²⁵ This suggests that while the BP7A preferentially binds to the {110} facet, it also possesses sufficient binding capabilities for the {111} and {100} surfaces to arrest growth along those directions at high peptide concentrations. Electrochemical analysis of the multipods demonstrated increased surface area as the pod extension length increased. In fact, for the largest pod structures studied, these materials possessed an ~2 fold increase in electrochemical Pt surface area as compared to commercially available Pt black,²⁵ suggesting that these materials possess unique structures for catalytic applications. While the BP7A sequence was found to have preferential binding for Pt {110} surfaces, this specificity was unanticipated. In order to identify peptides with clear affinity for selected facets, single crystal surfaces must be used during the biocombinatorial selection process. To this end, Huang and coworkers used Pt

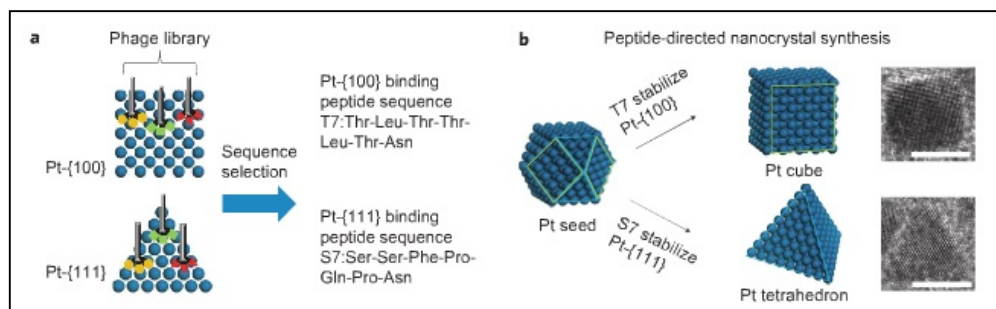


Figure 1.6. Approach used for the isolation of Pt facet-specific peptides. Part (a) illustrates the use of single crystal Pt surfaces for the isolation of the T7 and S7 peptides, while part (b) demonstrates the growth of nanocubes and nanotetrahedra using cubooctahedral seeds and the facet-selective peptides (scale bar 5 nm). (Reprinted by permission from Macmillam Publishers Ltd: Nature Chemistry, Chiu, C.; Li, Y.; Ruan, L.; Ye, X.; Murray, C. B.; Huang, Y. Platinum Nanocrystals Selectively Shaped Using Facet-specific Peptide Sequences. *Nat. Chem.* **2011**, *3*, 393-399, copyright 2011.)

nanocubes that display only $\{100\}$ facets and Pt nanooctahedra that present only $\{111\}$ facets to isolate sequences that preferentially bind the displayed surface (Figure 1.6).²⁴ Using these materials, phage display identified the T7 (TLTTLTN) and S7 (SSFPQPN) sequences that bound the Pt $\{100\}$ and $\{111\}$ facets, respectively. This specificity is achieved via the bioselection process and is likely the result of the peptide sequence and amino acid composition that recognize the crystallographic arrangement at the different surfaces. Such specificity would be difficult to achieve using other traditional ligands where the complexity of the peptides are well suited for this level of structural differentiation.

Once the facet selective peptides were obtained, their use in Pt nanoparticle formation has been shown to control nanoparticle morphology.²⁴ This is achieved using a modified seed mediated approach. In this system, the peptides, H_2PtCl_6 , a Pt^{4+} source, and ascorbic acid are co-mixed in solution. To this, NaBH_4 is added to reduce a fraction of the Pt^{4+} ions, which induces particle nucleation to form single crystal seeds.²⁴ The formation of single

crystal seeds is important to control the final particle morphology. Once the NaBH_4 is fully consumed, the residual Pt^{4+} ions are reduced at the seed surface by the ascorbic acid in solution. Note that under these conditions, ascorbic acid is too weak to initiate Pt^0 nucleation, thus requiring NaBH_4 . Due to the facet selectivity of the peptides, the biomolecules will bind at their preselected surface to ensure particle growth along the non-bound facets. As such, when using the S7 peptide as the capping agent, Pt nanoparticles with tetrahedral morphologies were the predominant shape. After a 1.0 h reaction time, 70% of the materials observed by TEM were tetrahedral with an edge length of 6.0 ± 0.9 nm.²⁴ Substitution of the S7 with the $\{100\}$ binding T7 sequence resulted in the production of Pt nanocubes. In this system, 70% of the final structures were cubic with edge lengths of 7.6 ± 1.0 nm after a 30 min reaction time.²⁴ Interestingly, for both materials, a transition from pseudospherical like seed particles to the shaped final structure was observed. This strongly indicates that facet selective binding occurs to promote growth along the unbound surfaces of the initial seeds.

Expansion of peptide-based nanoparticle shape control can be achieved by modifying the initial seed structure. In this work, Ruan *et al.* employed the S7 and T7 peptides; however, single-twinned Pt nanoparticles were used as the seeds to initiate nanoparticle shape selection.²⁶ Such seed morphologies were generated using the BP7A peptide responsible for Pt multipod formation,²⁵ upon which the facet selective S7 and T7 sequences can be added to further control particle growth and shape formation. As observed via HR-TEM analysis, the S7 and T7 systems were found to generate $\{111\}$ -bipyramids and right bipyramids, respectively, all based upon the changes to the seed structure. The $\{111\}$ -bipyramids formed by the S7 were enclosed by six $\{111\}$ facets and possessed lattice

spacings consistent with the $\{111\}$ planes of Pt.²⁶ Furthermore, the angles formed by the metallic planes at the vertices of the structures were measured to be $\sim 64^\circ$, which is quite close to the theoretical value of 63° . The right bipyramids formed by the T7 sequence consisted of two right tetrahedra extending from the $\{111\}$ center twin plane with six $\{100\}$ exposed facets.²⁶ The angles formed by shape of the structure at the vertices are measured to be 90° and 142° , similar to theoretical values of 90° and 143.1° . Such structure selection is again inherent in the peptide facet selectivity; however, by tuning the seed morphology, changes to the global nanoparticle structure are possible. By tuning the composition and structure at individual steps during the synthetic strategy, new functional materials could be developed.

In a separate study, Cha and colleagues have also isolated peptides that preferentially bind the Pt $\{100\}$ surface.²⁷ Preformed Pt nanocubes that expose $\{100\}$ surfaces to solution were again used as the target for phage display. From this study, a consensus sequence of PW_{xx}QRELSV was elucidated for peptide binding $\{100\}$ facet, where xx represents random residues.²⁷ For the synthetic studies, the sequence YQPWKTQRELSV was used to determine peptide-based nanoparticle shape direction. In this study, the authors employed different Pt precursors for materials synthesis, where the Pt²⁺ source and the rate of reduction significantly affected the shape of the final nanomaterials. For instance, when K₂PtCl₄ was reduced by NaBH₄ in the presence of the peptide, 1-2 nm Pt nuclei were observed; however, substitution of K₂PtCl₄ with Pt(NH₃)₄(NO₃)₂ in the same reaction generated 3-4 nm polyhedral Pt nanoparticles.²⁷ This change in particle morphology was attributed to changes in the reduction rate of the two precursors. To further ascertain such reduction rate affects, H₂ gas was employed as the reductant. In this

approach when using K_2PtCl_4 , 7-8 nm cubic Pt nanoparticles were observed when capped with the Pt {100} binding sequence.²⁷ Interestingly, when $\text{Pt}(\text{NH}_3)_4(\text{NO}_3)_2$ was used in the H_2 system, no reduction was observed over 16 h. Taken together, this suggests that while the peptide can be responsible for controlling the material morphology, additional factors including the metal source and reduction rate can dramatically affect the structure and composition of the final material. Such abilities could potentially be tuned in combination to allow for additional synthetic control that remains challenging to achieve.

1.3 Au and Ag Noble Metals

Au and Ag nanoparticles are well known for their unique optical properties that arise from the local surface plasmons that are related to the size, shape, and dispersity of the materials.³² Such properties can be exploited for a variety of applications including optics, biosensing, and catalysis. Due to the ease of synthesis, Au has been extensively studied for biomimetic and peptide-based syntheses, where the initial findings have been well reviewed previously.² As such, the present focus will be directed towards more recent results in characterization of the surface binding events to Au and Ag materials. Slocik *et al.* have demonstrated that unique chiroptical properties can be integrated into Au nanoparticles via peptide surface functionalization as determined via CD spectroscopy.³³ This is achieved through the binding of the chiral peptides at the particle surface, which is typically controlled through non-covalent interactions for materials binding sequences. In this study, spherical Au nanoparticles with a diameter of 10 nm were complexed with either the E5 (CGGEVSALEKEVSALEKEVSALEKEVSALEK-EVSALEK) or FlgA3 (DYKDDDDKPAYSSGAPPMPPF) peptides. The E5 is a helical peptide with a cysteine

residue incorporated at the N-terminus. While the helical portion is not anticipated to interact with the Au surface, the exposed thiol of the cysteine will covalently bind the nanoparticle.³³ This peptide was chosen due to the strong CD-observed properties associated with the helical structure to monitor such effects at the Au surface. In this study, the preformed Au nanoparticles possessed a plasmon band at ~530 nm, and were found to be achiral due to the lack of absorbance in the CD spectrum. CD analysis of the free E5 peptide demonstrated absorbances at ~208 and 222 nm with negative ellipticity, corresponding to the α -helical structure. When bound to the Au nanoparticles, these CD responses decreased in intensity, which is likely due to partial peptide unfolding; however, a new absorbance in the visible range with negative ellipticity was observed from the E5-capped materials.³³ This surprising new peak likely arises from the plasmon band of the nanoparticles coupled to the dipole interactions with the chiral peptide. Similar observations are noted when the same Au nanoparticles are capped with the FlgA3 peptide that non-covalently binds to the surface. Using this differently bound biomolecule, a CD response at ~520 nm was again observed due to the interactions between the chiral peptide and the plasmon band of the materials (Figure 1.7).³³ Interestingly, aggregation of the particles caused a red shift in the plasmon-induced CD absorbance, which is likely due to interparticle plasmonic coupling. These unique optical observations arise from the interactions of peptides with the Au materials, where such property manipulations could be exploited for various applications including plasmonic devices and biosensing.

Recent studies by Rosi and colleagues have exploited the interactions between Au nanoparticles and the A3 sequence (AYSSGAPPMPF) to drive highly intricate self-assembly processes. These approaches are capable of forming helical assemblies³⁴⁻³⁵ and

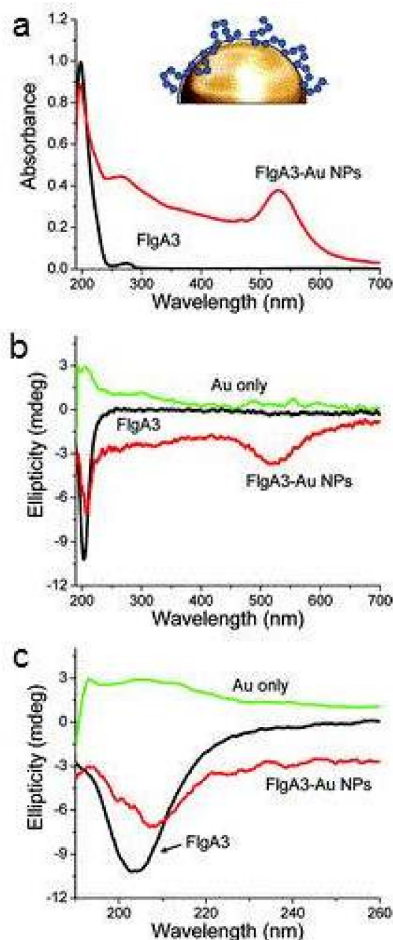


Figure 1.7. Chiroptical characterization of the FlgA3 binding to Au nanoparticles. Part (a) presents the UV-vis analysis of nanoparticles, while part (b) displays the CD spectra of the individual components (peptides and Au nanoparticles), as well as the peptide-capped particles. Note the new absorbance formed at ~520 nm for the peptide-capped particles. Part (c) presents an expanded image of the CD spectra in the UV region. (Reprinted with permission from Slocik, J. M.; Govorov, A. O.; Naik, R. R. Plasmonic Circular Dichroism of Peptide-Functionalized Gold Nanoparticles. *Nano Lett.* **2011**, *11*, 701-705. Copyright 2011 American Chemical Society.)

hollow spheres³⁶ of Au nanoparticles. The process is achieved through specific sequence modifications with hydrophobic components, which drives peptide assembly and nanoparticle formation. To form helical Au nanoparticle assemblies, dodecanoic acid was fused to the N-terminus of the A3 peptide to form the C_{12} -PEP_{Au} species. This results in the formation of a twisted nanoribbon structure via peptide assembly based upon the two

regions of the sequence (hydrophobic/organic and hydrophilic/biological). In this arrangement, the structures are anticipated to extend the Au recognition motif to solution from which nanoparticle binding/formation could be achieved. TEM and Atomic Force Microscopy (AFM) analysis of the biological helices demonstrated dimensions of up to $4\ \mu\text{m}$ in length with a width of $6.1 \pm 0.6\ \text{nm}$. Furthermore, these nanoribbons were structured as a left-handed twist with a pitch of $84.1 \pm 4.2\ \text{nm}$.³⁴ Spectroscopic analysis via CD and Fourier-Transform Infrared (FTIR) Spectroscopy indicated that the assembly process was driven by the formation of β -sheets within the ribbon structure. The first four amino acids in the PEP_{Au} sequence, AYSS, were considered responsible for the formation of β sheets as well as playing a role in driving the left-handed twist.³⁴ Meanwhile, the bulky nature of the prolines in the peptide sterically hinders the formation of a condensed structure and promote the assembly of nanoribbons.

Using the twisted nanoribbons, the formation of Au nanoparticle double helices was demonstrated.³⁴ Solutions of HAuCl₄ and C₁₂-PEP_{Au} in HEPES buffer were first filtered to remove any assembled structures and then allowed to sit for 30 min. As shown in Figure 1.8a-d, TEM analysis revealed the formation of double-helical assemblies with discrete spherical Au nanoparticles.³⁴ The distance between the gold nanoparticles on opposite sides of the helices was measured to be $6.0 \pm 0.8\ \text{nm}$, which corresponds quite well with the width of the double helix ($6.1 \pm 0.6\ \text{nm}$). Furthermore, the pitch of the nanoparticle assemblies was $83.2 \pm 4.4\ \text{nm}$, similar to the twisted nanoribbon itself, indicating that nanoparticle binding does not significantly perturb the peptide assembled structure.³⁴

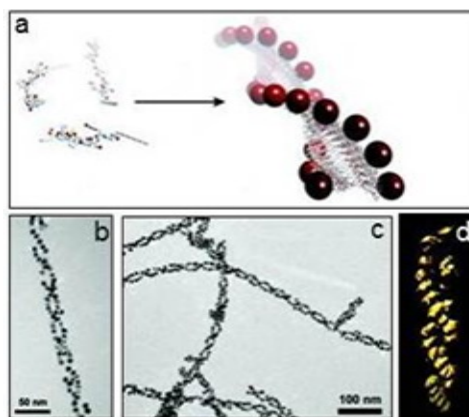


Figure 1.8. Peptide-based formation of nanoparticle superstructures Part (a) depicts the formation scheme of a peptide double helix using the C_{12} -PEP_{Au} sequence, while parts (b and c) present TEM images of Au nanoparticle double helices using the peptide (scale bar 50 and 100 nm, respectively). Part (d) presents the representative 3D image of the assembled structure achieved via tomography. (Reprinted with permission from Chen, C.-L.; Zhang, P.; Rosi, N. L. A New Peptide-Based Method for Design and Synthesis of Nanoparticle Superstructures: Construction of Highly Ordered Gold Nanoparticle Double Helices. *J. Am. Chem. Soc.* **2008**, *130*, 13555-13557. Copyright 2008 American Chemical Society.)

Changing the composition of the buffer and the reaction time was further found to affect the size and density of the nanoparticle structures formed using the C_{12} -PEP_{Au} assembly. By diluting the HEPES buffer with triethylammonium acetate (TEAA) buffer and by increasing the incubation time, an increase in the density of nanoparticles in the interhelical regions of the helices was observed.³⁵ Such changes in particle density and structural definition are potentially useful for electronic applications, while individual particle size control would be important for additional applications. As such, further efforts to control the particle morphology and assembly were explored. For instance, sodium citrate was added to the reaction system to investigate its affect as a capping agent on the assembled Au nanostructures.³⁵ Indeed, the addition of selected concentrations of citrate to the synthesis reaction resulted in smaller, nearly monodisperse Au nanoparticles of 6.2 ± 0.8 nm versus the 8.1 ± 1.0 nm particles formed in the absence of the ligands. The Au

nanoparticles were also further spaced within the helical structure, which is likely due to the electrostatic repulsions of the negatively charged citrate molecules on the particle surface.

After demonstrating the formation of left-handed double helices, Song *et al.* further expanded on that work to generate right-handed double helices using a similar C₁₂-PEP_{Au} conjugate molecule.³⁷ In the previous work, L-amino acids were employed and theorized that the chirality of the L-amino acids was what led to the left-handed twist of the helices.^{34,37} Thus, L-amino acids were substituted for D-amino acids in the PEP_{Au} portion of the conjugate molecule and the formation of a right-handed twist was observed. From TEM images, it was measured that the right-handed double helical Au structures had nanoparticles with a diameter of 5.25 ± 0.74 nm where the pitch was ~ 82 nm, the interhelical distance ~ 7.5 nm and the interparticle distance ~ 1.7 nm.³⁷ Using larger Au nanoparticles (through longer Au³⁺ incubation times), CD spectroscopy was then used to study the optical properties of both the left-handed and right-handed helices in solution. Both Au nanoparticle superstructures yielded two CD signals, one corresponding to the peptide and another corresponding to the plasmon of the Au nanoparticles, that were equal but opposite in charge. This resulted in a negative signal for the left-handed and a positive signal for the right-handed helices at ~ 220 nm for the peptide and 562 nm for the Au plasmon.³⁷ Additionally, it was found that changing the Au nanoparticle diameter shifted the CD signal for the plasmon to longer wavelengths, exemplifying that these unique Au nanoparticle superstructures can be tuned for certain physical properties (*i.e.* direction of turn in helices), as well as certain optical properties.³⁷

Through this work, Rosi and group have developed a methodology for generating “peptide-conjugates,” in that linking together a materials-binding peptide along with an organic functionality will create a template for a multitude of assembled material specific superstructures.³⁸ Following this model, the group linked together C₁₂ with Au binding peptide where the effect of the number of phenylalanines present at the C-terminus of the peptide was explored by modifying the quantity of phenylalanine added from 0 – 3. First, the assembly of the peptide conjugate in a HEPES buffer solution was studied over time and then analyzed through TEM imaging via staining the samples with phosphotungstic acid.³⁸ It was seen that the number of fibers formed in solution increased over time and with the quantity of phenylalanines present, in that the peptide with three phenylalanines had the thickest formation of intertwined fibers.³⁸ Using AFM, these intertwined fibers were measured to be ~20 nm tall.³⁸ Expanding on the TEM studies, Au³⁺ was added along with TEAA, and incubated for one day. TEM analysis was repeated in which it was seen that conjugate 1 (0 phenylalanine) resulted in linear but irregular oriented nanoparticles with a width of 24.1 ± 4.1 nm and a nanoparticle diameter of 8.1 ± 1.3 nm, while conjugate 2 (1 phenylalanine) resulted in double helices, as previously reported.^{34, 38} Furthermore, conjugate 3 (2 phenylalanines) yielded thick branched one-dimensional nanoparticle structures with a width of 61.4 ± 15.7 nm and a nanoparticle diameter of 6.3 ± 1.2 nm, while conjugate 4 (3 phenylalanines) yielded thin intertwined one-dimensional nanoparticle structures with a width of 20.5 ± 4.9 nm and a nanoparticle diameter of 6.0 ± 1.1 nm.³⁸ The variety of structures formed represent proof of concept that peptides conjugated to organic molecules are a viable avenue for creating a multitude of nanoparticle superstructures for various applications.

While external reagents can modify the structure of the inorganic materials, additional modifications to the hydrophobic region of the PEP_{Au} sequence can alter the morphology of the final Au nanoparticle assemblies.³⁶ In this study, the dodecanoic acid species required for peptide helix formation is substituted with n-hexane. Furthermore, the n-hexane is spaced from the Au-binding domain of the peptide by two additional alanine residues, thus generating the C₆-AA-PEP_{Au} sequence.³⁶ Using this species under identical reaction conditions as employed with the original C₁₂-PEP_{Au}, the formation of hollow Au spherical superstructures is observed (Figure 1.9).³⁶ In this event, Au nanoparticles form a shell like structure where the interior portion of the assembly remains hollow.

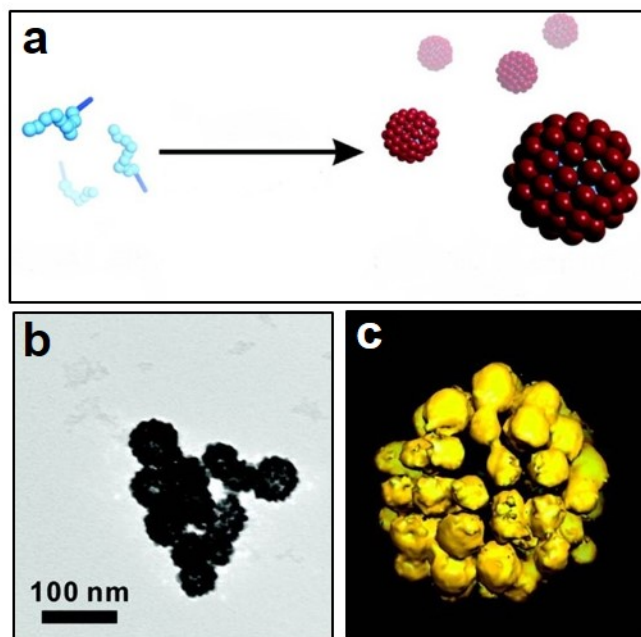


Figure 1.9. Part (a) displays the peptide-based assembly of Au nanoparticles to form hollow spherical superstructures using the C₆-AA-PEP_{Au} peptide. Part (b) presents the TEM analysis of the hollow nanospheres (scale bar 100 nm), while part (c) presents a 3D surface rendering of the tomographic volume. (Reprinted with permission from Song, C.; Zhao, G.; Zhang, P.; Rosi, N. L. Expedient Synthesis and Assembly of Sub-100 nm Hollow Spherical Gold Nanoparticle Superstructures. *J. Am. Chem. Soc.* **2010**, *132*, 14033-14035. Copyright 2010 American Chemical Society.)

Using this approach, the organized superstructures possessed a diameter ~ 137 nm as visualized by TEM and AFM. Tomographic analysis confirmed the hollow morphology of the materials, which is likely directed by the formation of spherical peptide assemblies in solution prior to the completion of Au nanoparticle formation. These unique structural formations, helices and hollow spheres, are likely due to the templating capabilities of peptide/materials binding for the formation of large assemblies. Such periodic structures could likely be quite important for future advances in plasmonics, catalysis, and biosensing where other approaches cannot readily achieve the degree of complexity observed using the modified peptides.

Expansion of the use of C₆-AA-PEP_{Au} for the formation of hollow spherical Au nanostructures was conducted by Zhang, *et al.* where the facile synthesis was optimized and shown to be customizable for three different diameters.³⁹ First, the concentration of the HEPES buffer was examined where it was determined that the peptide conjugate, C₆-AA-PEP_{Au}, organized in solution more rapidly at lower concentrations of buffer.³⁹ Through manipulation of such HEPES concentrations, as well as the concentration of HAuCl₄-TEAA, and time, the three sizes of hollow Au nanostructures were discovered. The small spheres, by TEM imaging, were shown to have an average diameter of 40.4 ± 5.9 nm, while the medium spheres and large spheres had average diameters of 75.3 ± 12.4 nm and 149.7 ± 30.8 nm, respectively.³⁹ Extinction coefficients were determined for each size of Au nanostructure through UV-vis spectroscopy. The small spheres had a maximum at 545 nm, while the medium spheres had a maximum at 670 nm and the large spheres at 740 nm.³⁹ Interestingly, the large spheres' extinction maximum is in the near-infrared

(NIR), suggesting these large Au nanostructures could have applications in the biological field.

In regards to Au-binding peptides, such as A3 which was used extensively by Rosi and group to generate superstructures such as helices and hollow nanostructures, Li, *et al.* have conducted extensive work on a library of peptides, which included A3, to yield Au nanoparticles of varied surfaces and catalytic properties.⁴⁰ The library used included seven peptides originally isolated to bind to Au, two peptides originally isolated to bind to Ag and one peptide isolated to bind to Pd.⁴⁰ First, the plasmon formation of the Au nanoparticles prepared with each peptide was observed with UV-vis spectroscopy. Each material yielded a surface plasmon resonance at ~520 nm except for the Z1 peptide which had a broad shoulder around the plasmon at 520 nm and the Pd4 peptide which had a broadened absorbance versus the other materials.⁴⁰ Following the determination that stable materials were capable of being formed using each peptide, TEM analysis showed spherical nanoparticles with average diameters ranging from 2.3 ± 0.5 nm to 5.1 ± 1.6 nm.⁴⁰ In order to study the catalytic behavior, 4-nitrophenol reduction studies were conducted using each peptide-capped Au nanoparticle system as the catalyst. From the rate constant determined for reduction, across different temperatures, activation energies were computed. Furthermore, these activation energies were correlated to previously determined binding affinities of each peptide. All in all, these correlations reveal a classification of the peptides and the manner for which they bind to the Au surface.⁴⁰ This system revealed that some peptides are enthalpic binders in that they have high activation energies (>20 kJ/mol) and multiple anchor residues throughout the sequence, leading to a flatter orientation on the metal surface.⁴⁰ On the other hand, some peptides were found to be

entropic binders where the activation energies were lower (9.1 – 15.1 kJ/mol) and the anchor residues were less abundant, leading to a limited area of contact with the metal surface.⁴⁰

Beyond helical and spherical nanoparticles, other shapes have been known to be formed using peptides in Au nanoparticle synthesis. The formation of NPNs using the R5 peptide were previously demonstrated using Pd at high ratios of metal:peptide.²²⁻²³ The Knecht group continued this work to include Au, again forming NPNs, through the use of the R5 self-assembling template to stabilize the Au materials.⁴¹ Ratios of metal:peptide were varied from 30-120:1 where the ratios >60 were determined to be unstable. Therefore the ratios of 30:1 and 60:1 were used in the study, termed Au30 and Au60, respectively.⁴¹ By UV-vis analysis, a large broad absorbance was seen for both Au30 and Au60 at >580 nm. From X-ray Diffraction studies (XRD), reflections associated with the (111) facet of Au were noted, resulting from the zerovalent Au present in the materials.⁴¹ Furthermore, using Scherrer's analysis, these reflections were used to predict crystallite sizes of 6.2 nm for Au30 and 6.4 nm for Au60, which was confirmed using TEM (Figure 1.10), indeed, the Au30 had an average width of 6.7 ± 1.1 nm and Au60 had an average width of 7.1 ± 1.3 nm.⁴¹ Interestingly, TEM imaging also showed the formation of NPNs at both ratios, whereas with the previous metal Pd, increasing metal concentration with R5 resulted in a morphology change of spheres to nanoribbons to NPNs.²²⁻²³ Thus it was postulated that something unique was occurring between the Au³⁺ and the R5 peptide template not seen with Pd. From DLS studies, it was seen that the Au³⁺ formed large aggregates through interaction with the peptide framework, leading to the reduced NPN morphology regardless

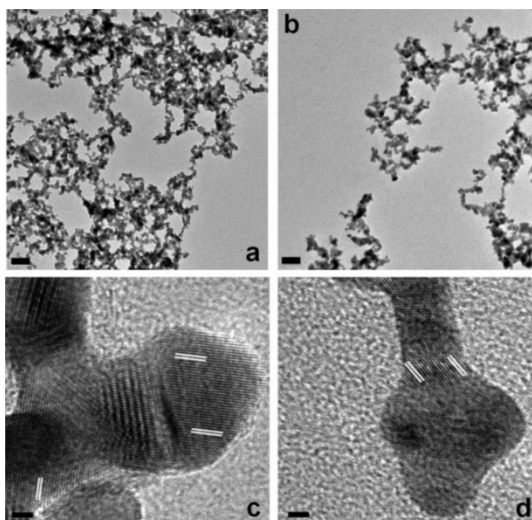


Figure 1.10. TEM analysis of Au₃₀ and Au₆₀ NPNs. Figure (a) is low magnification of Au₃₀ while figure (b) is Au₆₀. Figure (c) is the high resolution image showing the lattice spacing of Au₃₀ whereas figure (d) is Au₆₀. Reproduced from Ref 41 with permission of The Royal Society of Chemistry.

of the metal concentration.⁴¹ 4-nitrophenol reduction studies were employed to probe the materials further where that both Au₃₀ and Au₆₀ resulted in similar activation energies of 29.0 ± 1.4 kJ/mol and 27.7 ± 1.6 kJ/mol, respectively.⁴¹ This demonstrated that the peptide framework remains flexible even at higher metal loadings and thus does not limit substrate diffusion and catalytic activity.

Further work on templating peptides for the formation of Au nanomaterials was conducted by Stevens and colleagues where they synthesized a peptide that resulted in the formation of ultrasmall Au nanoclusters.⁴² The sequence used was a triple repeat of glycine, arginine and proline with a cysteine at the N-terminus to yield CGRPGRPGRP, where cysteine was added as a nucleation site for Au, while proline imbued a helical structure and arginine assisted in the final materials use in cell uptake.⁴² Optimal characterization of the C(GRP)₃ nanoclusters revealed a lack of surface plasmon formation and subsequently a fluorescence emission at ~630 nm (from an excitation wavelength of

440 nm), which suggested that the nanoclusters were less than 2 nm in diameter.⁴² Small-Angle X-ray Scattering (SAXS) studies confirmed an average radius of 3.7 Å, which was similar to the predicted size of the peptide cage, indicating that the C(GRP)₃ was forming a cage in solution that could control the Au nanocluster growth.⁴² With the small size being optimal for uptake into cells and being fluorescent in the NIR, confocal microscopy studies then revealed that the nanocluster could be incorporated into cells and diffused in the cytosol.⁴² These studies demonstrate the utility of fabricated peptides for Au nanomaterials synthesis for biological applications with far-reaching possibilities of further functionalization.

In a similar fashion to the work of Rosi and colleagues, Kim *et al.* have demonstrated the production of spherical superstructures that consist of a hybrid of the Ag and Au binding AG4 peptide (NPSSLFRYLPSD) and Au nanoparticles.⁴³ Mixing 0.2 mg of the peptide with 0.1 mM HAuCl₄ in water at 37 °C resulted in the formation of large, spherical Au/peptide structures with an overall diameter of 473.8 ± 121.5 nm.⁴³ Control analysis of the Au salt and peptide alone in solution demonstrated no assembly, indicating that both components are required for superstructure formation. It was suggested that the Au³⁺ ions were likely reduced to form Au⁰ nanoparticles via the tyrosine residue of the peptide sequence, as observed previously.⁴⁴ Interestingly, Au nanoparticles permeated throughout the assembled materials where a bimodal distribution of inorganic components was observed. To that end, smaller Au nanoparticles with a diameter between 2.5 nm and 4.5 nm were present inside the spheres intermixed with peptide molecules, while larger Au nanoparticles with an average diameter of 8.6 ± 2.2 nm were observed on the surface.⁴³ The authors suggest that the two different sizes of Au nanoparticles arise from the different

environments, where the surface-exposed materials grow to larger sizes due to more exposure to Au^{3+} ions in solution. The size of the assembled structures was shown to be dependent upon the reaction temperature, where increasing the temperature to 50 °C and 70 °C resulted in a size decrease to 208.2 ± 53.1 nm and 114.4 ± 19.6 nm, respectively. Surprisingly, the diameter of the surface-displayed Au nanoparticle barely changed with the reaction temperature, decreasing in size to 8.3 ± 2.1 nm at 50 °C and 8.1 ± 1.9 nm at 70 °C. This suggests that the system temperature preferentially affected the assembly of the hybrid spheres, but only minimally affected the growth of the surface Au nanoparticle.⁴³

Further studies were performed by altering the AG4 peptide sequence to elucidate key residues responsible for both superstructure generation and Au nanoparticle formation.⁴³ Phenylalanine and tyrosine residues were replaced with glycine and/or serine to remove the aromatic species. In this regard, four peptide analogues were created: Y to S (NPSSLFRSLPSD), Y to G (NPSSLFRGLPSD), F to G (NPSSLGRYLPSD) and F and Y to G and S (NPSSLGRSLPSD). While Au^{3+} reduction was observed during material synthesis using all four modified peptides, none of the sequences resulted in the formation of hybrid spheres. For all four systems, a wire-like assembly was observed, composed of randomly shaped Au nanoparticle aggregates.⁴³ This was interesting since Au nanoparticles were still formed, suggesting that tyrosine was not specifically required for reduction of Au^{3+} ions. Taken together, this work suggests that larger structures beyond peptide-capped nanoparticles can be generated using materials-directing sequences, where no peptide modifications are required to generate the assembly. Such morphologies could be important for delivery capabilities where minimization of the structure components is desirable.

Beyond Au materials, Ag nanostructures have recently been generated by Belcher and colleagues using the E6 (EEEEEE) and D6 (DDDDDD) peptides.⁴⁵ These sixmer homopeptides were selected as carboxylic acid containing residues are known to interact with metal ions and metal surfaces.⁴⁶ The peptides were expressed on the surface of yeast and added to a Ag^+ solution for 24 h with no external reductant. Over this time frame, the reaction solution changed color from orange to red, with a growth of an absorbance peak at ~ 400 nm in the UV-vis spectrum.⁴⁵ TEM imaging of the yeast-based Ag materials demonstrated the formation of stable metallic nanoparticles coating the cell surface.⁴⁵ It was found that the yeast peptide complex facilitates the reduction process, but light was needed to fully reduce the Ag ions. These reduction capabilities were shown to be increased when the peptides were bound to the cell surface as free E6 peptide in solution demonstrated minimal to no reduction capabilities. Interestingly, as confirmed through computational analysis, the E6 sequence was capable of mediating greater degrees of Ag^+ reduction over the D6 peptide for nanoparticle formation.⁴⁵ This is likely due the pocket-like structure of the E6 where a large concentration of carboxylic acid can facilitate increased metal binding as compared to the linear D6 sequence.

With confirmation of glutamic acid's ability to form Ag nanomaterials, changes in the inorganic morphology were studied when M13 bacteriophage were employed as the biotemplate.⁴⁷ In this strategy, four glutamic acid residues were expressed on the virus major coat protein. From this arrangement, the formation of Ag nanowires was observed where the metallic materials were ~ 30 nm thick.⁴⁷ Selected Area Electron Diffraction (SAED) analysis demonstrated that that five $\{111\}$ twin boundaries were present in materials, suggesting a strong templating capability of the initial viruses. Once the Ag

nanowires were formed, FePO₄ could be deposited onto the surface. Interestingly, an anhydrous FePO₄ layer was generated, as confirmed by Thermogravimetric Analysis (TGA), which was surprising as the materials were deposited from an aqueous solution. Electrochemical performance testing of the FePO₄ deposited nanowires demonstrated discharge capacities at a low C/10 discharge rate of 165 mAh/g and at a higher 1C discharge rate of 110 mAh/g.⁴⁷ These rates are similar to FePO₄ materials synthesized at high temperatures, where the low temperature virus-based synthesis is an attractive alternative. Taken together, these very high capacities and discharge rates make these viral-based inorganic materials potential components for Li-ion batteries.

Carter *et al.* have also advanced peptide-based methods for Ag nanoparticle formation employing the Ge8 sequence (SLKMPHWPHLLP) that was originally isolated to fabricate germania.⁴⁸⁻⁴⁹ Using this peptide, Ag⁰ nanoparticles were generated with a diameter of 4.1 ± 0.9 nm that were again generated in the absence of traditional reductants. To fabricate these materials, the peptide, HEPES buffer, and light are required for the reduction reaction.⁴⁹ Recent studies have indicated that HEPES buffer is capable of reducing metal ions for nanoparticle formation,⁵⁰ which likely leads to Ag⁰ materials, in combination with photoreduction. Furthermore, the residues of the Ge8 sequence could also assist in Ag nanoparticle formation via multiple events. For instance, tryptophan is a known reductant capable of reducing Ag⁺ to Ag⁰,¹¹ lysine can act as a surface capping agent, acid/base catalysis can occur at the histidine residue,⁴⁹ as well as a variety of other coordination capabilities could occur via the additional amino acids of the sequence. These capabilities were explored through residue substitutions with alanine in the parent Ge8 sequence.⁴⁹ For instance, the replacement of either of the two histidines of the Ge8 resulted in the formation

of larger Ag nanoparticles with a diameter of 5.3 ± 1.4 nm. With a methionine or tryptophan replacement, no nanoparticle formation was visible using the standard synthetic approaches, through either spectroscopic or TEM characterization. Further changes in the particle size were achieved via scrambling of the peptide sequence that resulted in still larger particles of 7 ± 3 nm. This suggests that the amino acid composition and overall sequence order play an intimate role in controlling the particle morphology, which could be tuned to achieve the desired particle size and composition.

In a unique analysis, immobilization of the Ge8 on a solid surface resulted in further surprising structural changes of the final Ag materials. Upon introduction of Ag^+ ions and HEPES buffer to the biofunctionalized surface, the formation of crystalline curled nanomaterials was observed, as shown in Figure 1.11. The materials possess a large spherical structure from which a nanowire extends in a curled fashion.⁴⁹ At present, it remains unclear as to why the wire-like structures are produced at the peptide interface;

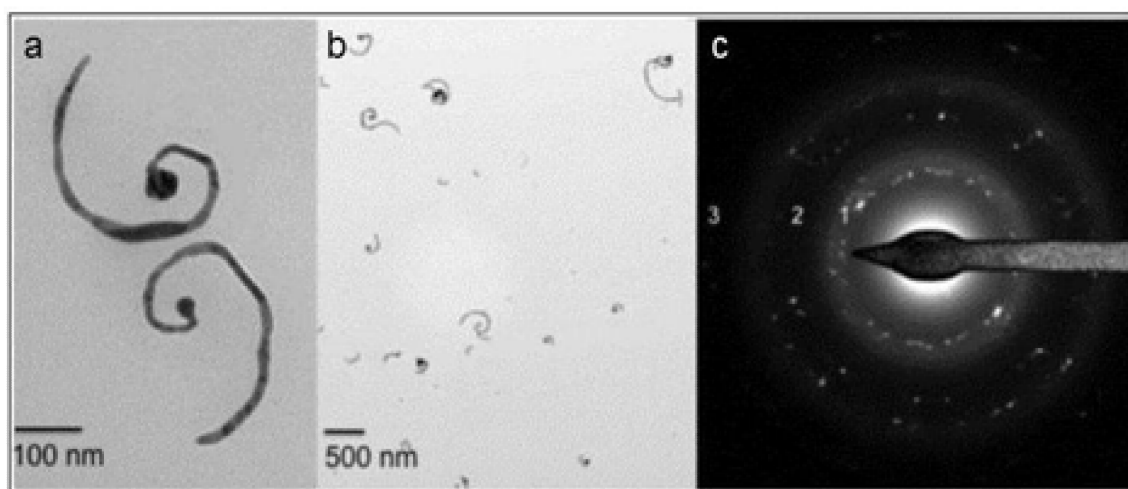


Figure 1.11. Parts (a and b) present the TEM analysis of the curled Ag nanomaterials formed by the Ge8 peptide. Part (c) presents the diffraction pattern of the nanowires. (Reprinted with permission from Carter, C. J.; Ackerson, C. J.; Feldheim, D. L. Unusual Reactivity of a Silver Mineralizing Peptide. *ACS Nano* **2010**, *4*, 3883-3888. Copyright 2010 American Chemical Society.)

however, it is possible that the immobilization strategy affects the ability of the sequence to bind to the growing Ag^0 structure to arrest continued particle growth.

In contrast to the *in vitro* protocols previously discussed, Hall Sedlak, *et al.* have recently identified a Ag-binding peptide sequence capable of forming Ag nanoparticles *in vivo*.⁵¹ Through phage display, the AgBP2 (EQLGVRKELRGV) peptide sequence was identified to have a high affinity for Ag. This peptide was then attached to the end of a *E. coli* maltose binding protein (MBP), where the protein was expressed in both the periplasm (MBP-AgBP2p) and cytoplasm (MBP-AgBP2c) of the cells, and then exposed to an increasing concentration of AgNO_3 .⁵¹ Dosing experiments revealed that the cells expressing MBP-AgBP2p had a higher tolerance to Ag^+ compared to those expressing MBP alone as well as MBP-AgBP2c. Further time-course experiments involving MBP-AgBP2p and MBP-

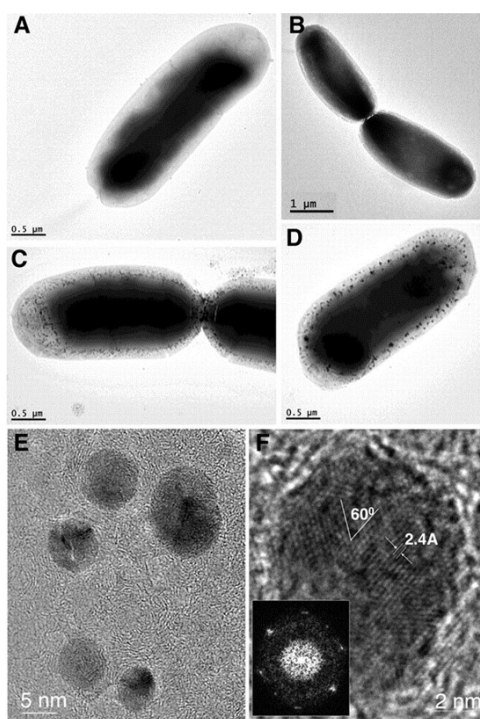


Figure 1.12. TEM images of cells with MBPp (parts A and B) and MBP-AgBP2p (parts C and D) 1 h after AgNO_3 addition. Parts E-F show high resolution from the periplasmic space and the visible $\langle 111 \rangle$ lattice fringes. Copyright © American Society for Microbiology, Appl. Environ. Microbiol. 78, 2012, p.2289-2296, doi:10.1128/AEM.06823-11

AgBP2c as well as MBP-AG4 (a different Ag-binding peptide) showed that cells with MBP-AgBP2p had an increased viability in a solution of 28 μM AgNO_3 compared to all other variants studied.⁵¹ TEM imaging, as seen in Figure 1.12, was conducted of the cells containing MBP-AgBP2p where small nanoparticles can be seen in the periplasmic space (Figure 1.12C-D). The nanoparticles were confirmed as Ag based upon the measured lattice fringes (Figure 1.12E-F).⁵¹ This work further confirms that Ag ions become toxic once entering the cytoplasm of cells as seen by the lack of viable cells containing MBP-AgBP2c. Overall, this work exemplifies that materials-binding peptides can be employed *in vivo*, opening up applications for biological sensing and imaging.

1.4 Metal Oxides

Metal oxide materials are highly important structures with multiple crystal phases. They possess unique properties associated with the individual structures, which can be used for applications in catalysis, photovoltaics, and optics. Peptide-based precipitation is well known to occur in nature through the fabrication of biosilica in sponges⁵² and diatoms,¹ where such approaches can be translated to the formation of other oxides on the benchtop. Recent research has focused on the fabrication of semiconductor and ferroelectric materials including ZnO ,⁵³⁻⁵⁴ TiO_2 ,⁵⁵⁻⁵⁶ and BaTiO_3 ,⁵⁷ where their technological applications are quite important.

ZnO is a well characterized semiconductor due to its wide band gap, making it attractive for applications in solar cells, piezoelectric transducers, chemical sensors, and photocatalysis. These properties are optimized based upon the material's crystal structure, thus recent studies have focused on directing and controlling such structural properties.⁵³

Tomeczak *et al.* have demonstrated the fabrication of ZnO materials employing the Z1 (GLHVMHKVAPPRGGGC) peptide.⁵³ The Z1 sequence is quite similar to a peptide (GAHVMHKVAPRP) previously used by Adschiri *et al.*⁵⁸ to generate ZnO nanoflowers. In the study of the Z1 peptide, Zn(NO₃)₂ was used as the Zn²⁺ precursor where 1,3-hexamethylenetetramine (HMTA) was added in attempts to manipulate the ZnO crystal growth.⁵³ Using this precipitation method, hexagonal platelet formation was observed by SEM. HRTEM imaging and SAED analysis of the ZnO platelets revealed one diffraction pattern present from the crystals, verifying a twinned wurtzite crystal structure. Such a structure was maintained when fabricated with peptide reaction concentrations up to 0.5 mg mL⁻¹. Should the peptide concentration be decreased, the ZnO materials could grow to larger sizes with hexagonal shapes, suggesting that the Z1 peptide preferentially binds to the {002} facets.⁵³

To further the peptide-based ZnO materials for eventual applications, it is important that the structures be selectively deposited at designed interfaces. As such, silk films were soaked in solutions of the Z1 peptide and Zn(NO₃)₂ for ZnO fabrication at the film surface.⁵³ SEM imaging of the materials revealed that ZnO crystals formed hexagonal rods that were oriented perpendicularly to the silk-based substrate. XRD analysis noted the presence of both the silk II crystal structure, arising from the substrate, and the wurtzite structure of ZnO.⁵³ It is likely that both the amino acid identity and peptide sequence are involved in directing the ZnO synthesis. For instance, the glycine and cysteine residues of the GGGC tail of the peptide have been suggested to initiate the interaction with the growing ZnO materials, while the positively charged lysine and arginine residues potentially repel the negatively charged ZnO surface to promote interactions with the

adjacent amino acids. Furthermore, the use of histidine and cysteine in combination with glycine, proline, lysine, and arginine is likely to assist in the formation of a single layer hexagonal platelet over basic layered zinc salt structures.⁵³

In separate ZnO studies, Perry and colleagues demonstrated particle size control using the G-12 (GLHVMHKVAPPR) and GT-16 (GLHVMHKVAPPRGGGC) peptides.⁵⁴ Zn(NO₃)₂, HMTA, G-12 and GT-16 reaction solutions were prepared by varying the reagent concentrations and adjusted to a neutral pH. The solutions were incubated for 24 h at 20 °C, followed by heating at 65 °C for 72 h. Samples from the reaction mixtures were acquired for SEM, IR, and TGA analysis at select times. A decrease of the crystal length (L) to diameter (D) ratio (L/D) was observed to be selected for by the peptides. For instance, the L/D was determined to be 2.7 for the control samples fabricated in the absence of peptide; however, the L/D decreased to 1.0 and 1.7 for the materials produced in the presence of the G-12 and GT-16 peptides, respectively. FTIR analysis of the bio-based ZnO materials verified the presence of peptides binding to the inorganic structures via observation of the amide I band at 1600-1700 cm⁻¹ and amide II band at 1500-1600 cm⁻¹. In comparing the free peptides to the ZnO complexed sequences, the FTIR spectra demonstrated blue shifts in the amide bands for the bound species, which likely arises from peptide absorption to the crystal surface. TGA analysis also verified the presence of the peptide due to the additional mass loss associated with the biomolecules.

Further characterization of the growth of the ZnO materials over time was conducted to elucidate the effects of peptide binding over the structure of the materials.⁵⁴ For the control studies in the absence of peptide, the rod-like ZnO crystals grew at a rate of 149 nm h⁻¹ in length and 3.4 nm h⁻¹ in diameter. When the G-12 peptide was added to the reaction, the

growth rate in the longitudinal direction decreased to 10 nm h^{-1} , with no change in the rate of growth of the material diameter noted. With the GT-16 sequence, the materials grew at a rate of 7 nm h^{-1} in the length; however, an increased rate of growth in the diameter was noted.⁵⁴ These significant changes in directional growth rates are likely due to binding of the peptides to specific ZnO facets, where absorption studies were performed using G-12 and GT-16 on single crystal ZnO films of (0001) and (10-10) to confirm such a theory. For both sequences, the surface peptide density was found to be greater on (0001) plane over the (10-10) surface. It was also determined that the overall surface density for the GT-16 ($0.31 \text{ nmol cm}^{-2}$) was greater than the G-12 ($0.08 \text{ nmol cm}^{-2}$).⁵⁴ Such results were confirmed via X-ray Photoelectron Spectroscopy (XPS) analysis of the peptides on the different surfaces. Together, this work demonstrated a unique peptide-based method to control metal oxide structures via facet selective binding.

Additional semiconductor oxides have also recently been prepared using peptide-based synthetic approaches, including TiO_2 .⁵⁵ Such materials possess exciting optical and electrical properties for application in photovoltaics and photocatalysis, and for use as catalyst supports. Unfortunately, most established TiO_2 synthesis methods require high temperatures or caustic conditions.⁵⁹ To overcome this limitation, peptide-directed syntheses have been developed that occur at room temperature in water.⁵⁵ To achieve this, Sandhage and colleagues have identified peptides via phage display that direct the formation of TiO_2 nanoparticles, mimicking the ambient conditions typically observed in Nature. By using this biocombinatorial method, 20 peptides were identified that specifically bound to the {100}, {110}, or {001} facets of TiO_2 by using single crystal targets. From this approach, 16 different peptides were isolated having an affinity for either

of the {110} and {100} surfaces (eight each), while only two peptides demonstrated binding to the {001} surface. Interestingly, one peptide, Ti-3 (KSLSRHDHIIHHGW), was noted that bound to both the {110} and {001} planes, while a further single sequence, Ti-4 (TQHLSHPRYATKGGGW), had high degrees of affinity for all three surfaces. From this newly derived library, four sequences were studied further for their ability to precipitate TiO₂: Ti-1 (RKKRTKNPTHKLGGGW {110}), Ti-2 (MRMIRRFPSLKGGGW {100}), Ti-3, and Ti-4. Solutions of the four peptides were added to titanium (IV)-bis-ammonium-lactato-dihydroxide (TiBALDH) solutions maintained at pH 6.3 with a sodium phosphate/citrate buffer. Upon addition of the peptide to the Ti precursor after 10 min at room temperature, a white precipitate was noted that was collected by centrifugation.⁵⁵ After the materials were washed numerous times, the final product was quantitated using a colorimetric assay at 335 nm. From this peptide-based approach, the amount of TiO₂ produced per mole of peptide ranged from 8.1 ± 1.1 for the Ti-4 peptide to 38.7 ± 1.6 for the Ti-1 sequence, which resulted in percent yields of $16.4 \pm 2.3\%$ and $75.4 \pm 3.3\%$, respectively.⁵⁵ On average, the Ti-1 precipitated the greatest amount of TiO₂, which is likely due to the peptide possessing the greatest number of basic residues (lysine, arginine, and histidine), resulting in a larger overall positive charge. This charge effect is highly important as the growing TiO₂ materials possess a negative surface that will more readily interact with positively charged sequences. Based upon these observations, two new peptides were designed to enhance TiO₂ production: dTi-1 (H/R) and dTi-1 (RKK). The dTi-1 (H/R) peptide was synthesized using the parent Ti-1 that swapped the histidine residue of the sequence to an arginine. This was anticipated to expand the pH dependence of TiO₂ formation to pH values between 4 and 8 due to the

increased charge characteristics of the lysine residue. The second new sequence, dTi-1 (RKK), was also synthesized based on the Ti-1; however, it possessed a tetrameric repeat of the first three amino acid residues of the Ti-1 sequence to increase the number of positively charged residues present in the peptide. Analysis of TiO₂ production from these designed sequences demonstrated enhanced synthetic abilities. For instance, the dTi-1 (RKK) precipitated the most TiO₂ of all peptides studied with product yields of $83.9 \pm 4.4\%$.⁵⁵ Note that it also possessed the greatest positive charge as well. For the dTi-1 (H/R) sequence, diminished product yields of $67.3 \pm 6.1\%$ were noted, as compared to the yields observed with both the parent Ti1 and dTi-1 (RKK). This suggests that while the positive charge of the peptide is an important factor in TiO₂ production, an unresolved role for the histidine exists that increases materials production. Such residues can act as acid/base catalysts,⁴⁹ which may be important for polycondensation reactions that are used to generate metal oxide materials.

SEM characterization of the materials generated using the Ti-1, Ti-2, Ti-3, and dTi-1 (RKK) sequences demonstrated particles with diameters between 50 nm and 100 nm that were fused into networks.⁵⁵ For those materials fabricated by the Ti-4 and dTi-1 (H/R) peptides, similar morphologies were observed, but with larger particle diameters. Energy Dispersive Spectroscopy (EDS) analysis of the precipitates confirmed the presence of titanium, oxygen, and phosphorus, where the phosphorus likely arises from the buffer. HR-TEM images of the individual structures demonstrated that the particles were a mixture of fine nanocrystals (<10 nm) agglomerated together with various amorphous materials.⁵⁵ Electron and X-ray diffraction analyses of the materials demonstrated a mixture of anatase and monoclinic β -TiO₂ crystal phases, which was surprising as such materials typically

require high temperatures for synthesis.⁵⁹ From these findings, it was demonstrated that peptides could mediate the formation of TiO₂ under ambient conditions, which is quite desirable; however, the specificity of such peptides for selected metal oxides remains unclear. For instance, peptides could bind multiple substrates, thus identification of sequences with single surface specificity is desirable.

To increase the material specificity of the peptides, Fang *et al.* employed subtractive phage display to isolate TiO₂ binding peptides with minimal to no ability to bind compositionally similar SiO₂.⁵⁶ In this method, phage that bound to SiO₂ were first removed from the library, from which the new virus subset was used to identify peptides that bound to TiO₂. To that end, no SiO₂-binding phage in the subset that was used to isolate TiO₂ binding sequences would be present, thus all sequences isolated during the biopanning process should only bind the desired target. Through this technique, seven peptides were identified, which were termed Ti(~~Si~~) to denote their TiO₂ specificity and inability to bind SiO₂.⁵⁶ Analysis of the individual sequences for materials production demonstrated the desired specificity. For instance, the Ti(~~Si~~)-1 peptide (YPSAPPQWLTNT) produced the greatest amount of TiO₂ (~0.01 mg TiO₂ (mg peptide)⁻¹). In this sequence that was the most identified peptide in the library, a third of the residues were serine, tyrosine, or tryptophan, with no positively charged amino acids. Interestingly, the Ti(~~Si~~)-4 sequence (ATTLHPPRTSLP) precipitated the least amount of material of all of the peptides studied (~0.003 mg TiO₂ (mg peptide)⁻¹).⁵⁶ The composition of this peptide was similar to the Ti(~~Si~~)-1 sequence; however, two basic amino acids were present (histidine and arginine). This was quite surprising as the peptides discussed above for TiO₂ binding⁵⁵ demonstrated enhanced materials production from sequences with greater

numbers of basic residues. Furthermore, the highly positively charged sequences produced more oxide precipitate than the peptides isolated via subtractive phage display. Unfortunately, different titanium precursor solutions were used in the two studies; the $\text{Ti}(\text{Si})$ peptides were unable to precipitate TiO_2 using TiBALDH, thus potassium bis(oxalato)oxotitanate(IV) $[\text{K}_2(\text{TiO}(\text{C}_2\text{O}_4)_2) \cdot 2\text{H}_2\text{O}]$ was substituted to observe reactivity. Metal oxide precipitation using $[\text{K}_2(\text{TiO}(\text{C}_2\text{O}_4)_2) \cdot 2\text{H}_2\text{O}]$ and the $\text{Ti}(\text{Si})-1$ sequence was found to be pH dependent, differing in activity based on whether the reaction solution was above or below the pI of the peptide (5.5). For instance, precipitation studies at pH values of 3-4 resulted in more product, likely due to the overall positive charge of the peptide, while at pH values ≥ 6 , both the peptide and TiO_2 were negatively charged, preventing the electrostatic interactions that enhance materials precipitation.

Characterization of the structure of the TiO_2 nanoparticles prepared with the $\text{Ti}(\text{Si})$ peptides was performed using SEM, EDS, and TEM. From these analyses, it was revealed that the precipitate was formed from the agglomeration of fine particles of <100 nm in diameter. The materials were mainly composed of titanium, oxygen, and trace other elements from the precursor solution. With full characterization of the TiO_2 fabrication abilities, the sequences were studied for SiO_2 production. Using standard SiO_2 -based methods,¹ no precipitation was observed, strongly suggesting that compositional specificity can be integrated into the selected sequences employing subtractive phage display.

Using biomimetic approaches, Ahmad *et al.* have identified additional peptides capable of producing ferroelectric BaTiO_3 particles under ambient conditions.⁵⁷ Again using phage display, the BT1 (HQPANDPSWYTG) and BT2 (NTISGLRYAPHM) peptides were

identified to mediate the formation of multicomponent metal oxide. Mixing of the peptides with barium acetate and potassium bis(oxalato)oxotitanate(IV) at a pH of 6.8 for 2 h at room temperature resulted in precipitation of the BaTiO₃ materials. SEM and TEM characterization of the precipitate from both peptides demonstrated that small faceted particles of 50-100 nm were observed to agglomerate to form structures with overall dimensions of 300 – 500 nm (Figure 1.13).⁵⁷ XRD analysis indicated that crystalline materials were generated with tetragonal BaTiO₃ crystallinity. Control studies on the peptide sequence were subsequently performed that varied the hydroxyl and charged residues of the peptide, which resulted in the production of amorphous materials. This suggests that the sequence and composition of the materials-directing peptide is critically

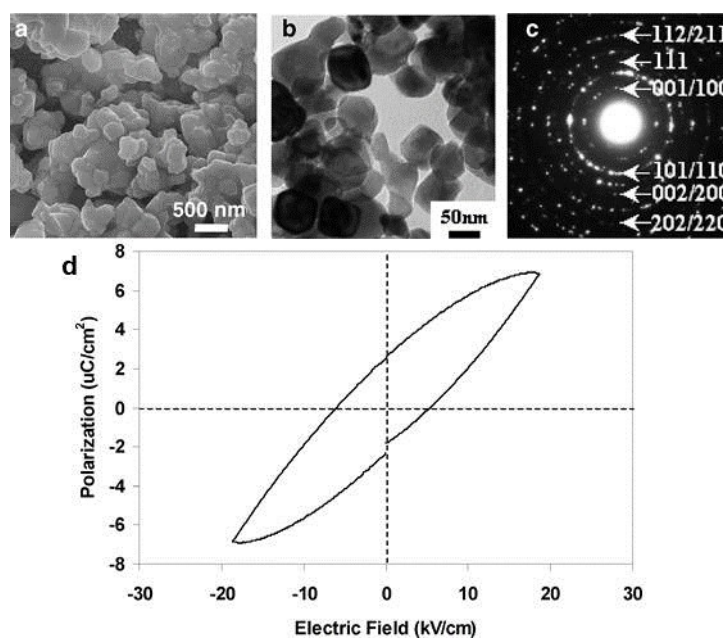


Figure 1.13. Analysis of BaTiO₃ fabricated using peptides. SEM and TEM images of the materials fabricated using the BT2 peptide are presented in parts (a and b), respectively, while part (c) displays the SAED pattern of the precipitated BaTiO₃ particles. Part (d) depicts a plot of the polarization versus applied electric field for the ferroelectric materials. (Reprinted with permission from Ahmad, G.; Dickerson, M. B.; Cai, Y.; Jones, S. E.; Ernst, E. M.; Vernon, J. P.; Haluska, M. S.; Fang, Y.; Wang, J.; Subramanyam, G., *et al.* Rapid Bioenabled Formation of Ferroelectric BaTiO₃ at Room Temperature from an Aqueous Salt Solution at Near Neutral pH. *J. Am. Chem. Soc.* **2008**, *130*, 4-5. Copyright 2008 American Chemical Society.)

important for metal oxide fabrication. Ferroelectric performance testing of the BaTiO₃ precipitated using the BT2 sequence demonstrated polarization hysteresis, which could prove to be useful for memory storage devices (Figure 1.13d).

1.5 Catalytic Applications

It is well established that nanoparticles are advantageous for application in catalysis.^{12, 16-17, 29, 60 13, 15, 18-19, 22, 28, 41} The use of nanoparticles can lead to increased catalytic activity based upon higher surface-to-volume ratios, shape,²⁵ exposure of particular facets,²⁴ and tunable material composition.⁶¹ Furthermore, the use of nanoparticles in catalytic applications can also lead to a reduced amount of metal required for equivalent activity, resulting in reaction conditions under more sustainable environments.⁶⁰

1.5.1 Stille Coupling

One specific reaction that has been previously shown to be optimized through the use of nanocatalysts is Stille coupling.¹² Typically employing Pd as the catalyst,⁶² this C-C coupling reaction begins with oxidative addition of the Pd⁰ to an aryl halide to form Pd²⁺, upon which transmetalation occurs through the use of an organotin compound.⁶³ After transmetalation, reductive elimination results and the product is formed along with regeneration of the Pd⁰ catalyst (Figure 1.14).⁶³ There is much debate over the mechanism upon which Stille coupling operates, either via a homogeneous or heterogeneous system.⁶³

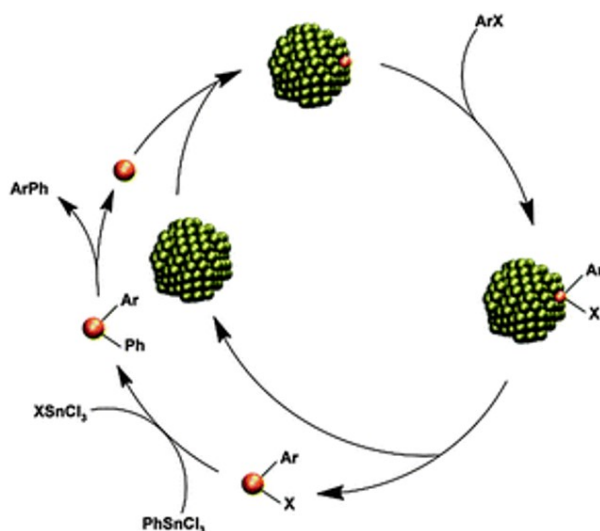


Figure 1.14. Suggested mechanism of Stille coupling with nanoparticles. (Reproduced and adapted from Ref. 64 with permission from the PCCP Owner Societies.)

A large concentration of nanocatalysis studies focus on this debate, whether the Pd atoms are abstracted by a leaching mechanism and then undergo catalysis in a homogeneous manner,^{16, 64} or whether the aryl halide adsorbs to the nanoparticle surface and catalysis occurs there.⁶⁵ Further studies are required to continue to elucidate the Stille coupling mechanism with nanoparticles fully.

1.5.2 Suzuki Coupling

Another C-C coupling reaction often employing Pd nanocatalysts is Suzuki coupling.⁶⁶ This reaction is similar to Stille coupling in that it occurs under similar processes, except that the transmetalation agent is known to be less toxic.⁶⁷ Suzuki coupling is initiated by oxidative addition of Pd⁰ into the carbon-halide bond of an aryl halide substrate.⁶⁸ Transmetalation occurs with this reaction as well, except with Suzuki coupling, an organoboronic acid is employed.⁶⁸ Following transmetalation, reduction elimination with product generation and catalyst reformation occurs.⁶⁸ There is also debate on whether

Suzuki coupling operates via a homogeneous leaching mechanism or surface mechanism.⁶⁹ Another issue debated with this C-C reaction is the state of the organic boronic acid needed for transmetalation, where it could either exist in a neutral state or be converted to an anionic species by the included base to promote transformation.⁷⁰⁻⁷² Detailed studies over the mechanism of such reactions are necessary for optimization using nanocatalysts, in order to achieve the end result of higher activities under greatly needed ambient conditions.

1.5.3 Heck Coupling

Heck coupling is an additional type of C-C coupling known to use Pd catalysts. Coupling, in the instance of this reaction, occurs using an aryl or vinyl halide and an alkene in the presence of a base.⁷³ As with Stille and Suzuki coupling, the first step of the reaction involves oxidative addition of the Pd into the carbon-halide bond. The subsequent steps are syn addition and β -elimination to yield the product and regenerate the Pd catalyst (Figure

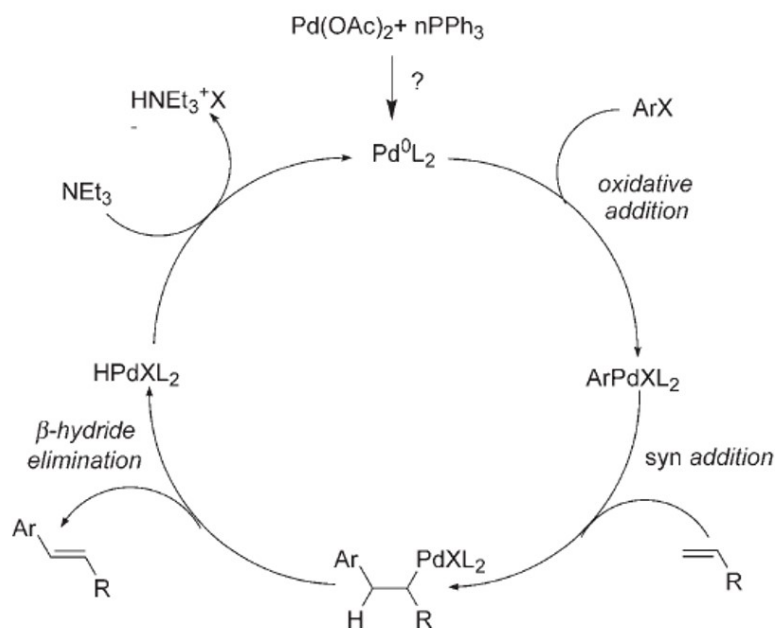


Figure 1.15. Typical mechanism for Heck coupling. (Reproduced from Ref. 30 with permission © 2006 WILEY-VCH Verlag GmbH, Weinheim, Fed. Rep. of Germany).

1.15).⁷³ There is also a significant debate over whether the reaction occurs via a homogeneous or heterogeneous mechanism, in which the research involving nanocatalysts, while on-going, suggests a homogeneous mechanism.^{69, 74-75} Regardless of the mechanism, Heck coupling remains an attractive route for C-C coupling as it employs alkene substrates and has *trans* selectivity.⁷³

1.5.4 4-Nitrophenol Reduction

Moving away from C-C coupling reactions, which are useful for pharmaceutical syntheses as well as generation of energy-related products,⁷⁶ is a reaction useful for pollution remediation, 4-nitrophenol reduction.⁷⁷ In contrast to the previously discussed reactions, 4-nitrophenol reduction is known to occur on the surface of the catalyst⁷⁸ which is advantageous for elucidation of structural details of the nanoparticles employed. This reaction is initiated by the addition of NaBH₄ as a hydrogen source, as hydrogen is needed in excess to drive the reduction.⁷⁷⁻⁷⁹ Once the catalyst is saturated with hydrogen, 4-nitrophenol is added to the system and is reduced to 4-aminophenol.⁷⁸ Another advantage of this reaction, besides the simple setup and surface mechanism, is the direct monitoring capable through the use of UV-vis spectroscopy, where 4-nitrophenol is known to absorb at 400 nm.⁷⁸ From the change in absorbance, reaction rates and activation energies can be determined, thus enabling comparisons between multitudes of nanoparticle systems.^{22, 41,}

1.6 Summary and Conclusions

A great number of materials-directing peptides are now available for a diverse set of technologically important materials compositions (see Chapter 6.1, Table 5). While biocombinatorial methods are capable of isolating further sequences, it would be highly desirable to develop computational approaches for the *de novo* design of peptides to generate materials of controlled size, composition, shape, and ultimately function. Such abilities would be quite important for programmable materials fabrication that could immediately be used in many applications ranging from optics and biosensing to catalysis and energy storage. To achieve these predicted capabilities, it is critical that a greater understanding of the surface binding events be known, where recent studies discussed herein have significantly advanced this level of knowledge. While these initial steps have demonstrated key results, further significant efforts are truly required. Unfortunately, the complete characterization of the biotic/abiotic interface has been hampered by the lack of physical characterization methods; therefore, to advance peptide-based approaches, new techniques are needed. These include new spectroscopy, microscopy (including high-resolution and staining methods), and other methods that allow for the characterization of molecular level events for materials of 1 – 100 nm in size. Such approaches are becoming available, thus leading to a better understanding of the biomolecular surface.

“Reprinted and adapted with permission from (Briggs, B. D.; Knecht, M. R. Nanotechnology Meets Biology: Peptide-based Methods for the Fabrication of Functional Materials. *J. Phys. Chem. Lett.* **2012**, *3*, 405-418). Copyright (2012) American Chemical Society.”

Chapter 2. Atomic-Scale Identification of Pd Leaching in Nanoparticle Catalyzed C-C Coupling: Effects of Particle Surface Disorder

2.1 Overview of Study

C-C coupling reactions are of great importance in the synthesis of numerous organic compounds, where Pd nanoparticle catalyzed systems represent new materials to efficiently drive these reactions. Despite their pervasive utility, the catalytic mechanism of these particle-based reactions remains highly contested. Herein we present evidence of an atom leaching mechanism for Stille coupling under aqueous conditions using peptide-capped Pd nanoparticles. EXAFS analysis revealed Pd coordination changes in the nanoparticle consistent with Pd atom abstraction, where sizing analysis by SAXS confirmed particle size changes associated with a leaching process. It is likely that recently discovered highly disordered surface Pd atoms are the favored catalytic active sites and are leached during oxidative addition, resulting in smaller particles. Probing the mechanism of nanoparticle-driven C-C coupling reactions through structural analyses provides fundamental information concerning these active sites and their reactivity at the atomic-scale, which can be used to improve catalytic performance to meet important sustainability goals.

2.2 Motivation

Carbon-carbon (C-C) coupling reactions are pervasively used for chemical synthesis; however, they typically require unsustainable conditions of high temperatures, organic solvents, and high Pd loadings.^{60, 62} Conversely, Pd nanoparticles could advance these reactions toward more sustainable conditions, where such materials have recently been

employed to drive Stille, Suzuki, and Heck couplings under favorable conditions such as ambient temperatures, aqueous solvents, and ultra-low catalyst concentrations.^{12, 60, 80-82} Unfortunately, the mechanism by which Pd nanoparticles drive these processes remains unclear and greatly contested. By understanding catalytic mechanisms at the atomic level, rationally designed catalysts with increased reactivity under sustainable conditions could be developed.

It is generally accepted that C-C couplings follow a three-step process: oxidative addition, transmetalation, and reductive elimination.⁸³ For oxidative addition, nanoparticle-driven systems have been proposed to operate by two different possible approaches: a surface or metal atom leaching mechanism.^{60, 81, 84} In the surface mechanism, the actual coupling process occurs directly at the metallic interface; however, for the leaching process, oxidative addition results in the abstraction of active Pd species from the nanoparticle to catalyze C-C bond formation in solution. To advance these materials for enhanced activity, it is imperative that the exact mechanism be determined.

There are several compelling arguments to support either a surface-based⁸⁵⁻⁹³ or atom-leaching mechanism.^{16, 74, 94-96} Work by Ellis *et al.* involving an in-depth spectroscopic study of Suzuki coupling suggested that the mechanism operated on the Pd nanoparticle surface.⁸⁵ Using X-ray methods, normalization of the reaction turnover frequency (TOF) indicated that the reaction occurred directly on the nanoparticle surface at edge and vertex atoms.⁸⁵ Continuation of these studies with further *in operando* X-ray experiments, as well as spiking and Hg poisoning studies, lended additional support to a surface-based process for Suzuki coupling.⁸⁸ Furthermore, work done by Lambert and coworkers has indicated that Sonogashira cross coupling can occur solely on the surface of Ag⁸⁹ and Au;⁹⁰⁻⁹¹

however, these studies use single crystalline metallic surfaces and not nanoparticles that may possess disordered surface metal atoms that could affect the reactivity. In addition, studies exploring a surface mechanism for Suzuki coupling were performed by Wang *et al.* where Pd nanoparticles were deposited on Au nanorods. In this approach, the plasmonic properties of the Au component enhanced the reactivity of the Pd materials.⁹²⁻⁹³ Through normalization by the number of surface atoms of Pd, it was postulated that the coupling process was occurring directly on the Pd surface.⁹²

Conversely, extensive studies have indicated that the C-C coupling process does not occur on the Pd nanoparticle surface, but by Pd atoms abstracted from the nanoparticle in solution.^{16, 74, 94-96} For instance, work by Li and coworkers that employed poorly crystalline Pd nanoparticles demonstrated that the materials increased their structural order after the reaction, suggesting that defect (*i.e.* disordered) surface Pd atoms were leached during the coupling process.⁹⁴ Other work also supports a leaching mechanism for C-C coupling, such as Stille TOF studies based upon Pd nanoparticle loading¹⁶ as well as studies from Reetz and Westermann⁹⁶ and de Vries⁷⁴ that detail the *in situ* formation of nanoparticles that are the responsible species for catalysis. Such Pd nanoparticle formation was shown where periodic Transmission Electron Microscopy (TEM) samples taken during Heck coupling using a Pd precatalyst revealed the formation of 1.6 nm nanoparticles.⁹⁶ Interestingly, product formation was not noted until nanoparticles were observed, suggesting that these materials were the active species.⁹⁶ Further work on ligand-free Pd catalysts in the Heck reaction supported the generation of nanoparticles in C-C coupling systems that employs Pd leaching during oxidative addition.⁷⁴ Finally, theoretical studies also have shown that atom abstraction can be the rate-determining step, even if Pd atoms are removed only a

short distance from the surface (3 Å or more).^{64, 97} Taken from all of these contrasting studies, it is evident that further work is necessary to elucidate the mechanism of nanoparticle-driven C-C coupling. In addition, most of these studies employ non-sustainable conditions of energy-inefficient high temperatures and environmentally unfriendly solvents, where an understanding of the effects of the reaction mechanism under energy neutral (room temperature) and aqueous conditions is required to advance their reactivity.

Previous studies in our group have shown that peptide-capped Pd nanoparticles are active catalysts for Stille coupling,^{12-13, 15-19} yet the mechanism remains unresolved. In this chapter, we have employed Extended X-ray Absorption Fine Structure Spectroscopy (EXAFS), in combination with Small Angle X-ray Scattering (SAXS), to examine the Stille coupling reaction catalyzed by peptide-capped Pd nanoparticles under room temperature and aqueous conditions. Based upon changes in the Pd-Pd coordination numbers (CNs) and overall nanoparticle dimensions as a function of the reaction progression, the results strongly support a Pd atom leaching process occurring during oxidative addition under the selected conditions. In the reaction, disordered surface Pd atoms⁹⁷ on the nanoparticle are abstracted, leaving behind a more ordered core. Once leached, the coupling ensues in solution, wherein the liberated Pd species continue to cycle through the reaction. As such, the particle is speciated into two regions: highly reactive disordered surface atoms that are the favored catalytic species and core atoms with lower reactivity. This work presents important new findings on the reactivity of nanoparticles that could play a significant role in the design of new materials for increased reactivity under sustainable conditions.

2.3 Methods

2.3.1 Materials

K_2PdCl_4 and $PhSnCl_3$ were supplied from Sigma Aldrich. $NaBH_4$, *t*-butylphenol, *N*-methyl-*N*-(trimethylsilyl)-trifluoroacetamide (MSTFA), and $CDCl_3$ were purchased from Acros Organics. KOH, ethyl ether, *N,N*-dimethylformamide (DMF), dichloromethane (DCM), acetonitrile, methanol, and $NaSO_4$ were obtained from BDH Chemicals, while NaCl and HCl were from EMD Chemicals. 4-iodobenzoic acid was supplied from TCI America. Water used for all analyses was 18 $M\Omega \cdot cm$ (Millipore, Ultrapure Synergy UV). Finally all peptide synthesizing materials including 9-fluoroenylmethoxycarbonyl (Fmoc) protected amino acids and 4-hydroxymethylphenoxy acetyl (WANG) resins were purchased from Creosalus.

2.3.2 Peptide Synthesis

The Pd4 peptide (TSNAVHPTLRHL) was synthesized using standard solid phase peptide synthesis techniques on a TETRAS peptide synthesizer (Creosalus).⁹⁸ The crude peptide was then purified using reverse-phase HPLC with a water/acetonitrile gradient, and the molecular weight was confirmed with MALDI-TOF mass spectrometry.

2.3.3 Particle Synthesis

Pd4-capped Pd nanoparticles were prepared based on a previously established protocol.¹² Briefly, 25 μL of 0.1 M K_2PdCl_4 was mixed with 100 μL of 10.0 mg/mL Pd4 peptide and

4.775 mL of water in a 20 mL glass vial. The mixture was allowed to complex on the benchtop for 30 min. Next, 100 μ L of freshly made 0.1 M NaBH₄ was added, the vial was swirled to mix, and then the solution was allowed to reduce for 1 h prior to use.

2.3.4 Stille Coupling to Isolate Oxidative Addition

Stille coupling was conducted with an isolated oxidative addition step to probe its effects on the catalytic process. First, 620 mg of 4-IBA was dissolved in 40 mL of 2.25 M KOH. To this solution, 2.5 mL (0.05 mol%) of Pd nanoparticles were added. The solution was allowed to stir for 30 min during which a loss of the characteristic brown Pd nanoparticle color was noted. After 30 min, 493 μ L of PhSnCl₃ was added to the solution. From this point, 4 mL aliquots were taken at regular time intervals and quenched in 25 mL of 5% HCl. The aliquots were then extracted with three times with 30 mL of ethyl ether followed by a wash of two times with 20 mL of saturated NaCl. The organic layer was then dried over Na₂SO₄, after which 75 mg of *t*-butylphenol was added as an internal standard. The organic layer was then removed via rotary evaporation and analyzed via ¹H NMR and GC-MS.¹²

2.3.5 Standard Stille Coupling Reaction

When the materials were studied by EXAFS and SAXS after reaction completion, the catalytic process was studied that did not isolate oxidative addition. In this regard, identical reaction conditions and concentrations were used; however, the 4-IBA and PhSnCl₃ were co-mixed prior to addition of the Pd nanoparticles. Upon reaction initiation via nanoparticle addition, characterization of the material followed using the standard approaches.

2.3.6 Characterization

^1H NMR was conducted on a Bruker Advance Broadband 400 MHz NMR. ~ 1 mg of the solid sample was dissolved in 1 mL of CDCl_3 and then placed in an NMR tube. The integration of the peak at $\delta 6.8$ ppm, corresponding to the internal standard (*t*-butyl phenol), was compared to the integration of the peak at $\delta 8.2$ ppm, corresponding to the product, biphenylcarboxylic acid. GC-MS was conducted with an Agilent 6850 gas chromatograph (GC), equipped with an Agilent 5975C mass spectrometer (MS). The samples were treated with MSTFA by stirring ~ 2 mg of the sample in 200 μL of the silane reagent for 2 h to produce trimethylsilyl ester analogues. The samples were then diluted in DCM to reach a concentration of ~ 1 mg/mL before analyzing.

2.3.7 EXAFS

EXAFS analysis was performed at Brookhaven National Laboratory (BNL) at the National Synchrotron Light Source (NSLS) on beamline X18B. The samples were prepared using 0.3 mol% Pd nanoparticles at 1.125 M KOH with standard Stille coupling conditions (0.5 mmol 4-IBA and 0.6 mmol PhSnCl_3) in a 4 mL total solution volume. The components of the solution were varied, as discussed above, depending on which step of the Stille coupling mechanism was being explored. These solutions were transferred to a kapton-window liquid cell. Energy scans were taken from -150 keV below to 50 keV above the Pd edge jump (24.353 keV). Fluorescence detectors were employed: either a Passivated Implanted Planar Silicon (PIPS) or 13-element Ge detector. Eight scans of each experimental condition were measured, averaged, and processed using the IFEFFIT software.⁹⁹

2.3.8 SAXS

SAXS data were collected at the Advanced Photon Source (APS) at Argonne National Laboratory (ANL) on beamline 12-ID-C at 12 keV. The detector used was an in-house CCD detector. The samples were analyzed at 0.3 mol% Pd nanoparticles in 1.125 M KOH with standard Stille coupling conditions (0.5 mmol 4-IBA and/or 0.6 mmol PhSnCl₃) in 2 mL of total solution. Like the EXAFS studies, the components of the solution were varied depending on which step of the Stille coupling mechanism was being explored. The samples were transferred to 2 mm quartz capillaries for analysis. An exposure time of 0.1 s was used for 60 scans with a 40 s delay between each exposure. Spectra were background subtracted and averaged together using the Igor Pro software.¹⁰⁰

2.3.9 Computational Analysis of Coordination Numbers

Coordination numbers were computed from molecular models of the peptide-covered nanoparticles using molecular dynamics simulations with the CHARMM-INTERFACE force field.¹⁰¹⁻¹⁰³ Atomically resolved structural models of the nanoparticles were obtained using data from High Energy-X-Ray Diffraction (HE-XRD) and Pair Distribution Functions (PDFs) in experiment. The models were employed to examine the conformation and binding energy of peptides adsorbed on the surface in aqueous solution as well as the coordination numbers in equilibrium. The protocol to generate these structures and to carry out molecular dynamics simulations has been previously described in detail.⁹⁷

In brief, the atomistic model for an average Pd nanoparticle derived by reductive synthesis in the presence of peptide Pd4 was obtained as follows. First, an atomistic model

of bulk Pd (large supercell of the fcc unit cell) was processed into a model of a near-spherical nanoparticle with the desired average number of 319 atoms, which was derived from HR-TEM, XRD, and corresponding PDF data. The initial model was built by choosing an arbitrary center atom and a spherical cutoff at 10.5 Å, followed by deletion of surface atoms as needed. Then, PDFs were computed from the initial model and reverse Monte Carlo (RMC) simulations employed to alter the particle structure so that the computed PDF from the model particle fits closely to the experimental PDF. The final particle structure obtained from RMC was further relaxed in molecular dynamics simulation using the CHARMM-INTERFACE force field¹⁰¹⁻¹⁰³ to create a realistic surface structure; this step is necessary as the experimental HE-XRD and PDF data represent a size distribution over several particles while the entire particle size distribution is represented in a single nanoparticle model of average shape. The nanoparticle model was then brought in contact with peptide Pd4 in solution to compute peptide binding conformations and the binding energy near monolayer coverage using several parallel replicas, advanced annealing and sampling protocols.⁹⁷ The same set of data was also previously obtained for various other nanoparticles derived from peptide mutants of the parent Pd4 peptide.

The computation of coordination numbers was carried out by an analysis of the number of nearest atomic neighbors in the equilibrium models, including Pd-Pd and Pd-C/O/N coordination. Thereby, neighbors within the first coordination shell of all Pd atoms were taken into account, *i.e.*, including Pd atoms in the core that only have Pd neighbors, as well as surface Pd atoms that have fewer Pd neighbors as well as some C, N, and O neighbors. The reported coordination number (CN) refers to the average number of Pd, C, N, or O neighbors per atom as an average over all atoms in the Pd nanoparticles, which is equivalent

to the CN measured in XAFS studies. The analysis of the data shows an average Pd-Pd coordination number of 5.8 ± 0.2 for the Pd₄-capped nanoparticles. The average Pd-N/O coordination number is 0.5 ± 0.1 .

2.4 Results and Discussion

2.4.1 Pd Nanoparticle Synthesis

Pd nanoparticles were prepared using the Pd-specific Pd₄ peptide (TSNAVHPTLRHL) based on described methods.¹² UV-vis analysis (see Chapter 6.2, Figure 6.1) indicated the emergence of a ligand-to-metal charge transfer band at 224 nm in a solution of Pd²⁺ and Pd₄, prior to BH₄⁻ addition, consistent with the Pd²⁺ coordinating to the peptide amines.¹² After reduction, the shoulder disappeared and the resulting spectrum was characteristic of nanoparticles formation. TEM analysis, shown in Figure 2.1a, confirmed the formation of quasi-spherical and nearly monodisperse Pd nanoparticles. As indicated by the particle sizing analysis (Figure 2.1b), the peptide-capped nanoparticles have an average diameter of $2.0 \text{ nm} \pm 0.3 \text{ nm}$, consistent with previous studies.¹²

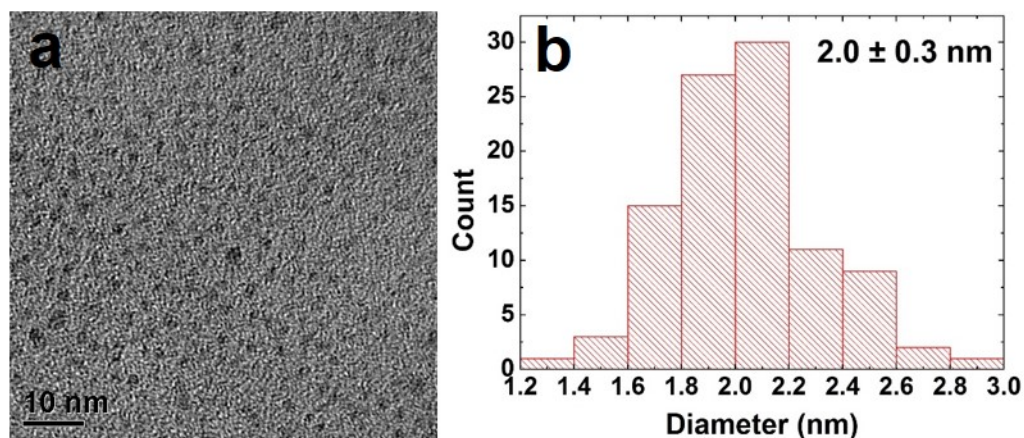


Figure 2.1. TEM characterization of the peptide-capped Pd nanoparticles. Part (a) presents the TEM image, while part (b) displays the particle sizing analysis.

2.4.2 Isolation of Oxidative Addition Step

In an initial study, the nanoparticles were employed to drive a modified Stille coupling reaction (Figure 2.2a), focused specifically on the oxidative addition step for Pd leaching. Typically when the peptide-capped materials are used, the aryl halide, 4-iodobenzoic acid (4-IBA) is commixed with the transmetalation reagent, PhSnCl_3 , followed by nanoparticle addition to drive the reaction.¹³ Under these standard conditions, the entire reaction proceeds to product formation.¹² Furthermore, due to the fast reactivity, it is nearly

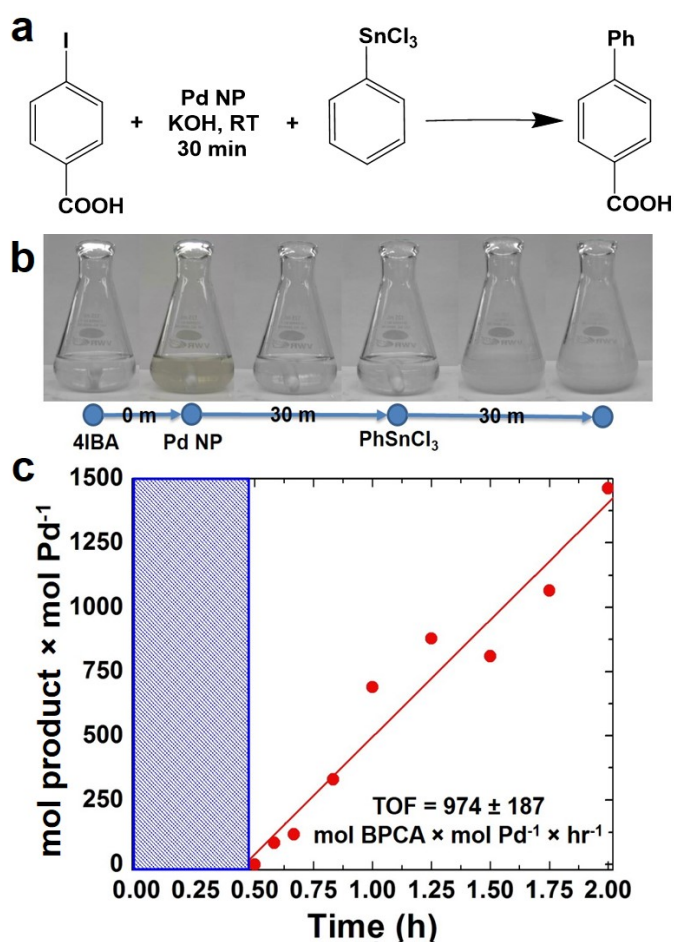


Figure 2.2. Isolation of the oxidative addition step using Pd₄-capped Pd nanoparticles at 0.05 mol% Pd. Part (a) presents the overall reaction, while part (b) displays the color change during oxidative addition. Finally, part (c) shows a TOF reaction analysis plot.

impossible to separate oxidative addition to elucidate the possibility of metal atom leaching. In the modified system, the nanoparticles were added to a solution of 4-IBA at a Pd loading of 0.05 mol%, in the absence of PhSnCl₃. This allows for oxidative addition to occur without continuing on to transmetalation. Initially, the characteristic brown color of Pd nanoparticles was observed at the start of the reaction (Figure 2.2b). The color intensity diminished, which within 30 min, the solution became clear and colorless, suggesting that the nanoparticles were no longer present. Next, PhSnCl₃ was added to initiate transmetalation. Within 15 min, a white precipitate was observed, corresponding to the formation of the product, biphenylcarboxylic acid. Using the addition of the PhSnCl₃ as the reaction starting point, aliquots were taken and the product was quantified to calculate the TOF value (Figure 2.2c). Under these modified conditions, a TOF of 977 ± 187 mol product $(\text{mol Pd} \times \text{h})^{-1}$ was observed. Note that this value is diminished when compared to the standard reaction that does not isolate the oxidative addition step.¹⁵ These diminished TOF results are not surprising; should the Pd nanoparticles be completely leached to Pd²⁺ complexes in solution, a higher concentration of regenerated Pd⁰ species after the reaction would be developed. At these high Pd⁰ concentrations, aggregation to form Pd black would be anticipated. Since Pd black is comparatively unreactive, this would lead to the observed reduction in catalytic activity.

From this analysis, it is evident that a change in nanoparticle morphology occurred during oxidative addition due to the color change. While this analysis is able to isolate oxidative addition, it cannot identify what changes to the nanoparticles actually occurred, which is quite challenging; due to their low solution concentration, observation of a statistically

relevant population of nanoparticles after the reaction via TEM is not possible. As a result, spectroscopic methods are required.

2.4.3 EXAFS Studies

To fully elucidate structural changes to the Pd nanoparticles as a function of the reaction, spectroscopic methods must be employed. Such approaches are required due to the low concentrations that prohibit nanoparticle observation via TEM after the reaction. EXAFS studies of the materials were conducted for various steps of the Stille coupling process, including isolation of oxidative addition. Pd nanoparticle solutions were prepared and transferred to a liquid cell for each analysis, where the materials were examined under three specific conditions: in the alkaline solvent before the reaction (termed Pd NP), in the presence of the aryl halide only (termed Pd NP + 4IBA; *i.e.* the modified reaction of Figure 2.2 to isolate oxidative addition from the whole reaction), and after the Stille coupling process was complete (termed post reaction). For all studies of the materials after the reaction throughout the text, the system was processed wherein the oxidative addition step was not isolated first. In this regard, the 4-IBA and PhSnCl_3 were commixed, to which the Pd nanoparticles were then added to drive the reaction. Since the reaction rate of the system is exceedingly fast, *in situ* analysis of the process via EXAFS was not possible. The aligned, averaged, background-subtracted, and edge-step normalized spectra were fit in *r*-space using FEFF6 theory¹⁰⁴ to determine the local Pd environment.

The *r*-space data (black plots) with corresponding fits (red plots) are shown in Figure 2.3. Initially, the Pd nanoparticles were examined in 1.125 M aqueous KOH, the reaction solvent, in the absence of any Stille coupling reagents (Figure 2.3a). Note that this is not a

catalytic process, but examines the stability of the particles in the reaction medium. In the r-space data, two peaks (not phase-corrected) are clearly evident: one between 2 and 3 Å, corresponding to the Pd-Pd first coordination shell, and a second one between 1.5 and 2.2 Å, due to the Pd-C/O/N contribution. This second peak arises from the peptides bound to the Pd, where EXAFS cannot distinguish between C, O, and N due to their similar scattering profiles. When the Pd nanoparticles were then examined in the same medium, but in the presence of 4-IBA, dramatic changes in the r-space data was evident (Figure 2.3b). For this system, the oxidative addition process is isolated from the overall Stille coupling process to clearly observe the potential effects of Pd leaching using the 4-IBA substrate. In this system, the peak corresponding to the Pd-C/O/N interaction remained; however, the second peak shifted to a lower r-range, demonstrating that no Pd-Pd bonds remained (Figure 2.3b). It is likely that the second peak originates from Pd-I interactions, as discussed below. The lack of a visible Pd-Pd contribution in this EXAFS spectrum suggests that the nanoparticles have been decomposed, consistent with the observed solution color change of Figure 2.2 and a Pd leaching process. The last analysis focused on the Pd nanoparticles after the Stille coupling reaction was complete (Figure 2.3c). For this system, both the 4-IBA and PhSnCl₃ were commixed prior to Pd nanoparticle addition, thus the reaction would immediately go to completion without isolation of the oxidative addition step. Note that the reaction was finished within 5 min, which is too short to analyze

via *in situ* EXAFS at the Pd concentrations used here. This sample again displayed a peak from Pd-C/O/N contributions, and a second peak consistent with Pd-Pd bonds. These tentative attributions of the EXAFS peaks to specific pair interactions in real space were used to guide theoretical modeling, as discussed below.

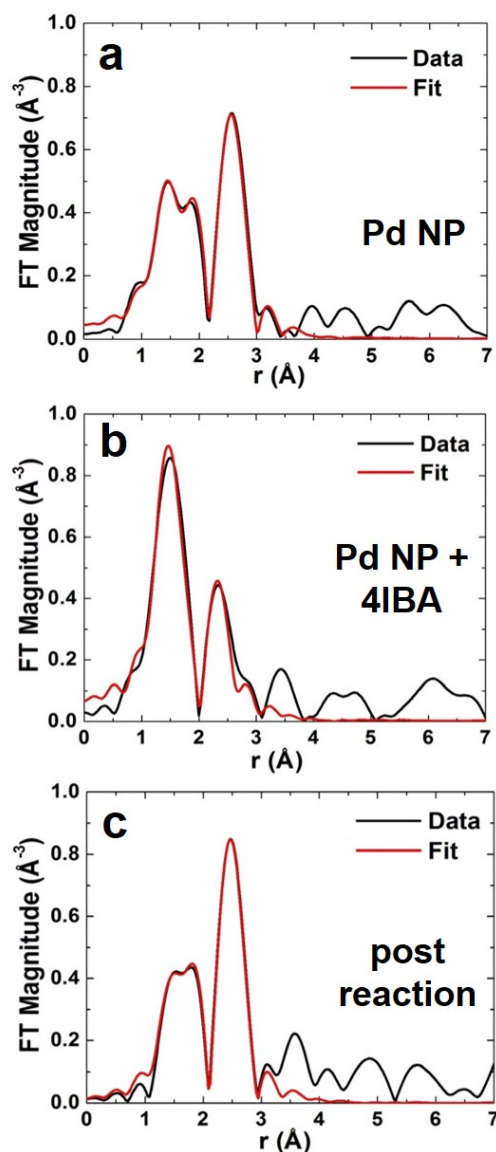


Figure 2.3. EXAFS r-space analysis at the Pd k-edge for (a) Pd NPs before the reaction, (b) Pd NP + 4IBA that isolates oxidative addition, and (c) the materials after Stille coupling completion. The k-ranges for Fourier transforms of k^2 -weighted EXAFS data were: (a) 2 - 10 \AA^{-1} , (b) 2 - 10 \AA^{-1} , and (c) 2 - 9.9 \AA^{-1} .

From the EXAFS analysis, first nearest neighbor CNs were determined to elucidate nanoparticle structural information (Table 1). For the Pd nanoparticles in KOH, Pd-Pd and Pd-C/O/N CNs of 3.6 ± 0.8 and 1.8 ± 0.6 , respectively, were noted, consistent with previous analysis of Pd₄-capped Pd nanoparticles in the solid state.¹³ This indicates that the alkaline environment does not alter the structure, thus any changes to the materials arise from the Stille reaction. Interestingly, the Pd-Pd CNs are lower than expected; for a 2.0 nm Pd nanoparticle, a CN of ~ 9 is anticipated.¹⁰⁵ The present value is likely diminished for two

Experiment	Bond	CN	Bond Length (Å)
Pd NP	Pd – Pd	3.6 ± 0.8 (5.8*)	2.74 ± 0.01
	Pd – C/O/N	1.8 ± 0.6	2.01 ± 0.03
Pd NP + 4IBA	Pd – Pd	not present	not present
	Pd – C/O/N	2.5 ± 0.5	2.00 ± 0.01
	Pd – I	1.0 ± 0.5	2.60 ± 0.01
post reaction	Pd – Pd	5.1 ± 1.1	2.71 ± 0.01
	Pd – C/O/N	0.8 ± 0.4	2.00 ± 0.04
	Pd – I	not present	not present

*Theoretical CN determined from modeling of Pd₄-capped Pd NPs.

Table 1. CNs and bond lengths from EXAFS analysis.

reasons: incomplete reduction of Pd²⁺ and undercoordination of highly disordered surface Pd atoms.⁹⁷ Estimation of the CN values for the peptide-capped Pd nanoparticles can be ascertained from previously published nanoparticle configurations elucidated via Pair Distribution Function analysis.⁹⁷ This study elucidated the complete nanoparticle structure, including both the significant surface metal atom disorder and the orientation of the peptides on the nanoparticle interface. Nearest neighbor analysis using atomistic models of the peptide-covered particle by molecular dynamics simulations at room temperature

indicates average Pd-Pd CN values of 5.8 ± 0.2 as well as a Pd-C/O/N CN of 0.5 ± 0.1 . Note that these values are for the nanoparticles alone without the unreduced Pd^{2+} complex in solution. Even with this, the estimation still remains below the anticipated value, which occurs due to significantly undercoordinated Pd^0 atoms on the nanoparticle interface. When the Pd nanoparticles were studied in the presence of 4-IBA that isolated the oxidative addition step from the complete reaction, no Pd-Pd interactions were evident; both Pd-I and Pd-C/O/N contributions were used to fit the data. To this end, a Pd-I CN of 1.0 ± 0.5 was obtained, while a Pd-C/O/N CN of 2.5 ± 0.5 was noted. For the materials studied after the Stille reaction was complete, a CN change was evident. Here a Pd-Pd and Pd-C/O/N CN of 5.1 ± 1.1 and 0.8 ± 0.4 were calculated, respectively. Note that other theoretical EXAFS contributions were attempted for each sample, but all resulted in a much worse fit.

Taken together, the EXAFS results support a significant structural change in the nanoparticles during oxidative addition. Such a change is consistent with Pd leaching during oxidative addition, forming a Pd^{2+} intermediate in solution. Under the conditions used, both to isolate oxidative addition and drive the full reaction, sufficient 4-IBA is present to fully oxidize all of the Pd in solution; however, when considering the complete reaction, PhSnCl_3 is present in the reaction mixture for transmetalation to occur, driving the reaction forward to completion and quantitative product formation. Note that no byproducts or homocoupling was observed in the reaction, confirming that oxidative addition occurred, rather than a secondary process leading to Pd nanoparticle degradation. Overall, the EXAFS results support the leaching mechanism for Stille coupling driven via oxidative addition. In this regard, the Pd₄-capped Pd nanoparticles were noted to be stable in the basic medium. This indicates that any changes to the material structure are directly

related to the catalytic process and not the conditions. Taking into account the considerations above, a Pd-Pd CN value of 5.8 was computationally derived using atomistic models for these materials prior to the reaction. When the nanoparticles are exposed to the aryl halide only in the absence of PhSnCl_3 (*i.e.* isolation of the oxidative addition step), no Pd-Pd bonds are observed; however, increased Pd-C/O/N bonds and a new Pd-I bond with a CN of ~ 1 are noted. Such effects are consistent with oxidative addition abstracting Pd^{2+} to solution. Should the nanoparticle remain intact with oxidative addition occurring at the metal interface, the complete loss of Pd-Pd bonds would not be observed. Additionally, the increase in the Pd-C/O/N CN could come from the coordination of the phenyl ring to the Pd^{2+} , which cannot be easily distinguished from the peptide. Note that the sum of the CN environment around these Pd species is ~ 3.5 , which is very close to the anticipated value of 4 for such complexes.

When the nanoparticles were examined via EXAFS after the complete Stille reaction was processed, an interesting change in the CN values and bond lengths was noted. The Pd-Pd CN decreased to 5.1 ± 1.1 compared to the apparent CN of 5.8 for the initial nanoparticles, and the bond length significantly contracted (Table 1). A decrease in the Pd-Pd CN and a contraction in the bond length supports the existence of smaller particles in the reaction medium after the Stille coupling process reached completion.¹⁰⁶ Such results are also directly supported by SAXS studies of the same materials (described below). It has been established that as nanoparticle size decreases, the metal-metal bond length decreases for very small materials due to surface strain.^{14, 107} These changes likely arise from the effects of the Stille reaction on the nanoparticles. As recently indicated, the highly disordered atoms at the nanoparticle surface are easily abstracted.^{64, 97} Should only these disordered

surface atoms be leached, a more ordered core of a smaller size would remain, giving rise to a decrease in the Pd-Pd CN values and an overall decrease in the Pd-Pd bond length due to the contracted nanoparticle diameter. Note that precipitation of the Stille product occurs, which likely removes the unreacted Pd²⁺ complex from the solution and the analysis. This is evident due to the dramatic decrease in the Pd-C/O/N value for the nanoparticles after the reaction. Additionally, the leached Pd atoms may aggregate to bulk Pd black upon reaction completion, where a gray precipitate was noted. These precipitates were not likely to be observed via EXAFS as they fell outside the X-ray beam; however, a small fraction may be included, slightly contributing to the Pd-Pd CN. Overall, the EXAFS analysis supports Pd abstraction occurring at the nanoparticle interface, where the highly disordered species are leached and the more ordered core remain. Once the disordered atoms are leached, the reaction ensues from these species; leaching of Pd from the more ordered core is not likely to be favored as compared to oxidative addition at the pre-leached Pd atoms in solution. As such, the core species are potentially less reactive.

While the data supports a Pd atom leaching process, it cannot rule out the abstraction of small Pd clusters as the reactive species in solution. Unfortunately due to the speed of the reaction, it is not possible to monitor the abstraction process via EXAFS *in situ*, thus the exact identity of the reactive species cannot be quantitatively defined. However recent studies on the calculated abstraction energies of Pd atoms on the surface of the disordered peptide-capped Pd nanoparticle suggest that the leaching process occurs for single atoms at the nanoparticle surface.⁹⁷

2.4.4 SAXS Studies

To confirm the proposed reaction-based nanocatalyst changes via oxidative leaching observed by EXAFS, SAXS was employed to probe the Pd nanoparticle size. SAXS studies were conducted using the EXAFS experimental conditions, providing a direct comparison. The resulting scattering patterns were background subtracted, averaged, and subsequently analyzed using the Irena macros in Igor Pro.¹⁰⁰ The pattern for the Pd₄-capped Pd nanoparticles in KOH displayed a broad feature at $\sim 0.2 \text{ \AA}^{-1}$, which can be modeled using

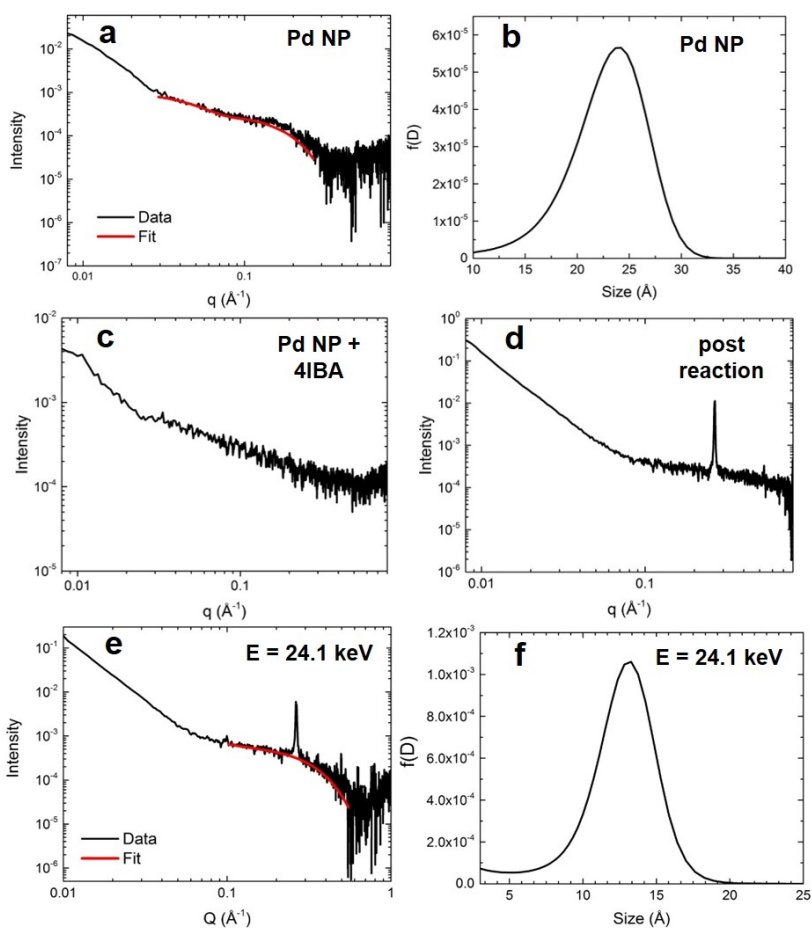


Figure 2.4. SAXS analysis. Part (a) shows the scattering data for the Pd₄-capped Pd nanoparticles in KOH before the reaction with (b) presenting the size distribution. Part (c) displays the scattering data for the Pd nanoparticles in the presence of 4-IBA that isolates oxidative addition, while part (d) shows the scattering analysis for the materials post Stille coupling. Part (e) presents the ASAXS analysis of the nanoparticles post Stille coupling at 24.1 keV, while (f) displays the corresponding size distribution.

a spherical form factor (Figure 2.4a). From this, the size distribution of the nanoparticles is centered at ~ 24 Å (Figure 2.4b), which is only slightly larger than the TEM determined size (2.0 ± 0.3 nm). When the Pd nanoparticles were studied with the addition of the aryl halide that isolated the oxidative addition step, the SAXS pattern exhibited an absence of any tangible nanospherical scatters (Figure 2.4c). Qualitatively, the nanoparticle feature is significantly broadened out, suggesting a complete loss of spherical materials. This is consistent with the EXAFS results that indicated a total loss of Pd-Pd bonds in the presence of 4-IBA due to oxidative-based Pd leaching.

When the Pd nanoparticles were probed after the Stille coupling reaction was fully completed using SAXS, the pattern exhibited a diffraction peak at 0.264 Å⁻¹ and a sharp power-law upturn at low Q (Figure 2.4d). The large diffraction peak corresponded to a d-spacing of 23.8 Å, likely from the crystalline reaction product that precipitated, while the power-law upturn at low Q can be attributed to the sharp interfaces of the crystallized product. Given the substantial concentration differences between Pd and the Stille product (0.3 mol% Pd), a lack of Pd features in the pattern was not surprising. As such, Anomalous SAXS (ASAXS) experiments were performed close to the Pd K-edge to increase the Pd contrast. The ASAXS pattern (Figure 2.4e) still displays the same features of the SAXS pattern, but also exhibits a characteristic feature for spherical nanoparticles at ~ 0.3 Å⁻¹. Modeling of this feature to a spherical form factor resulted in a size distribution centered at ~ 15 Å (Figure 2.4f), which is smaller than the initial Pd nanoparticles. The decreased size supports the presence of smaller nanoparticles, potentially resulting from the core of the original structures once the active disordered species have been leached.

Based on both the EXAFS and SAXS results, a mechanism for Stille coupling catalyzed by peptide-capped Pd nanoparticles is proposed, assuming that both the aryl halide and transmetalation components are present in the reaction mixture (Figure 2.5). First, the Pd nanoparticles are exposed to the aryl halide, which leaches the disordered Pd species (atoms or potentially small clusters) from the nanoparticle surface during oxidative addition, leaving behind a more ordered core. Next, transmetalation occurs, followed by reductive elimination, forming the product and releasing Pd^0 atoms. These pre-leached Pd^0 species are likely to be more reactive for oxidative addition than the Pd atoms on the more

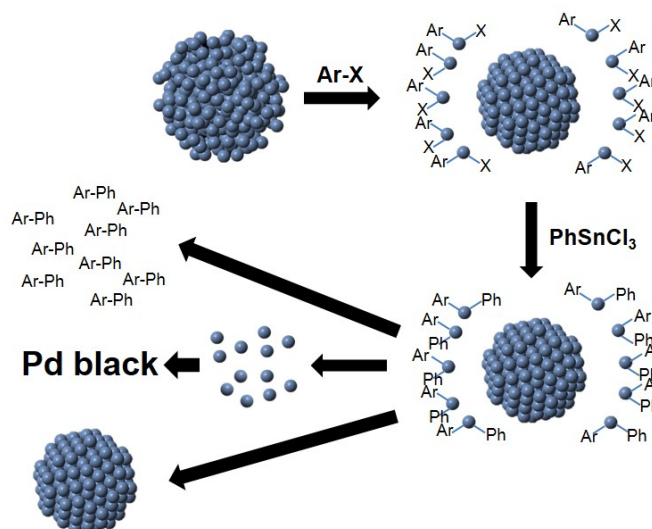


Figure 2.5. Schematic representation of Pd atom leaching Stille coupling mechanism

ordered core.⁶⁴ Under this assumption, the remaining nanoparticle would become less reactive as compared to the abstracted Pd species in solution, suggesting that the pre-leached Pd components would continually cycle through the reaction. The smaller nanoparticle core is likely to be responsible for the decreased Pd-Pd CN and contracted bond length, as observed by EXAFS, and the smaller diameter shown in SAXS. Upon reaction completion, the leached Pd atoms can either aggregate to Pd black, potentially

form new nanoparticles in the reaction medium, or deposit on the nanoparticle cores. Additional studies focused on the reductive elimination step are required to confirm the fate of the leached Pd species.

2.5 Summary and Conclusions

In conclusion, X-ray-based studies have indicated that a leaching mechanism using peptide-capped Pd nanoparticles for Stille coupling is occurring using unique aqueous and room temperature conditions. For this, highly disordered Pd atoms are leached from the nanoparticle surface during oxidative addition by the aryl halide. These leached metal species then drive Stille coupling in solution. Such detailed exploration of the mechanism of this reaction with nanoparticles under sustainable conditions is important to understand the structure/function relationship of these materials. From such a mechanistic understanding using environmentally friendly conditions, the rational design of materials for optimized C-C coupling is possible. Such studies are presently underway in our labs. Furthermore, the X-ray-based approaches described here could be applied to other nanoparticle-driven reactions to elucidate structural/mechanistic effects, providing new routes for nanoparticle reaction analysis.

Chapter 3. Examination of Transmetalation Pathways and Effects in Aqueous Suzuki Coupling Using Biomimetic Pd Nanocatalysts

3.1 Overview of Study

Carbon-carbon (C-C) coupling reactions are ubiquitously used for the generation of advanced chemical species; however, this reactivity remains inefficient and energy intensive. Transitioning such systems toward more sustainable and green conditions would be ideal where Pd nanoparticles represent unique catalysts to achieve this goal. In this chapter, we demonstrate the use of peptide-capped Pd nanoparticles as catalysts for driving Suzuki C-C coupling, focusing specifically on the effects of the transmetalation step in controlling the reactivity. These materials achieved C-C bond formation in water at room temperature using low Pd loadings. Coupling across a variety of mono- and di-substituted substrates was studied, where the reactivity was dependent upon the halogen moiety. Furthermore, studies of the reaction conditions revealed a strong sensitivity to the base identity, suggesting that competing transmetalation pathways and reaction equilibrium effects lead to variations in Suzuki coupling yields. Based upon these results, and in comparison to the Stille coupling reactivity of the same materials, it is suggested that the transmetalation step is important in controlling the overall C-C coupling process. This evidence is significant for nanocatalysts to optimize reactivity under sustainable conditions.

3.2 Motivation

Sustainable chemical transformations are required that minimize energy consumption and limit non-ecofriendly conditions.¹⁰⁸ This is especially important for catalytic processes that

require high reaction temperatures while employing large solvent volumes. Highly used catalytic reactions that could potentially be adapted toward sustainable conditions are carbon-carbon (C-C) couplings such as Suzuki,⁶⁶ Stille,⁶³ and Heck reactions.¹⁰⁹ These systems are extensively used as they can be simple, versatile, and adaptable for the production of C-C bonds at both small and industrial scales.^{60, 67, 110} While these reactions are pervasively employed, the exact mechanism remains unclear. Most C-C couplings follow a three-step process involving oxidative addition, transmetalation, and reductive elimination.⁸³ There is extensive work elaborating on both oxidative addition and reductive elimination,^{83, 111-112} however, details on the transmetalation step are less plentiful.^{70, 72, 113} This is especially true for nanoparticle-driven C-C couplings that have demonstrated significant catalytic reactivity at ambient conditions, including using water as the solvent.^{12, 60} As such, the transmetalation process remains uncertain for such aqueous nanoparticle-based reactions, which could be integral in advancing these systems.

Different transmetalation reagents are used to drive C-C couplings. For instance, Stille coupling employs organostannanes⁶² that produce toxic tin byproducts.¹¹⁰ On the other hand, Suzuki coupling is attractive because it uses less toxic organoboranes for transmetalation. These reagents can be functionalized with numerous chemical moieties, are generally stable, and are commercially available or easily synthesized.^{66-67, 110} Most studies that explore Suzuki coupling use organometallic Pd catalysts that require bulky phosphine ligands to prevent deactivation,¹¹⁴⁻¹¹⁵ however, nanoparticle-based systems have demonstrated remarkable Suzuki reactivity in the absence of phosphines.^{80, 86, 116-117} These nanomaterials operate in water-based solvents at room temperature, thus making them model green catalysts to explore structure/function relationships.

Suzuki coupling using nanomaterials has been suggested to be driven by a Pd atom leaching process.^{80, 95, 118} This mechanism begins with aryl halide oxidative addition that drives the leaching to form a Pd²⁺ intermediate in solution. Next, transmetalation occurs, releasing the halogen and positioning a nucleophile onto the Pd²⁺ complex. This is then followed by reductive elimination to liberate the product and regenerate the Pd⁰.⁸³ This Pd⁰ component can then be recycled through the reaction should sufficient reagent be present, quenched by the remaining particles, or aggregated to form Pd black if excessive Pd⁰ leaching has occurred. While research has been focused on the oxidative addition step for Pd leaching,^{16, 80, 95} transmetalation has been understudied using nanocatalysts, which may be important for the leaching process. For Suzuki coupling specifically, the base in the reaction may play a large role as it can coordinate to the boronic acid transmetalation reagent to generate a tetracoordinate anionic boronate.^{67-68, 71, 110, 119} Formation of this species could increase the nucleophilicity of the boron center to facilitate organic group transfer to the active Pd²⁺-halide intermediate.⁶⁷ The base has also been suggested to participate in another role in which an OH⁻ species exchanges with the halide on the oxidative addition Pd²⁺ intermediate prior to transmetalation.^{70, 72, 113} In this case, the newly formed aryl-Pd-OH species is thought to be the active component for transmetalation, reacting with a neutral boronic acid. Compounding this issue, both the boronic acid/boronate species and the Pd²⁺-halide/Pd²⁺-OH species are in equilibrium, thus all four species are likely to be present in a single reaction system. As a result, experimentally determining the species involved in the reaction remains difficult, especially when examining nanoparticle-driven systems.

Peptide-based approaches represent new methods for the generation of catalytic nanostructures.^{12, 15, 45, 47, 50} To this end, we have employed the Pd4 peptide (TSNAVHPTLRHL) with affinity for Pd.¹² Using this biomolecule, ~2 nm Pd nanoparticles can be produced where the peptides cap the materials via anchoring through the histidines.^{9, 12-13} These materials have shown high reactivity for aqueous Stille coupling where quantitative yields were achieved at 0.005 mol% Pd with a turnover frequency (TOF) of 2234 ± 99 mol product (mol Pd \times h)⁻¹.¹⁵ Further studies of the reaction mechanism suggested that a catalytic Pd leaching process was occurring during oxidative addition.¹⁶ Interestingly, modification of the amino acids in the peptide can have significant implications on both the size and functionality of nanocatalysts.^{13, 15, 18-19} Taken together, these materials represent model bio-inspired nanocatalysts with optimized reactivity under sustainable conditions. Expanding their catalytic capabilities toward new C-C couplings could provide important mechanistic information that could be used to understand and optimize nanoparticle reactivity.

In Chapter 2, the mechanism of Stille C-C coupling using Pd4-capped Pd nanoparticles was explored, with an in-depth focus on the oxidative addition step. Due to the similar nature of Stille coupling with Suzuki coupling, we were interested in exploring the reactivity for Suzuki C-C coupling, with a concentration on the transmetalation step as this step differentiates the two reactions. Thus, in this chapter, we demonstrate the use of the Pd4-capped Pd nanoparticles for Suzuki C-C coupling. These materials were reactive in water at room temperature, where the effects of the transmetalation step were systematically explored. For this, the particles were employed as catalysts for a model Suzuki coupling of 4-iodobenzoic acid with phenylboronic acid (PhB(OH)₂) to generate

biphenylcarboxylic acid. The reaction was processed at room temperature in a basic aqueous solution, where the base was varied across three species: KOH, Na₂CO₃, and K₃PO₄. Interestingly, the base identity and concentration played an important role in the reactivity, where the catalytic functionality was a function of the base strength. Such effects are likely due to competing transmetalation pathways developed as a result of equilibria established in the system, altering the reactivity, which were examined using ¹¹B NMR and control nanocatalysts. Once examined, the use of the biomimetic nanocatalyst for Suzuki coupling was expanded to additional mono- and di-substituted aryl halide substrates that indicated preferential reactivity for specific halogens. While these structures did not deliver the fastest reactivity, they do provide important information concerning the reaction mechanism for nanoparticle-driven C-C coupling systems that operate in water at room temperature. This mechanistic level can be accessed via comparison of the presently reported Suzuki reactivity with the known catalytic activity of these materials for Stille coupling^{12, 16} that varied the transmetalation step only. Such information is critically important in the development of sustainable catalytic systems and nanotechnologies.

3.3 Methods

3.3.1 Chemicals

K₂PdCl₄, sodium citrate, boric acid, and PhB(OH)₂ were obtained from Sigma, while KOH, K₃PO₄, NaBH₄, *t*-butylphenol, *N*-methyl-*N*-(trimethylsilyl)-trifluoroacetamide (MSTFA), D₂O, and CDCl₃ were supplied from Acros. 4-iodobenzoic acid was acquired from TCI America. Diethyl ether, NaCl, Na₂CO₃, Na₂SO₄, *N,N*-dimethylformamide (DMF),

dichloromethane (DCM), methanol, and acetonitrile were obtained from BDH, while HCl was supplied by EMD. Finally, all Fmoc-protected (Fmoc = 9-fluorenylmethoxycarbonyl) amino acids and resins for peptide synthesis were purchased from Advanced Chemtech. All solvents and reagents were used as received without additional purification. Finally, 18 M Ω •cm water was used throughout (Millipore, Ultrapure Synergy UV).

3.3.2 Peptide-Capped Nanoparticle Synthesis

The Pd4 peptide was synthesized employing standard solid-phase Fmoc protocols⁹⁸ using a TETRAS synthesizer (Creosalus). The peptides were purified using HPLC and confirmed using MALDI-TOF. Once confirmed, the sequences were employed for nanoparticle synthesis using described methods.¹² Briefly, 0.025 mL of freshly prepared, aqueous 0.10 M K₂PdCl₄ and 0.10 mL of 10.0 mg/mL Pd4 were co-dissolved in 4.775 mL of water. This solution was allowed to sit for 30 min, after which 0.10 mL of freshly prepared 0.10 M aqueous NaBH₄ was added. The solution was swirled to mix and then allowed to stand for 60 min.

3.3.3 Citrate-capped Nanoparticle Synthesis

Citrate-capped Pd nanoparticles were prepared based on published methods with slight modifications.¹²⁰ For this, 7.5 μ L of 0.10 M sodium citrate was added to 1.38 mL of water while stirring. 37.5 μ L of 0.10 M K₂PdCl₄ was then added and the solution was allowed to stir for 30 min. Next, 75 μ L of freshly prepared 0.10 M NaBH₄ was added while stirring. The reaction was allowed to reduce for 30 min.

3.3.4 Suzuki Coupling

The reaction of 4-iodobenzoic acid with PhB(OH)₂ in 0.50 M K₃PO₄ is described; however, identical reaction conditions were applied with the different bases at the desired concentration. Note that the indicated base concentration reflects the reaction concentration. In a 20 mL glass vial, 0.5 mmol of 4-iodobenzoic acid and 0.6 mmol of PhB(OH)₂ were co-dissolved in 4.0 mL of 1.0 M K₃PO₄. Once fully dissolved, a sufficient volume of Pd nanoparticles was added to reach the desired concentration: 1.00 mL (0.10 mol% Pd), 500 μL (0.05 mol% Pd), 100 μL (0.01 mol% Pd), 50 μL (0.005 mol% Pd), 10 μL (0.001 mol% Pd), 5.0 μL (0.0005 mol% Pd), or 1.0 μL (0.0001 mol% Pd). To the reaction, additional water was added prior to nanoparticle addition, so that the final volume was 8.0 mL. The vials were then capped and the mixtures were allowed to stir at room temperature for 24.0 h. The reactions were then quenched with 50 mL of 5.0% HCl and extracted three times using 30 mL of diethyl ether. Next, the organic layers were collected, washed twice with 20 mL of a saturated NaCl solution, and then dried with anhydrous Na₂SO₄. 0.5 mmol of *t*-butylphenol was added to the product as the internal standard, after which the ether was removed. The resulting product was quantitated using ¹H NMR and GC-MS,¹² described below.

3.3.5 TOF Studies

To determine TOF values, the reaction was increased five fold. In a 100 mL round bottom flask, 2.5 mmol of 4-iodobenzoic acid and 3.0 mmol of PhB(OH)₂ were dissolved in a total of 40.0 mL of base and water to reach the desired base concentration. Once dissolved, 2.50

mL of the Pd nanoparticles were added (0.05 mol% Pd). 4.0 mL aliquots were then extracted and quenched with 25 mL of 5.0% HCl at selected time points, followed by product quantitation. Due to reactivity differences, the K_3PO_4 and Na_2CO_3 systems were monitored over 4.5 h, while KOH-based reactions were studied for 9.0 h.

3.3.6 Recycling Studies

To study the recyclability of the nanocatalysts, a two-extraction system was processed. For this, standard 8.0 mL Suzuki reactions that coupled 4-iodobenzoic acid with $PhB(OH)_2$ were prepared using 0.50 M K_3PO_4 and 0.50 M Na_2CO_3 at 0.05 mol% Pd. After 24.0 h, a 4.0 mL aliquot was extracted and quantitated. To the remaining 4.0 mL of the initial system, sufficient 4-iodobenzoic acid and $PhB(OH)_2$ were added to re-attain a 0.05 mol% Pd loading. This reaction proceeded for 24.0 h, followed by product quantitation.

3.3.7 Characterization

GC-MS analysis was conducted using an Agilent 6850 gas chromatograph (GC), equipped with a 5975C mass spectrometer (MS). Extracted and dried samples with carboxylic acid or phenol functional groups were prepared by reacting ~2 mg of the product in 200 μ L of MSTFA for 2.0 h. The samples were then diluted in DCM at ~1 mg/mL prior to analysis. 1H NMR spectra were obtained using a Bruker Advance Broadband 400 MHz NMR. Samples were prepared by dissolving ~1 mg of the product in 1.0 mL of $CDCl_3$, followed by transferring the solution into a 5 mm NMR tube. For reactions that generated biphenylcarboxylic acid as the product, the *t*-butylphenol internal standard peak integration at δ 6.8 ppm was compared with the product peak integration at δ 8.2 ppm to determine

product yields.¹² For all other reactions using different aryl halide substrates, appropriate peaks were selected for product quantitation that clearly arose from the starting materials, product, and/or internal standard. Using these characterization methods, average yields and TOF values are presented \pm one standard deviation derived from triplicate analyses. TEM images were obtained either using a JEOL 2010F or a Phillips CM200 transmission electron microscope operating at 200 kV. The samples were prepared by depositing 5.00 μ L of the nanomaterial solution onto a 400 mesh Cu grid (EM Sciences). The samples were allowed to dry overnight prior to imaging.

3.3.8 ¹¹B NMR Experiments

¹¹B NMR spectra were obtained using a Bruker Advance Broadband 400 MHz NMR. Frequencies were recorded with respect to a standard of 0.10 M boric acid in D₂O. 0.10 M solutions of PhB(OH)₂ were prepared in the base solutions in D₂O at the concentrations studied for the reactions. These samples were stirred for 1 h before analysis.

3.4 Results and Discussion

Studies of the Suzuki coupling reactivity for the peptide-capped Pd nanoparticles were probed to determine mechanistic effects for C-C coupling, as compared to previous results for Stille coupling.¹² Remarkably, few studies focus on using identical materials for these similar reactions to probe mechanisms, where the only difference is during transmetalation. It has been suggested that nanoparticle-driven C-C coupling follows a metal leaching process,^{16, 80, 95} whereby Pd species are released during oxidative addition to drive the reaction in solution. As such, transmetalation could be substantially influenced by both the

replaced by a broad absorbance characteristic of Pd nanoparticles.¹²¹ Note that a minor amount of unreduced Pd²⁺ is likely to be present in the sample.¹³ Transmission Electron Microscopy (TEM) analysis of the final materials (Figure 3.1b) confirmed the production of spherical Pd nanoparticles of 1.9 ± 0.4 nm in diameter. The materials remained stable for several days when left out on the benchtop. These results confirm the production of stable Pd nanoparticles of an ideal size for catalysis that maximizes the surface-to-volume ratio.

Prior to catalytic analysis, the solubility of the 4-iodobenzoic acid and PhB(OH)₂ substrates in the different base solutions was determined over a base concentration range of 0.10 to 2.25 M (see Chapter 6.3, Table 6). Note that the presence of base is required to deprotonate the carboxylic acid moiety of 4-iodobenzoic acid to make it soluble in water. The molar ratios of 4-iodobenzoic acid to base were 1:1.6, 1:8, 1:12, 1:24, 1:30, and 1:36 at base concentrations of 0.1, 0.5, 0.75, 1.5, 1.87, and 2.25 M, respectively. From this, the substrates were found to be fully soluble in KOH over the entire range, while they were only soluble up to a base concentration of 0.75 M of Na₂CO₃ and K₃PO₄. Once the solubility was determined, initial Suzuki coupling analyses were conducted for the three different systems: monobasic (KOH), dibasic (Na₂CO₃), and tribasic (K₃PO₄). For this reaction (Figure 3.2a), 4-iodobenzoic acid was mixed with PhB(OH)₂ in the aqueous base solution, to which the Pd₄-capped Pd particles were added at a metal loading of 0.05 mol% Pd. After 24.0 h of reaction, the biphenylcarboxylic acid product was extracted and quantitated to determine the reaction yield as an effect of the base concentration and identity (Figure 3.2b). When the reaction was processed in 0.10 M KOH, a product yield of $62.2 \pm 14.7\%$ was observed. As the base concentration increased to 0.50 M, the product

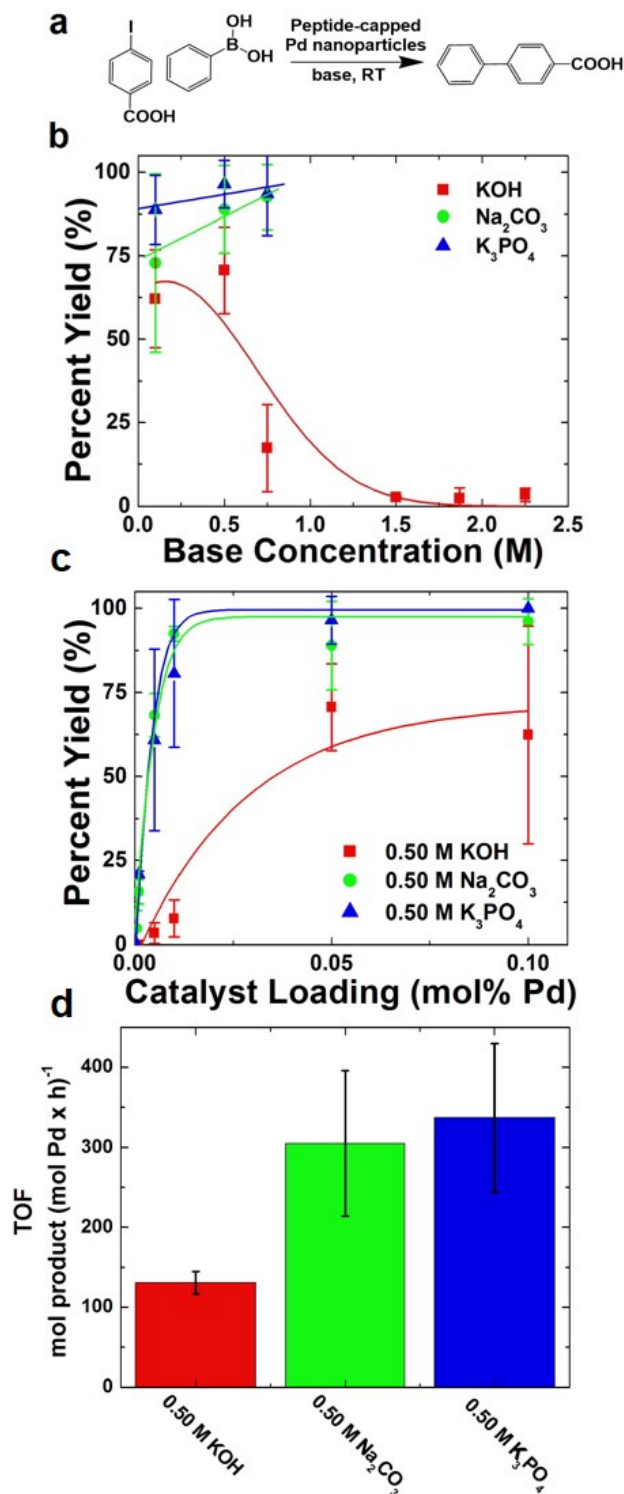


Figure 3.2. Suzuki coupling analysis as a function of the base. Part (a) presents the model Suzuki reaction, while part (b) displays the product yield at a catalyst loading of 0.05 mol% Pd over the base concentrations studied. Part (c) shows the catalyst loading analysis using the Pd₄-capped Pd nanoparticles in 0.5 M base, while part (d) is the catalytic TOF analysis at 0.05 mol% Pd in 0.5 M base.

yield was similar, with a value of $70.7 \pm 13.0\%$; however, at a KOH concentration of 0.75 M, the yield substantially decreased to $17.4 \pm 13.0\%$. At higher base concentrations, negligible product yields were isolated over the time frame of the study, even though the two substrates were fully soluble. As is evident, quantitative product yields were never observed with KOH, and high base concentrations actually inhibited the reaction. These results contrast the reaction yields for the same Pd₄-capped Pd nanoparticles that provided quantitative product yields in 2.25 M KOH for Stille coupling using 4-iodobenzoic acid with PhSnCl₃ as the transmetalation reagent.¹² This indicates that the base can significantly affect the overall reaction, most likely at transmetalation, as identical oxidative addition and reductive elimination pathways are anticipated for the Suzuki and Stille reactions using these particles.

When considering Na₂CO₃ and K₃PO₄, a different trend in reactivity was observed, with higher product yields as compared to KOH. Note that product yields could only be determined up to a base concentration of 0.75 M due to reagent solubility. For instance, at a base concentration of 0.10 M, the Na₂CO₃ system demonstrated a product yield of $72.9 \pm 26.7\%$, while for the K₃PO₄ base, a product yield of $88.8 \pm 10.3\%$ was determined. At the two higher base concentrations studied, 0.50 M and 0.75 M, slightly increased production was observed for these two systems that approached quantitative yields. This is especially important at the 0.75 M base concentration, where product yields of $92.6 \pm 9.8\%$ and $93.7 \pm 12.6\%$ were determined for the Na₂CO₃ and K₃PO₄ systems, respectively. Such values are significantly larger than those observed for the KOH base that demonstrated greatly diminished reactivity at this concentration. This suggests that the identity and concentration of the base can dramatically impact the C-C coupling reaction.

From this initial analysis, it was noted that maximal reaction efficiency occurred at a 0.50 M base concentration for all three systems. Note that these base concentrations were those that gave rise to the highest product yield for each system, but that lower yields were still observed for the KOH system. As such, this base concentration was employed for all subsequent experiments to explore and optimize the reactivity, including catalyst loading studies, which are presented in Figure 3.2c. For these experiments, the Pd nanoparticle catalyst concentration was varied from 1.0×10^{-4} to 0.10 mol% Pd for the model Suzuki coupling reactions, where the product yield was determined after 24.0 h. Considering the monobasic sample (KOH), in general, diminished product yields were determined compared to the multiply charged bases. For this system, reactivity was first observed at a loading of 5.0×10^{-3} mol% Pd with a product yield of $3.5 \pm 3.1\%$ that increased to $70.7 \pm 13.0\%$ at 0.05 mol% Pd. At subsequently higher catalyst loadings, comparable product yields were isolated. Transitioning to the dibasic Na_2CO_3 system, increased product generation was noted that reached saturation at near-quantitative yields. For instance, at a Pd loading of 5.0×10^{-4} mol%, a product yield of $4.9 \pm 5.2\%$ was determined. This value linearly increased to $92.5 \pm 2.2\%$ at 0.01 mol% Pd, where product saturation was evident. For the triply charged K_3PO_4 base, similar results were observed as compared to the Na_2CO_3 system. Here, at a Pd loading of 1.0×10^{-3} mol%, a reaction yield of $20.9 \pm 0.9\%$ was quantitated that again saturated at a $96.5 \pm 7.1\%$ yield with a catalyst loading of 0.05 mol% Pd. Overall, higher yields were determined from the multiply charged bases that reached near quantitative product generation at Pd loadings ≥ 0.05 mol% Pd. Note that no product was generated when the reaction was processed in the absence of catalyst and no evidence of homocoupling was noted.

To further probe the effects of the base, TOF studies were conducted to determine the catalytic efficiency of the three different systems. For this, a scaled-up model Suzuki reaction at a Pd loading of 0.05 mol% was analyzed for product yield as a function of time. A loading of 0.05 mol% Pd was selected as maximized product yields were observed for all three reaction systems at this catalyst concentration. As shown in Figure 3.2d, the different bases produced strikingly different TOF results, indicating altered reaction efficiencies. To this end, the KOH system demonstrated a TOF value of 131 ± 14 mol product $(\text{mol Pd} \times \text{h})^{-1}$. In contrast, the K_3PO_4 system displayed the highest TOF of 337 ± 93 mol product $(\text{mol Pd} \times \text{h})^{-1}$, while the Na_2CO_3 system presented a similar value at 305 ± 91 mol product $(\text{mol Pd} \times \text{h})^{-1}$. These results reflect those observed for the catalytic loading studies where higher reactivity was noted for the dibasic and tribasic systems over the monobasic KOH reaction. Plots of the product yield of biphenylcarboxylic acid over time for all three bases are shown in Chapter 6.3, Figure 6.2

In order to examine the efficiency of the peptide-capped Pd nanoparticles in the Suzuki system, recycling studies were also conducted in 0.50 M K_3PO_4 and Na_2CO_3 at 0.05 mol% Pd. For these studies, the reactions were run for 24.0 h, after which an aliquot was extracted to quantitate the product yield. To the remaining, unquenched reaction, fresh 4-iodobenzoic acid and $\text{PhB}(\text{OH})_2$ were added so that a 0.05 mol% Pd reaction system was regenerated. This reaction was processed for another 24.0 h. Once complete, the system was quenched and the product yield was determined. A schematic description of these recycling studies is shown in Chapter 6.3, Figure 6.3a. For both systems after the initial 24.0 h reaction time frame, quantitative product yields were determined; however, only $77.9 \pm 11.1\%$ and $70.7 \pm 11.6\%$ product yields were observed in the second reaction time frame using the 0.50 M

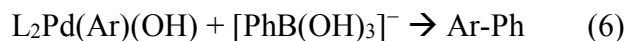
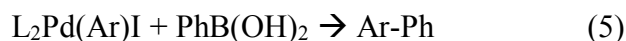
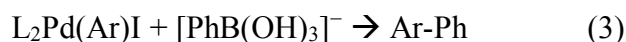
K₃PO₄ and Na₂CO₃ systems, respectively (Chapter 6.3, Figure 6.3b). This suggests that a degree of catalyst deactivation occurs after the initial reaction, which may arise from the proposed leaching process that can generate unreactive Pd black, leading to lower product yields.¹⁶

From the catalytic analysis, Suzuki coupling using the Pd₄-capped Pd nanoparticles revealed a significant base effect that controlled the overall coupling reactivity. Such effects are consistent with previous literature precedent using organometallic catalysts that suggested increased reactivity from dibasic and tribasic derived systems;¹²²⁻¹²⁵ however, the effect of such differences have not been examined for nanoparticle-driven reactions that occur in water. As such, it is important to elucidate these fundamental effects to optimize the reaction for eco-friendly and energy efficient sustainable conditions. For the present system, when dibasic and tribasic species were employed, a significant increase in reactivity was observed. This suggests that polybasic bases facilitated more efficient Suzuki coupling as compared to their monobasic counterpart, KOH. The increased reactivity for the polybasic species indicates that the difference in the strength of the base may affect the reaction, particularly at the transmetalation step. The hydroxide species formed from the base can react with the PhB(OH)₂ and Pd²⁺ catalytic intermediates through two equilibrium reactions, shown below:



From this set of equilibria, four different possible reactions are possible (3-6), as described below; however, only two of the reaction schemes (3 and 4) have been shown to facilitate

transmetalation for product turnover in Suzuki coupling, while reactions 5 and 6 are anticipated to be unreactive for product generation:



As shown previously,^{67-68, 71, 110, 119} four-coordinate boronates $\text{PhB}(\text{OH})_3^-$ can be generated through reactivity between $\text{PhB}(\text{OH})_2$ and the hydroxides produced from a base (reaction 2), where this species can participate in transmetalation using $\text{L}_2\text{Pd}(\text{Ar})\text{I}$ as the catalytic species (reaction 3). Prior studies using organometallic catalysts indicated that such a change in the boronic acid charge and structure was required for the Suzuki coupling to occur.^{67-68, 119} For instance, in computational studies by Maseras and colleagues, the addition of the base into the tricoordinate boronic acid to form the tetracoordinate boronates was calculated to have a minimal energy barrier.⁷¹ Such computational results are supported by the studies of Dewar and Jones, which demonstrated that boronic acids indeed form a tetrahedral species under basic conditions using ^{11}B NMR.¹²⁶ Additionally, Smith *et al.* have shown a direct correlation between Suzuki product formation and the amount of K_2CO_3 added.⁶⁸

Conversely, recent studies have suggested that hydroxide ions could also coordinate to the catalyst, producing an $\text{L}_2\text{Pd}(\text{Ar})(\text{OH})$ intermediate (reaction 1), which then interacts with a neutral boronic acid during transmetalation (reaction 4).^{70, 72, 113} Amatore *et al.* have shown that the role of the base is not to coordinate to the boronic acid, but rather to replace the halide on the oxidative addition intermediate to form the $\text{L}_2\text{Pd}(\text{Ar})(\text{OH})$ species.^{70, 113}

These works theorize that the other suggested pathway that employs a negatively charged boronate is less favorable and can hinder coupling.^{70, 113} Furthermore, Carrow and Hartwig have conducted studies isolating each suggested pathway of the reaction (reactions 3 and 4), which showed that reaction 4 results in higher rates as compared to reaction 3; however, catalytic turnover was still observed for the $L_2Pd(Ar)I + [PhB(OH)_3]^-$ pathway.⁷² It has also been shown that $L_2Pd(Ar)(OH)$ does not react with boronate (reaction 6),¹¹³ thus limiting the possible transmetalation pathways of the present system to reactions 3 and 4.

To ascertain which pathway the nanoparticle-based system employs during transmetalation, ^{11}B NMR studies (Figure 3.3) were used to elucidate the boronic acid structure in the aqueous reaction. Note that most studies that focus on this process employ organic-containing solvents, thus pure aqueous reaction systems must be examined to isolate reaction pathway differences based upon the solvent. For this $PhB(OH)_2$ was dissolved in basic solutions prepared from the three selected bases in D_2O to a concentration of 0.10 M. As a control, when $PhB(OH)_2$ was dissolved in D_2O in absence

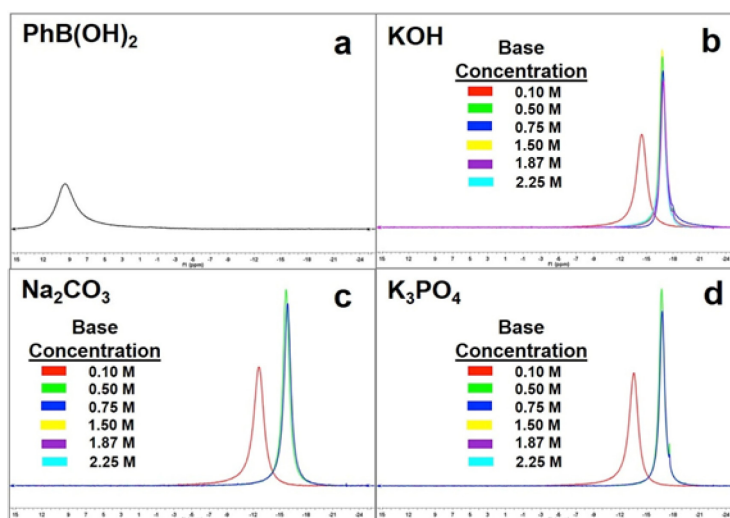


Figure 3.3. ^{11}B NMR of 0.1 M $PhB(OH)_2$ over the range of base concentrations studied. Part (a) presents the analysis in D_2O only, while parts (b-d) present the analysis in KOH , Na_2CO_3 , and K_3PO_4 , respectively.

of base, a singlet with a chemical shift of 9.6 ppm was observed arising from the tricoordinate species. When the boronic acid was studied in the basic D_2O solutions, a significant peak shift was noted. For instance, when dissolved in a 0.1 M base solution, a singlet peak at ~ 12.7 ppm was noted for all three bases. This peak then shifts to ~ 16.8 ppm for all of the selected bases at higher concentrations. As previously observed, this unique peak shifting phenomena arises due to the equilibrium event between the neutral tricoordinate $PhB(OH)_2$ and the tetracoordinate $[PhB(OH)_3]^-$ (reaction 2).^{72, 127} In this regard, as the concentration of base increases, the concentration of the boronate increases (due to the increased hydroxide present) and thus the peak shifts further from the boronic acid peak at 9.6 ppm. This indicates that the boronate is present in all three systems under the reaction conditions, suggesting that other factors beyond the boronate structure, including the formation of the hydroxylated Pd^{2+} catalytic intermediate, lead to reaction diminishment for the KOH system.

While it is evident that the tetracoordinate boronate is present in all three reaction systems at roughly similar concentrations, a secondary event must be occurring in the KOH reaction to lead to diminished reactivity (Figure 3.4). The biggest difference between the monobasic KOH and the polybasic Na_2CO_3 and K_3PO_4 bases is the fact that the former is a strong base, while the latter two are weak bases with known K_b values.¹²⁸ In this regard, the weak bases are in equilibrium with the OH^- in solution, thus competing with the boronate and Pd^{2+} species for these hydroxides. As such, for KOH, the amount of free and reactive hydroxide is higher at all base concentrations as compared to the Na_2CO_3 and K_3PO_4 systems, thus causing equilibrium shifts. In this regard, the ^{11}B NMR indicates that the

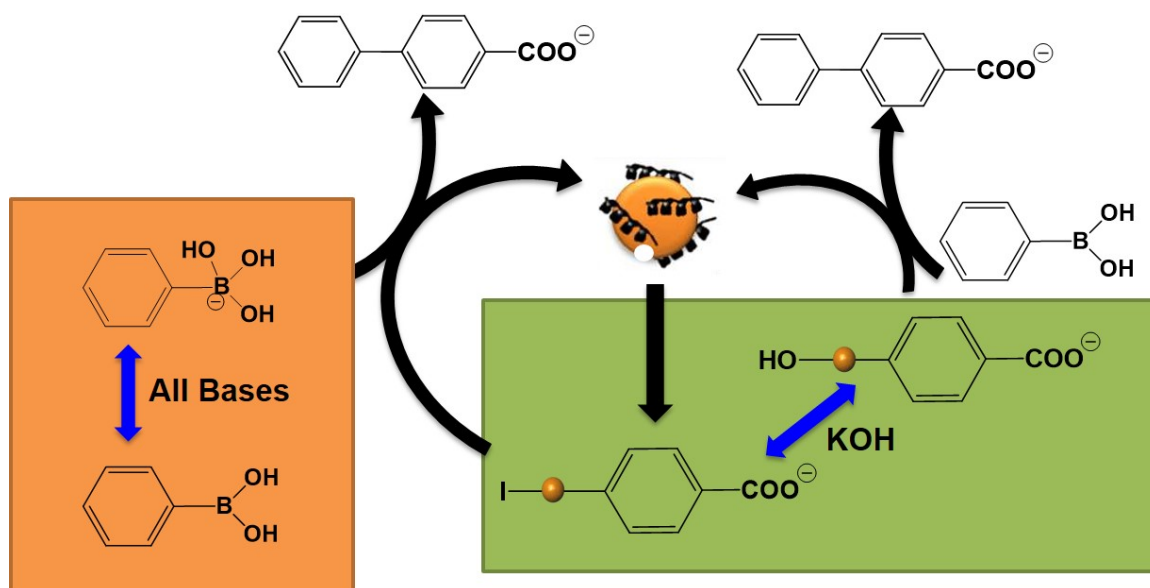


Figure 3.4. Schematic representation of competing transmetalation pathways and associated equilibria.

boronate species concentration was roughly equivalent for all reaction mixtures (Figure 3.4, orange box), thus the differences between the mono and polybasic systems likely arises at the hydroxylation of the Pd^{2+} intermediate (reaction 1). Based upon the equilibria and observed reactivity, it is likely that the $\text{L}_2\text{Pd}(\text{Ar})(\text{OH})$ is higher for the KOH system as compared to the Na_2CO_3 and K_3PO_4 systems, where the $\text{L}_2\text{Pd}(\text{Ar})\text{I}$ species is more prevalent. Should this reaction mixture be present in the KOH system, the $[\text{PhB}(\text{OH})_3]^-$ species would need to shift back to $\text{PhB}(\text{OH})_2$ for the Suzuki coupling to progress via reaction 4 or the $\text{L}_2\text{Pd}(\text{Ar})(\text{OH})$ would need to shift to $\text{L}_2\text{Pd}(\text{Ar})\text{I}$ for the coupling to occur via reaction 3. As such, this reaction system is highly dominated by equilibria processes that are shifted away from reaction mixtures amenable for Suzuki coupling. For the polybasic systems, a higher concentration of $\text{L}_2\text{Pd}(\text{Ar})\text{I}$ is present due to the equilibrium established with the PO_4^{3-} and CO_3^{2-} anions. As such, a higher stoichiometric ratio of $\text{L}_2\text{Pd}(\text{Ar})\text{I}$ and $[\text{PhB}(\text{OH})_3]^-$ are present, thus driving Suzuki coupling via reaction 3. While

the rate of this reaction is slower compared to the rate for the $L_2Pd(Ar)(OH)$ -based reaction (reaction 4), less degrees of equilibrium shifting are required, giving rise to the higher reactivity for the polybasic systems over the monobasic KOH reaction. Unfortunately, due to the fast reaction, very low nanoparticle concentration, and likely leaching event at the nanoparticle surface, NMR studies could not be completed to investigate the Suzuki reaction itself driven by the Pd nanoparticles. As such, further high resolution, *in situ* spectroscopic studies are required to fully elucidate the reaction mechanism; however, the presented differences are plausible due to the ^{11}B NMR and reactivity observations. It is worth pointing out that at very high KOH concentrations, the Suzuki coupling reaction is completely inhibited. This likely arises because both equilibria of reactions 1 and 2 are shifted to have high concentrations of $L_2Pd(Ar)(OH)$ and $[PhB(OH)_3]^-$, which cannot react in the Suzuki coupling, further supporting these equilibrium effects on the reactivity. Note that in all of the reaction systems, 4-iodobenzoic acid is deprotonated, consuming a fraction of the hydroxides. Furthermore, the reactivity does not correlate simply to pH as a reflection of the hydroxide concentration (Chapter 6.3, Figure 6.4), supporting equilibria effects playing a more dominant role in the reactivity.

To further examine how equilibria effects can alter the reaction system, a mixture of two bases in the reaction was explored. For this, a mixture of KOH and K_3PO_4 was used at a total base concentration of 0.5 M that varied from 100% KOH to 100% K_3PO_4 over set ratios. As shown in Chapter 6.3, Figure 6.5, as the concentration of KOH in the reaction increased, the percent yield of the Suzuki coupling product decreased. This further supports the equilibrium effects discussed above in that as the concentration of K_3PO_4 decreases,

the amount of weak base decreases, minimizing the equilibrium effects associated with it, thus shifting the reaction more toward the KOH system with lower degrees of reactivity.

Beyond the reaction studies for Suzuki coupling, the Pd4-capped Pd nanoparticles used here have also been studied for Stille coupling,¹²⁻¹³ thus serving as a direct comparison for understanding the observations herein. In that work, the Stille coupling of 4-iodobenzoic acid with PhSnCl₃ to prepare biphenylcarboxylic acid was extensively studied.¹² Note that the same aryl halide and final product are present in both systems, thus the only difference between these two reactions arises during transmetalation. For Stille coupling, a significantly higher TOF value of 2234 ± 99 mol product (mol Pd × h)⁻¹ has been achieved with quantitative product yields using Pd loadings of 0.005 mol%.¹⁵ Interestingly, these reactions were run at a KOH base concentration of 2.25 M, well above the base concentration where product formation for the Suzuki system was inhibited. Since the same oxidative addition and reductive elimination steps are occurring between these two reactions, the differences in reactivity must arise from the transmetalation step. This suggests that for the Pd4-capped nanoparticle system, transmetalation may be rate limiting and that the effects of secondary species in the reaction mixture play an important role during this specific process. Should the base affect either oxidative addition or reductive elimination, more similar degrees of reactivity would be anticipated for these different reactions. As such, the changes in reactivity are most likely affecting transmetalation, supporting the role of the base in the equilibrium effects of reactions 1-6.

To more fully understand the results of the nanoparticle catalysts, control studies were performed using citrate-capped Pd nanoparticles. These materials were similar to the peptide-capped structures, being spherical in shape with a diameter of 5.7 ± 1.3 nm

(Chapter 6.3, Figure 6.6). To this end, reaction product yields and TOF values were determined using this system at a metal loading of 0.05 mol% Pd at the selected base concentrations. For these particles (Figure 3.5a), a very similar reactivity trend was observed where Na_2CO_3 and K_3PO_4 displayed the highest yields of near-quantitative values after 24.0 h of reaction: $91.9 \pm 14.0\%$ and 100% , respectively. Furthermore, the yields from the KOH system were greatly diminished to $2.9 \pm 0.7\%$. TOF studies were also conducted using the citrate-capped Pd materials (Figure 3.5b) where K_3PO_4 was determined to be the most efficient basic system with a TOF value of 169 ± 8 mol product $(\text{mol Pd} \times \text{h})^{-1}$. The Na_2CO_3 derived reaction demonstrated a slightly lower TOF of 119 ± 6 mol product $(\text{mol Pd} \times \text{h})^{-1}$. Note that both of these TOFs are approximately half the values observed for the peptide-capped Pd nanoparticle catalyzed reaction. Unfortunately, due to the very low reaction yields for the KOH system, an accurate TOF value could not be ascertained.

Taken together, these control studies provide additional key information concerning the catalytic activity of the Pd4-capped materials. First, the reactivity for the biomimetic

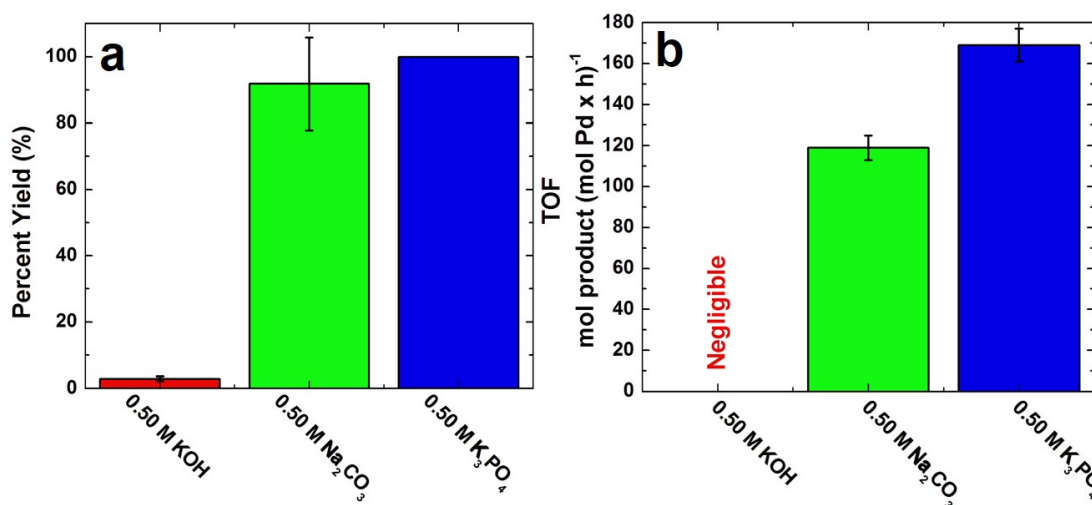
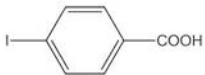

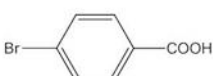

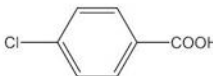







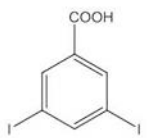
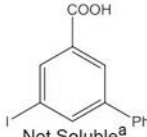
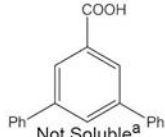
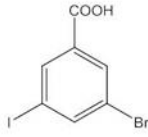
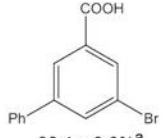
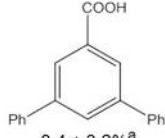


Figure 3.5. Analysis of Suzuki coupling using the citrate-capped Pd nanoparticles. Part (a) presents the 24 h product yields using a Pd loading of 0.05 mol% in 0.5 M base, while part (b) displays the corresponding TOF values for systems with significant reactivity.

materials is enhanced as compared to the citrate-capped structures. This suggests that both the size of the Pd4-based system, and potentially the surface structure, are enhanced as compared to the larger particles. In this regard, the peptide-capped materials present a higher surface-to-volume ratio as compared to the larger citrate-prepared particles. Since the same Pd concentration was used in both systems, a greater metallic surface was presented for the peptide-based structures, thus assisting in increasing the reactivity. Additionally, substantially different surface structures from the passivating ligands are presented to solution between the two different materials. For instance, the Pd4 peptide is known to lay flat on the particle surface in an extended conformation,³⁵ which may lead to enhanced exposure of the catalytic species as compared to the citrate-capped materials that can tightly pack on the metal surface to prevent metallic exposure. As such, these control studies confirm the increased reactivity from the biomimetic materials and that similar reaction trends are noted for comparable material sets based upon the reaction conditions, further supporting the hypothesis that equilibria shifting plays an important role in the transmetalation step of nanoparticle-driven Suzuki coupling.

Once the fundamental catalytic effects of the Pd4-capped Pd materials were determined, the reactivity of the structures with a variety of different aryl halide substrates was examined. For this, a 0.50 M K_3PO_4 reaction medium was employed as it provided the highest reactivity. As presented above, when 4-iodobenzoic acid was employed as the aryl halide substrate with a catalyst loading of 0.05 mol% Pd, a product yield of $96.5 \pm 7.1\%$ was observed over a 24.0 h reaction time frame at room temperature (Table 2); however, when 4-bromobenzoic acid and 4-chlorobenzoic acid were employed as the substrate,

diminished product yields were determined (Table 2). For these reactions at room temperature, no coupling was observed from the bromo- and chloro-based substrate, but when the reaction temperature and catalyst concentration were increased, product

Entry	Substrate	Intermediate	Yield
1		None	 96.5 ± 7.1% ^a
2		None	 0 ± 0% ^a 0 ± 0% ^b 10.1 ± 2.8% ^c
3		None	 0 ± 0% ^a 0 ± 0% ^b 8.7 ± 3.3% ^c
4		None	 65.2 ± 7.4% ^a
5		None	 0 ± 0% ^a 2.6 ± 3.1% ^b 54.1 ± 17.1% ^c
6		None	 0 ± 0% ^a 0 ± 0% ^b 6.2 ± 2.4% ^c
7		 Not Soluble ^a 0% ^d	 Not Soluble ^a 40.5 ± 7.3% ^d
8		 38.1 ± 3.0% ^a 27.9 ± 5.0% ^d	 8.4 ± 3.2% ^a 24.8 ± 4.0% ^d

^a0.5 M K₃PO₄, 0.05 mol% Pd, RT, 24 h
^b0.5 M K₃PO₄, 0.10 mol% Pd, 40.0 °C, 24 h
^c0.5 M K₃PO₄, 0.10 mol% Pd, 60.0 °C, 24 h
^d0.5 M K₃PO₄, 0.05 mol% Pd, 40.0 °C, 24 h

Table 2. Suzuki coupling reactions catalyzed by the Pd₄-capped Pd nanoparticles

generation was evident. To this end, with a Pd loading of 0.10 mol% and a reaction temperature of 60.0 °C, product yields of $10.1 \pm 2.8\%$ and $8.7 \pm 3.3\%$ were observed for 4-bromobenzoic acid and 4-chlorobenzoic acid with $\text{PhB}(\text{OH})_2$, respectively.

Transitioning to phenol substrates, similar reaction trends were noted. For instance, when using 4-iodophenol, a product yield of $65.2 \pm 7.4\%$ was observed at room temperature using 0.05 mol% Pd. No reactivity was again noted for 4-bromophenol under these conditions; however, when using a Pd loading of 0.10 mol%, a product yield of $2.6 \pm 3.1\%$ was noted for 4-bromophenol at 40.0 °C that increased to $54.1 \pm 17.1\%$ at 60.0°C. For 4-chlorophenol at 60.0°C, a product yield of $6.2 \pm 2.4\%$ was quantitated, indicating that catalytic turnover was possible. In general, for the different substrates, an overall reactivity trend of $\text{I} > \text{Br} > \text{Cl}$ was observed, which is likely due to the differences in the bond strength between C-I, C-Br, and C-Cl bonds.¹²⁹ In comparison to Stille coupling studies employing the same nanocatalysts and substrates, the product yields were diminished for Suzuki coupling; however, the reactivity trends based upon halogen identity remained the same.^{12, 17} Note that for all reactions of Table 2, formation of only the anticipated product was observed: no homocoupling or undesired byproducts were noted.

Disubstituted aryl halide substrates were also studied for the nanoparticle-catalyzed Suzuki reaction using 0.50 M K_3PO_4 . When employing 3,5-diiodobenzoic acid as the aryl halide with a Pd loading of 0.05 mol% at 40 °C, formation of the dicoupled product was observed at $40.5 \pm 7.3\%$. Note that this temperature was required to fully dissolve the substrate in the reaction medium. Such a result indicates that the coupling of the first phenyl ring is the rate-limiting step that activates the coupling at the second iodo-position for an enhanced rate, consistent with Stille coupling studies.¹⁷ When 3-bromo-5-iodobenzoic acid

was employed as the substrate at room temperature, a reaction yield of $38.1 \pm 3.0\%$ of the monocoupled product (3-phenyl-5-bromobenzoic acid) and $8.4 \pm 3.2\%$ of the dicoupled product (3,5-diphenylbenzoic acid) were observed after 24.0 h at room temperature. When the temperature was increased to $40.0\text{ }^{\circ}\text{C}$ for the 24.0 h reaction period, an increase in the dicoupled product to $24.8 \pm 4.0\%$ was noted, concomitant with a decrease in the monocoupled product yield to $27.9 \pm 5.0\%$, all of which was likely due to the increased temperature driving the reaction forward. Such studies suggest a degree of selectivity for iodo-based substrates over bromo-base reagents may be present, which is similar to the results observed for Stille coupling.¹⁷

3.5 Summary and Conclusions

These results demonstrate that the Pd₄-capped Pd nanoparticles are catalytically reactive for Suzuki coupling over a variety of aryl halide substrates in water at low reaction temperatures. While the reactivity is not the fastest, unique mechanistic information for nanoparticle-driven systems in water is presented. Such information could be important in transitioning these reactions toward more sustainable conditions; however, changes to the reaction system such as depositing the materials onto a heterogeneous support may significantly alter the reactivity and would need to be fully analyzed before application. Furthermore, the results indicate that the solution medium is highly important to the overall functionality. To this end, the base plays a key role in controlling the reaction, as observed by the variations in product yields and TOF values using the differently charged bases. It is likely that the strength of the base is responsible for the observed reactivity trend. In this regard, during the transmetalation step, both a four-coordinate, negatively charged

boronate species and a $L_2Pd(Ar)(OH)$ intermediate are formed based upon the reactivity of the hydroxide species in solution. With stronger bases, competing pathways that require significant equilibrium shifting inhibit Suzuki coupling, while weaker bases, K_3PO_4 and Na_2CO_3 , present a different reaction mixture that is more optimal for Suzuki coupling. These results are important as they demonstrate the effects of solution conditions on the overall reaction that are generally not considered for nanoparticle catalyzed reactions, but may be integral in advancing such systems toward green conditions. Upon comparing the Suzuki results with previous Stille coupling studies using the same catalytic materials, it is suggested that the transmetalation process may be rate-limiting, where changes in this step could be employed to optimize and enhance the overall reaction efficiency.

“Reprinted (adapted) with permission from (Briggs, B. D.; Pekarek, R. Y.; Knecht, M. R. Examination of Transmetalation Pathways and Effects in Aqueous Suzuki Coupling Using Biomimetic Pd Nanocatalysts. *J. Phys. Chem. C*. **2014**, *118*, 18543-18553). Copyright (2014) American Chemical Society.”

Chapter 4. Reductant and Sequence Effects on the Morphology and Catalytic Activity of Peptide-capped Au Nanoparticles

4.1 Overview of Study

The use of peptides as capping ligands for materials synthesis has been widely explored. The ambient conditions of bio-inspired syntheses using molecules such as peptides represent an attractive route for controlling the morphology and activity of nanomaterials. Although various reductants can be used in such syntheses, no comprehensive comparison of the same bio-based ligand with different reductants has been reported. In this contribution, peptides AuBP1, AuBP2 and Pd4 are used in the synthesis of Au nanoparticles. The reductant strength is varied by using three different reducing agents: NaBH₄, hydrazine, and ascorbic acid. These changes in reductant produce significant morphological differences in the final particles. The weakest reductant, ascorbic acid, yields large, globular nanoparticles with rough surfaces, while the strongest reductant, NaBH₄, yields small, spherical and smooth nanomaterials. Studies of 4-nitrophenol reduction using the Au nanoparticles as catalysts reveal a decrease in activation energy for the large, globular, rough materials relative to the small, spherical, smooth materials. These studies demonstrate that modifying the reductant is a simple way to control the activity of peptide-capped nanoparticles.

4.2 Motivation

Bio-inspired strategies for producing inorganic nanoparticles are of great interest because they can control the structure of the material under very mild synthetic conditions.^{5, 130}

Biomolecule-capped nanomaterials have proven useful in many applications, including catalysis, biosensing, and nanoparticle assembly, where the biotic interface can play an integral role in their performance. Many biological entities have been used to passivate nanoparticle surfaces, including DNA,¹³¹⁻¹³⁴ viruses,⁴⁷ and peptides.^{2, 16, 18, 33, 55, 135-136} Peptides are particularly promising, because they can provide biomolecular recognition for specific binding to metal interfaces and they are relatively easy to prepare. Biocombinatorial selection methods such as phage and cell-surface display have been used to isolate many peptides with affinity for metal,^{27, 33} metal oxide,⁵⁴⁻⁵⁵ and metal sulfide surfaces,¹³⁷⁻¹³⁸ with selectivity for specific target materials.¹³⁹⁻¹⁴⁰

While nanoparticles of many compositions have been prepared using peptides, Au nanoparticles are of particular interest due to their applications in sensing,¹⁴¹ catalysis,^{40, 142-143} diagnostics,¹⁴⁴ and bionanocombinatorics.^{139-140, 145} A key property of Au nanoparticles is their Localized Surface Plasmon Resonance (LSPR), which produces strong scattering and absorption of light over a wavelength range that can be tuned by varying the nanoparticle size and shape.¹⁴⁶ Peptides can provide control over morphology and activity of Au nanoparticles through their sequence specific interactions with the Au surface.⁴⁰ The AuBP1 (WAGAKRLVLRRE) and AuBP2 (WALRRSIRRQSY) sequences are exemplar peptides with affinity for Au and the ability to generate nearly monodisperse nanoparticles.^{40, 135} Sarikaya and colleagues isolated these peptides via phage display and demonstrated that the biomolecular structure (linear vs. cyclic) played a critical role in controlling the overall affinity of the sequence for the metal surface.¹³⁵ More recently, Tang *et al.* demonstrated the importance of the nature of binding to the metal surface, which can be predominantly enthalpic or entropic.¹³⁹ Both AuBP1 and AuBP2 were classified as

enthalpic binders, meaning that they incorporate several residues throughout the sequence that anchor the biomolecule to the metallic surface in a small number of possible configurations.¹³⁹ Specifically, AuBP1 and AuBP2 each have four anchor residues dispersed throughout the sequence (Trp-1, Arg-6, Arg-10, and Arg-11 in AuBP1, Trp-1, Arg-4, Arg-5, and Tyr-12 in AuBP2).¹³⁹ Conversely, a peptide exhibiting entropically driven binding has fewer anchor residues, but assumes many different surface bound conformations, which imbue it with relatively high entropy in the bound state. The Pd4 peptide (TSNAVHPTLRHL), originally isolated with affinity for palladium (Pd), is an exemplar of entropic binding peptides on Au.⁹ It includes only two anchor residues (His-6 and His-11); however, extensive simulation studies revealed a relatively large number of binding conformations for the peptide on an aqueous Au surface.¹³⁹ Peptide-capped Au nanoparticles prepared using NaBH₄ as the reductant with each of these peptides were spherical, and their size was correlated with the number of anchor residues (*i.e.* enthalpic contribution), rather than the overall binding affinity, which is related to the free energy change of binding.⁴⁰

Beyond the peptide-metal interactions, several other factors control the growth and final structure of peptide-capped Au nanoparticles.¹⁴⁷⁻¹⁴⁹ Nanoparticle formation is initiated by addition of a reductant that reduces dissolved Au³⁺ to insoluble Au⁰, initiating nanoparticle nucleation and growth. Previous studies have shown that altering the strength of the reductant changes the rate of reduction, producing changes in nanoparticle size.¹⁴⁹ Thus, different reductants produce nanoparticles with different LSPR spectra, catalytic activities, and other properties that depend upon the nanoparticle size and shape.¹⁴⁷⁻¹⁴⁹ A strong reductant drives a burst of nucleation due to the high concentration of Au⁰ produced by

rapid reduction. The high nucleation density produces smaller final nanoparticles as a fixed amount of Au precursor deposits onto a larger number of nuclei. A weaker reductant produces a lower concentration of Au⁰ through slower reduction. This results in a lower probability of overcoming the barrier to nucleation and therefore a lower nucleation density. Ultimately, this produces a smaller number of larger particles.¹⁵⁰ Most prior studies of these effects employed standard nanoparticle surface passivants, such as thiols on Au, and produced quasi-spherical nanoparticles regardless of the reductant employed.¹⁵¹ The effects of the peptide on nanoparticle generation with different reductants have not been systematically studied. The kinetics and thermodynamics of binding of biomolecules with the Au surface are significantly more complex than those of thiols and similar passivants. As discussed above, sequence-dependent interactions at the nanoparticle surface control the peptide binding and therefore the peptide's role in arresting particle growth.¹³ If understood, this can provide enhanced control over particle size, morphology, surface structure, and properties that remains difficult to achieve via traditional approaches.

One area of rapidly growing interest for Au nanoparticles is catalysis. The reduction of 4-nitrophenol is widely employed as a probe reaction for evaluating the catalytic activity of such materials.^{40-41, 77-79, 152-153} The substrate, 4-nitrophenol, is a known pollutant and toxin that can be easily reduced to 4-aminophenol, a major pharmaceutical precursor.⁷⁷ This reaction is relatively simple and can be easily monitored using UV-vis spectroscopy in aqueous conditions at ambient temperature.⁷⁷⁻⁷⁸ Importantly, the reduction of 4-nitrophenol is known to operate by a surface reaction mechanism in which adsorption of hydrogen and the substrate to the metal surface is required for catalytic turnover.⁷⁹ This is

advantageous for the peptide-capped nanoparticles in that it provides a direct measure of the accessibility of the metal surface that cannot be readily assessed by other methods.

In previous chapters we explored peptide-capped Pd nanoparticles for various C-C coupling reactions and the mechanisms of these processes. While active for a large number of catalytic applications, the correlation between the Pd nanoparticle surface and catalytic functionality remains difficult to ascertain. Such effects, as controlled by the biomolecule capping agent, are very important for all noble metal nanoparticles, thus they must be fully examined. Au nanoparticles, on the other hand, are well known for their LSPRs, which allows for easy detection of changes in size and morphology. In this chapter, we study the combined effects of reductant strength and peptide binding at the Au nanoparticle interface based upon the rate of nanoparticle nucleation and growth, and the catalytic properties of the final materials. Au nanoparticles were generated using three different peptides, AuBP1, AuBP2, and Pd4, which span a known range of binding affinity and balance between enthalpic and entropic binding character.¹³⁹ Each of these was used in combination with three different reductants: sodium borohydride (NaBH_4), hydrazine, and ascorbic acid. The product nanoparticles were fully characterized using UV-vis absorbance spectroscopy, Transmission Electron Microscopy (TEM), and Selected Area Electron Diffraction (SAED) analysis. Their catalytic activity for the reduction of 4-nitrophenol to 4-aminophenol was also quantified. The results and synthetic strategies provide a path toward realizing low temperature and facile mechanisms of tuning Au nanoparticle size, shape, and surface state for applications in biosensing, catalysis, and related fields.

4.3 Methods

4.3.1 Materials

HAuCl₄ was purchased from Acros Organics, while NaBH₄ and hydrazine monohydrate were acquired from Sigma-Aldrich. Trifluoroacetic acid (TFA), tri-isopropyl silane (TIS), and 4-nitrophenol were obtained from Alfa Aesar, and ascorbic acid, acetonitrile, methanol, and *N,N*-dimethylformamide were purchased from BDH Chemicals. Finally, all Fmoc-protected amino acids, Wang resins, and coupling reagents were acquired from Advanced Chemtech. Ultrapure water (18.2 MΩ·cm) was used for all experiments and all reagents were used as received.

4.3.2 Peptide Synthesis

Standard solid-phase peptide synthesis protocols were used with a TETRAS peptide synthesizer (Creosalus).⁹⁸ Peptides were cleaved from the Wang resins using a TIS/H₂O/TFA cleavage cocktail and purified using reverse-phase HPLC. The purified peptide sequences were confirmed using MALDI-TOF mass spectrometry.

4.3.3 Nanoparticle Synthesis

Au nanoparticles were prepared by minor modifications of previously described methods.⁴⁰ Modifications to the synthesis protocol using the different reductants (ascorbic acid and hydrazine in place of the NaBH₄ used previously) are discussed below. Briefly, 0.50 mL of a 1.0 mM peptide solution was diluted with 4.46 mL of H₂O in a glass vial. To this, 0.01 mL of 100 mM HAuCl₄ was added and the solution was mixed vigorously for 15 min.

Next, 0.03 mL of freshly prepared 100 mM NaBH₄ was added and the solution was mixed again. This provides a threefold molar excess of NaBH₄ compared to Au. The nanoparticles were allowed to reduce for 60 min prior to analysis or use. Identical synthetic protocols were employed using the other reductants, with a threefold molar excess of ascorbic acid to Au³⁺ or a twofold molar excess of hydrazine.

4.3.4 Characterization

TEM analysis was done using a JEOL JEM-2010 microscope operating at 200 kV. The samples were prepared by drop-casting 5 μL of the nanoparticle solution onto a carbon-coated 400 mesh Cu grid (EM Sciences), which was allowed to dry overnight. UV-vis monitoring of nanoparticle formation, as well as the reduction of 4-nitrophenol, was conducted using an Agilent 8453 spectrometer. Samples were analyzed using a quartz cuvette with a 1 cm optical pathlength.

4.3.5 4-Nitrophenol Reduction Reaction

The catalytic activity of the Au nanoparticles was evaluated using the reduction of 4-nitrophenol to 4-aminophenol following previously established protocols.^{22, 78} In a 1 cm quartz cuvette (nominal volume = 3.5 mL), 1.0 mL of the Au nanoparticle solution was combined with 1.0 mL of freshly-prepared 15 mM NaBH₄ in water. Next, 1.0 mL of a 150 μM 4-nitrophenol solution, prepared in water, was added to initiate the reaction. Monitoring of the change in the absorbance at 400 nm at 20.0 s intervals for 12.0 min was conducted in triplicate at 20 – 50 °C for all nine material sets (Au nanoparticles prepared using each of the three peptides, reduced using each of the three reductants).

4.4 Results and Discussion

4.4.1 Nanoparticle Synthesis and Characterization

Au nanoparticles were prepared using three peptides: AuBP1, AuBP2, and Pd4. These sequences were selected to span a known range of binding parameters for Au. AuBP1 and AuBP2, specifically identified for their affinity to bind Au surfaces,¹³⁵ have binding affinities (ΔG of binding) on Au of -37.6 ± 0.9 and -36.4 ± 0.3 kJ/mol, respectively.¹³⁹ Pd4 was originally isolated via phage display for the ability to bind Pd. It binds to Au with a ΔG value of -30.3 ± 0.2 ,¹³⁹ which is smaller than its binding affinity for Pd (-33.0 ± 0.5 kJ/mol).^{9, 19, 139} In addition, these three peptides have differing thermodynamic driving forces for binding to the Au surface. In this regard, both the AuBP1 and AuBP2 have several anchor residues interspersed throughout the sequence, thus they have been classified as enthalpic binding peptides. Conversely, the Pd4 only has two anchors at the histidines; however, it can adopt many different conformations on the Au surface, and is thus classified as an entropic binder. Taken together, these three peptides provide different binding parameters (both in overall affinity and thermodynamic driving forces), spanning a significant range of possible interactions.

For nanoparticle synthesis experiments, each peptide was mixed with Au^{3+} in water at a Au:peptide ratio of 2:1 for 15 min prior to reduction. This allows for complexation of the metal ions to the biomolecule. After complexation, each solution was reduced separately with one of three reductants: NaBH_4 , hydrazine, or ascorbic acid. These were selected to span a range of strengths as reducing agent. NaBH_4 is the strongest reductant in this set,

followed by hydrazine, with ascorbic acid being the weakest reductant.¹⁵⁴⁻¹⁵⁵ For both NaBH_4 and ascorbic acid, a threefold molar excess relative to Au^{3+} was employed; however, a twofold molar excess of hydrazine was used. The lower ratio of hydrazine to Au was specifically chosen as this was the ratio used in previous studies.¹⁵⁶ In all cases, an obvious color change was noted upon reduction, as described below, and the product nanoparticle dispersions remained stable for > 24 h without any visible precipitation.

Initial characterization of the nanoparticle formation process as a function of both the peptide and reductant was completed using UV-vis spectroscopy (Figure 4.1). For each system, the spectra were background corrected using the peptide solution at the reaction concentration, thus the observed absorbance arises only from the Au^{3+} /peptide complex and/or the nanoparticles. As shown in Figure 4.1a, for the AuBP1-system prior to reduction, a minor peak at 500 nm was visible, while a shoulder absorbance is visible at

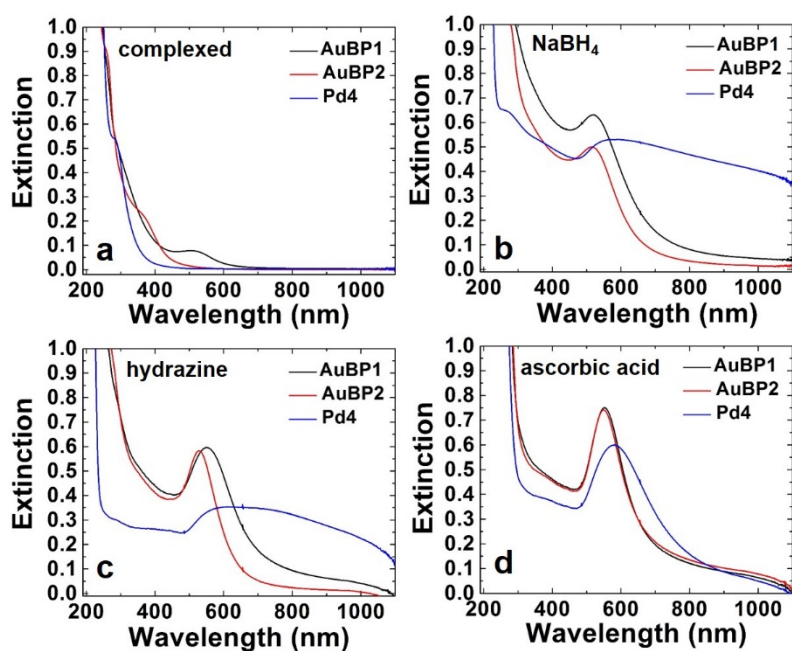


Figure 4.1. UV-vis analysis of Au nanoparticle formation. Part (a) presents the spectra of each Au^{3+} /peptide complex prior to reduction, while parts (b-d) shows the materials after reduction with (b) NaBH_4 , (c) hydrazine, and (d) ascorbic acid.

~400 nm for the AuBP2-mediated reaction. For the Pd4-based system, no significant peaks were visible in the spectrum. Upon reduction, an absorbance peak associated with the Au nanoparticle LSPR was evident, with a peak position and shape that varied with both the peptide and reductant. For NaBH₄ specifically (Figure 4.1b), when AuBP1 and AuBP2 were used to cap the Au nanoparticles, a distinct and relatively sharp LSPR was observed at 520 nm; however, when Pd4 was used to generate the Au nanoparticles, a broader and red-shifted LSPR absorbance was observed. This suggests that the Pd4-capped Au nanoparticles are larger, more polydisperse, and/or more aggregated in solution than the AuBP1- and AuBP2-capped materials. With hydrazine as the reductant (Figure 4.1c), the AuBP1- and AuBP2-capped materials again have a distinct LSPR absorbance after reduction. In this system, the peak position is slightly red shifted, compared to the nanoparticles produced with NaBH₄, to 550 nm for the AuBP1-capped materials and 530 nm for the AuBP2-capped structures. Interestingly, for the hydrazine reductant, the AuBP1-capped nanoparticles resulted in a broader LSPR absorbance as compared to the AuBP2 materials. For the Au nanoparticles capped with Pd4 and reduced with hydrazine, a broad absorbance with a peak beginning at 580 nm was again observed. Finally, when ascorbic acid was used as the reductant (Figure 4.1d), the results were substantially different. The spectra for the AuBP1- and AuBP2-capped materials were nearly identical with a distinct plasmon band 550 nm. This was the sharpest LSPR observed among all of the samples. For the Pd4-capped materials reduced with ascorbic acid, a distinct LSPR peak at 580 nm was noted that was significantly sharper than that observed for the Pd4-capped nanoparticles prepared using the stronger reducing agents.

TEM imaging and analysis to extract nanoparticle size information of all materials was carried out to directly observe the nanoparticle morphology changes with variations in reductant and capping peptide (Figure 4.2). For the sizing analysis, >100 nanoparticles

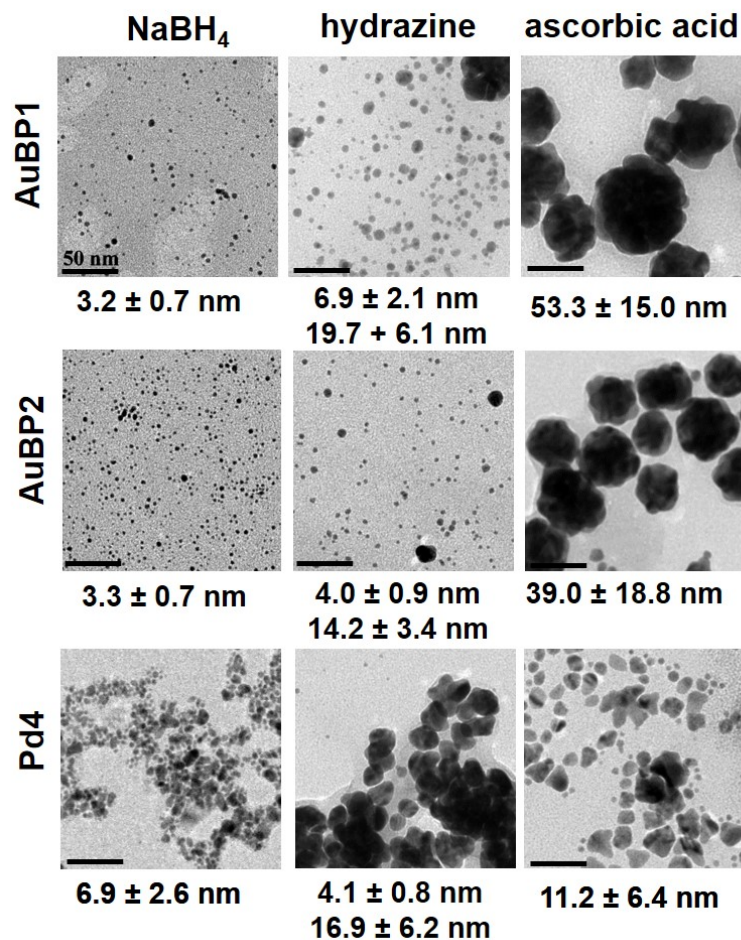


Figure 4.2. TEM images of the Au nanoparticles prepared as a function of peptide passivant and reductant. All scale bars are 50 nm.

were counted from at least three separate TEM images to generate particle size histograms (Chapter 6.4, Figure 6.7). SAED analysis of all of the prepared Au nanoparticles was conducted (Chapter 6.4, Figure 6.8), and in all cases only diffraction rings corresponding

to Au were visible. Particles produced using NaBH_4 as the reducing agent gave SAED patterns with more diffuse rings, consistent with smaller particle size, while those produced using ascorbic acid gave the sharpest rings, with discrete spots associated with individual crystallites. Using the AuBP1 and AuBP2 peptides as the capping agents with NaBH_4 as the reductant yielded small, quasi-spherical Au nanoparticles with average diameters (\pm one standard deviation) of 3.2 ± 0.7 nm and 3.3 ± 0.7 nm, respectively. Using the Pd4 peptide to stabilize the particles under the same conditions, more polydisperse nanoparticles with an average diameter of 6.9 ± 2.6 nm were obtained. These results are consistent with the UV-vis spectra of the materials, in which the AuBP1 and AuBP2 systems displayed sharp LSPR bands, while a broader, red-shifted LSPR peak was observed for the Pd4-based structures. However, the very broad LSPR peak from the materials prepared using the Pd4 cannot be accounted for based on the increased size and polydispersity alone. This suggests that the Pd4-capped particles are significantly aggregated in solution, even though they do not aggregate to an extent that they visibly precipitate. With hydrazine as the reductant in combination with all three peptides, a bimodal nanoparticle size distribution was observed. Specifically, for AuBP1, spherical particles were again noted, but with a larger average diameter of 6.9 ± 2.1 nm (88% of the sample, by number). These were accompanied by larger agglomerates with a diameter of 19.7 ± 6.1 nm (12% of the sample, by number). For the AuBP2-capped nanoparticles reduced with hydrazine, the results were similar with the smaller nanoparticles (4.0 ± 0.9 nm) comprising 91% of the population and the larger agglomerates (14.2 ± 3.4 nm) accounting for 9% of the sample. Finally, for the materials fabricated using the Pd4 peptide with hydrazine, the bimodal trend was continued with small nanoparticles of 4.1 ± 0.8 nm

diameter comprising 71% of the sample and larger nanoparticles of 16.9 ± 6.2 nm diameter comprising 29%. Interestingly, the Pd4-capped system yielded a greater percentage of larger nanoparticles as well as a greater occurrence of aggregation, as noted via TEM imaging. These results are again consistent with the UV-vis spectra of the materials. In this regard, the AuBP1- and AuBP2-capped materials reduced with hydrazine displayed red shifted and broadened LSPRs as compared to the comparable structures reduced with NaBH_4 . This is a direct consequence of the increase in particle size and inclusion of significantly larger particles. Furthermore, the AuBP1-capped particles were generally larger and more polydisperse in size, giving rise the broadened and red shifted LSPR relative to the AuBP2-based materials. Finally, the Pd4-capped structures again appeared to be aggregated and non-spherical in shape, generating the very broad LSPR absorbance.

TEM imaging of Au nanoparticles prepared using ascorbic acid showed dramatic differences in particle size and morphology compared to nanoparticles prepared using the stronger reductants. The AuBP1-capped nanoparticles produced using ascorbic acid had an average diameter of 53.3 ± 15.0 nm. More interestingly, the surface structure of these materials was quite rough. Similar nanomaterials were prepared using AuBP2 and ascorbic acid, but the average diameter of these globular nanoparticles was 39.0 ± 18.8 nm. Interestingly, when Pd4 was used with ascorbic acid, smaller irregularly shaped nanostructures were generated. Their size, as measured along their longest axis, was 11.2 ± 6.4 nm.

For all of the particles produced using AuBP1 and AuBP2, the measured absorbance spectra are consistent with computed spectra based upon the size distributions measured by TEM. Extinction spectra (Chapter 6.4, Figure 6.9) were computed via Mie theory

assuming spherical particles with a Gaussian size distribution and the mean diameter and standard deviation of diameter obtained from TEM imaging. For the particles reduced with hydrazine, where a bimodal size distribution was observed, only the large particle mode was considered. Because of the strong size-dependence of absorbance and scattering in this size range, the larger subpopulation of particles will dominate the extinction spectrum. The relatively weak LSPR predicted and observed for the NaBH_4 -reduced particles is associated with their small size and resulting increased damping of the LSPR by interface scattering of electrons. The largest particles, produced using ascorbic acid as the reductant, have the sharpest LSPR peak, which is slightly red-shifted from the peak computed and observed for the hydrazine-reduced particles, due to their larger size. The LSPR spectra observed for the Pd4-capped particles cannot be explained based on the size-distribution of the primary particles, leading us to conclude that they are somewhat aggregated in solution, with a broad range of aggregate sizes, during the absorbance measurement.

The above results illustrate that changes in the peptide and in the reducing agent used in the synthesis can have dramatic and non-obvious effects on the size, shape, and optical properties of the product Au nanoparticles. The binding at the metal nanoparticle interface in solution, as controlled via the peptide sequence, as well as the strength of the reductant each play a significant role in controlling the particle size and morphology. Clearly these effects do not operate independently, but synergistically. We do not observe universal trends with respect to either the peptide or reductant. For example, for AuBP1 and AuBP2, it can be seen that using a stronger reductant produces smaller nanoparticles, which can be understood based upon the stronger reductant generating a larger number of nuclei via faster reduction of Au^{3+} to Au^0 . However, this trend does not hold for the Pd4-capped

particles. Similarly, one might expect Pd4 to produce larger particles than AuBP1 and AuBP2, because it has both lower enthalpy and free energy of binding, *i.e.* it is both a relatively weak binder and an entropically-driven binder on Au, but this only proves to be the case for the strongest reducing agent, NaBH₄. For weaker reducing agents, the situation is more complex, with the interplay between the biomolecular binding and the reduction kinetics working together to control the final nanoparticle structure.

Based upon the UV-vis and TEM results, both the peptide sequence and the reductant play critical roles in controlling the size and morphology of the Au NPs. With respect to the reductant, the rate of the reduction of Au³⁺ to Au⁰ is likely to play a central role, as it directly affects the particle nucleation and growth rate. The rate of reduction and of particle formation can be monitored by observing the appearance of the LSPR band for Au nanoparticles. Assuming pseudo-first order kinetics allows us to extract a rate constant representative of the reduction and particle nucleation and growth process. To this end, the LSPR absorbance was monitored using UV-vis by taking one spectrum per second for the first 5.0 min after addition of the reductant. From this, the rate constant (k) for nanoparticle growth can be determined, as presented in Figure 4.3 for the reactions employing hydrazine and ascorbic acid. Unfortunately, the rate of particle growth using NaBH₄ was too rapid to quantify with this approach. Using hydrazine as a reductant, the fastest formation of Au nanoparticles occurred in the presence of the Pd4 peptide ($0.0816 \pm 0.0120 \text{ s}^{-1}$). For the AuBP1 and AuBP2 peptides, which have both greater affinity for Au and more enthalpic binding character, smaller k values were observed: 0.0077 ± 0.0009 and $0.0156 \pm 0.0012 \text{ s}^{-1}$, respectively. The same trend was noted for the weaker ascorbic acid reductant. Faster nanoparticle growth was evident using Pd4 (k value = $0.0457 \pm 0.0100 \text{ s}^{-1}$), while slower

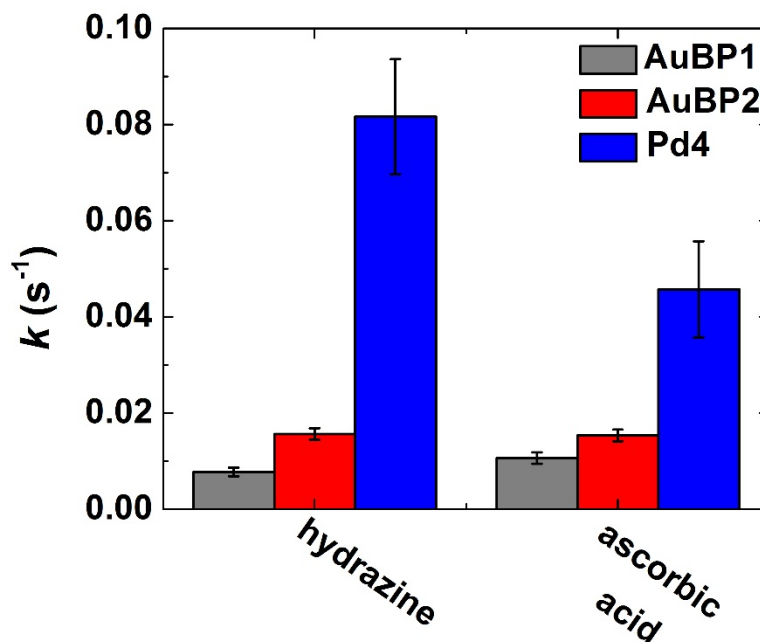


Figure 4.3. Comparison of the rate of Au NP formation as measured via the growth of the plasmon band. Values could not be determined for the particles reduced using $NaBH_4$ due to their rapid rate of formation.

nanoparticle growth occurred in the presence of AuBP1 ($0.0153 \pm 0.0012 s^{-1}$) and AuBP2 ($0.0106 \pm 0.0012 s^{-1}$) materials. Here, the binding affinity of different peptides for the Au surface varies as $AuBP1 > AuBP2 \gg Pd4$,¹³⁹ which correlates directly with the trend in observed particle growth rate.

Taken together, the UV-vis and TEM results provide insight into the effects of both the peptide capping agent and reductant upon the final particle morphology. The final morphology depends strongly upon the rate of reduction, which affects particle nucleation and growth rates. The strongest reductant, $NaBH_4$, drives extremely rapid nanoparticle nucleation. This high nucleation density gives rise to the smallest particles observed by TEM. This is consistent with the sharp plasmon bands at the shortest wavelengths (520 nm) observed for the nanoparticles produced using $NaBH_4$ with the AuBP1 and AuBP2

peptides. Use of the Pd4 peptide with NaBH_4 produced more polydisperse nanoparticles with a broad absorbance spectrum. This can be rationalized based on a high nucleation density coupled with incomplete surface capping that allows the initial nanoparticles to aggregate. With hydrazine, a weaker reducing agent than NaBH_4 , slower nanoparticle nucleation and growth was observed. The lower nucleation density produced by slower reduction ultimately generates larger primary particles. The influence of the affinity of the peptide for the metal surface was more significant in this case. The nanoparticles prepared using hydrazine with any of the peptides were slightly larger than those fabricated using NaBH_4 , leading to slightly red shifted SPR bands in the UV-vis analysis. Note that the reduction with hydrazine in the presence of Pd4 is substantially faster than in the presence of AuBP1 or AuBP2 (Figure 4.3). Most interestingly, when the weakest reductant, ascorbic acid, was used, the nanoparticle morphology changed substantially. When ascorbic acid was used with AuBP1 or AuBP2, larger nanoparticles with rough surfaces were obtained. These structures presented LSPR bands furthest shifted to the red due to their large size. This can be rationalized based on a combination of slow reduction, limited aggregation of primary particles, and slow overgrowth on these aggregates as Au reduction continues. In contrast, when ascorbic acid is used with Pd4, the reduction is faster and more polydisperse, irregular nanoparticles result. Calculation of the anticipated UV-vis spectra for these materials correlated directly to the observed spectroscopic results based upon the size and morphology of the nanoparticles.

The rate of nanoparticle nucleation and growth, as measured by the growth of the LSPR absorbance, is directly correlated with the binding affinity of the peptide to the Au surface. For the strongest reductant (NaBH_4), the growth rates were too fast to monitor, and the

effect of the peptide was limited. For the weaker reductants, the peptides may weakly interact with the growing nanoparticle surface in solution throughout the entire process. They can slow growth by complexing with the Au^{3+} ions, reducing the rate of Au^{3+} to Au^0 reduction, and also by adsorbing to the nanoparticle surface, slowing deposition of Au^0 . The latter mechanism would be affected significantly by the affinity of the peptide for the metal surface, as well as the morphology of the nanoparticle interface, as those with the strongest affinity or highest number of anchor residues would more effectively inhibit metal atom deposition compared to peptides that are less strongly bound or whose binding is more entropically driven. This is consistent with the observed rates of particle growth, which for a given reductant were much slower for the relatively strong enthalpically driven binders, AuBP1 and AuBP2, compared to the weaker, entropically-driven binder, Pd4. The final particle size, however, is determined by both the growth rate and the nucleation density, and therefore slower growth does not necessarily correlate with smaller final particles.

As a control study, TEM imaging of the AuBP1- and AuBP2-complexes with Au^{3+} ions prior to reduction were acquired. Such studies were completed as minor absorbances were noted in the spectra of these materials, suggesting some reduction to Au^0 may have occurred. In this analysis, the formation of large, branched Au materials were observed with diameters > 300 nm (Chapter 6.4, Figure 6.10). SAED analysis confirmed that the materials were polycrystalline Au. Additional studies are required to fully understand this unique phenomena.

Based upon the binding mechanism of these peptides on Au,¹³⁹ the biomolecules are expected to non-covalently interact with the metallic surface via multiple points of contact,

generating a biotic/abiotic interface that maintains the colloidal stability of the nanoparticles. From previous measurements,^{135, 139} the affinity of the biomolecules (*i.e.* their overall Gibbs free energy, ΔG , of binding) on Au is similar to that of standard monodentate thiols.¹³⁵ However, thiol ligands are covalently attached to the metal interface at a single point, forming a comparatively rigid inorganic/organic interface. Ligands stabilize nanoparticle colloids either through steric or electrostatic effects, or a combination of both,¹⁵⁷ depending upon the combination of ligand and solvent. Because the conformational flexibility of the bound peptides is significantly larger than that of the rigidly bound thiols, entropic effects play a more significant role in their interaction with the surface. Furthermore, these dense biological interfaces are highly charged, with both steric and electrostatic contributions to nanoparticle stabilization. Despite the differences in the nature of binding, based upon the similar overall binding affinities and stabilization mechanisms for the two different ligand classes, comparable degrees of Au nanoparticle stability in colloidal suspensions are anticipated and observed.

4.4.2 Reduction of 4-Nitrophenol

Once the Au nanomaterials were characterized for their morphological and optical properties, they were used as catalysts for the reduction of 4-nitrophenol. Since this reaction occurs directly on the metallic surface,⁷⁸ it provides insight into the structure and accessibility of the metal surface in solution. Additionally, the reaction is relatively quick and easily monitored using UV-vis absorbance changes from which apparent rate constants can be determined.⁷⁸ To probe their reactivity, each peptide-capped Au nanoparticle was employed in the reaction in water at temperatures ranging from 20 to 50 °C. To start the

analysis, the nanoparticles were first mixed with an excess of fresh NaBH_4 for 3.5 min, after which the 4-nitrophenol substrate was added to initiate the reaction. NaBH_4 is added to the reaction as a source of hydrogen atoms to saturate the metal surface and drive the reduction process.⁷⁷⁻⁷⁹ Figure 4.4 presents the reaction analysis for the Au nanoparticles capped with AuBP2, which were reduced with NaBH_4 . From the UV-vis analysis of Figure 4.4a, the successful reduction of 4-nitrophenol was visible by a decrease in absorbance at 400 nm along with the generation and growth of a new peak at 320 nm, corresponding to 4-aminophenol, the end product. In general, the reaction occurred rapidly with a decrease

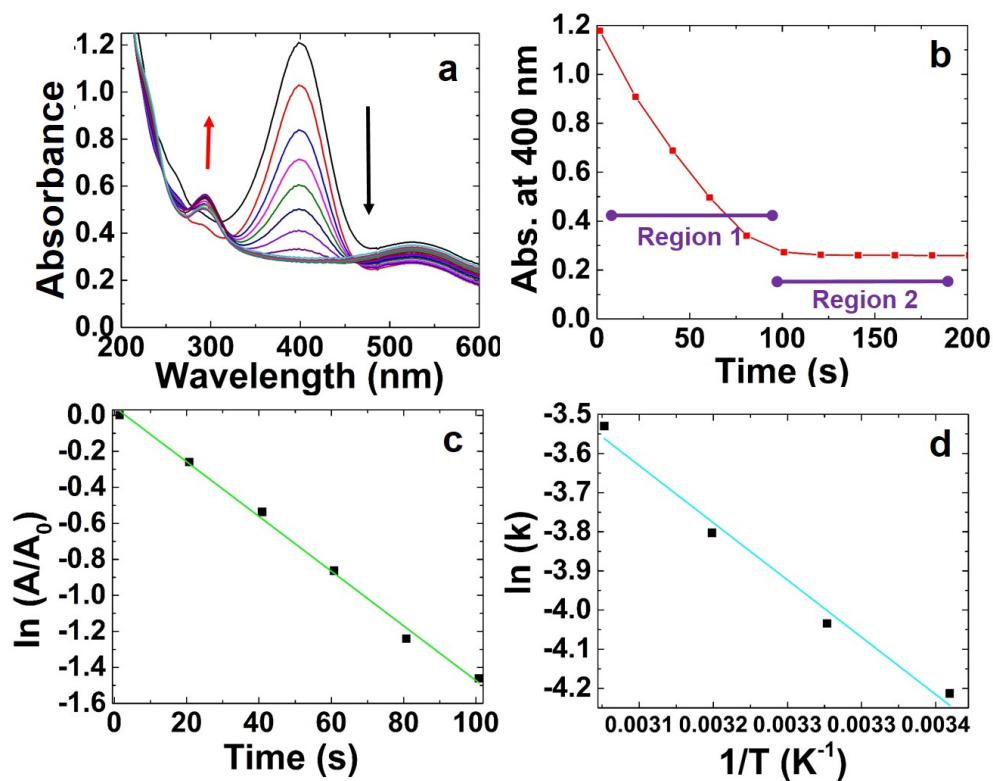


Figure 4.4. Determination of activation energies (E_a) for the 4-nitrophenol reduction reaction catalyzed by the peptide-capped Au nanoparticles. For this example, the AuBP2-capped nanoparticles reduced with NaBH_4 are used as the catalyst at 20 °C. Part (a) shows the UV-vis spectra where the peak at 400 nm corresponding to 4-nitrophenol decreases over time. Part (b) displays the absorbance intensity at 400 nm as a function of time. Part (c) presents the plot used to determine the pseudo-first order rate constant, while part (d) shows an Arrhenius plot from which the activation energy is determined.

in the absorbance at 400 nm (Figure 4.4b – Region 1), followed by a steady baseline upon completion (Region 2) at time >100 s. Note that the peptides (AuBP1, AuBP2, and Pd4) alone did not exhibit any catalytic activity for the reduction of 4-nitrophenol during at the time scales studied here (Chapter 6.4, Figure 6.11), demonstrating that the reactivity is catalyzed by the Au nanoparticle.

Because NaBH_4 was present in significant excess (100 fold), the reaction rate can be analyzed using pseudo-first order kinetics.^{22, 78} Figure 4.4c presents this analysis where absorbance (A) can be substituted in for concentration, as previously shown.^{22, 78} In this plot, the slope correlates to the apparent rate constant, k .⁷⁸ To determine the activation energy (E_a) for each nanoparticle catalyst, an Arrhenius plot was generated from the rate constants at the selected reaction temperatures (Figure 4.4d). Such an analysis was conducted for all nine nanoparticle samples, prepared using the three different peptides in combination with the three different reductants. Figure 4.5 presents an overall comparison of the rate constants as a function of reaction temperature, in which Figure 4.5a specifically presents the analysis for the particles capped with the AuBP1 sequence. For nanoparticles produced using NaBH_4 , the pseudo first-order rate constant increased from 0.0075 ± 0.0006 at 20 °C to 0.0132 ± 0.0001 at 40 °C. However, at 50 °C, the rate constant actually decreased. This non-Arrhenius behavior was observed for all of the particles prepared using the AuBP1 peptide, regardless of the reductant used for nanoparticle synthesis. This suggests that the materials capped using this peptide are inherently unstable at elevated temperatures. As a result, their catalytic activity is also altered, leading to the observed non-Arrhenius temperature dependence. Such effects are consistent with previous studies of Au nanoparticles capped with the AuBP1.⁴⁰

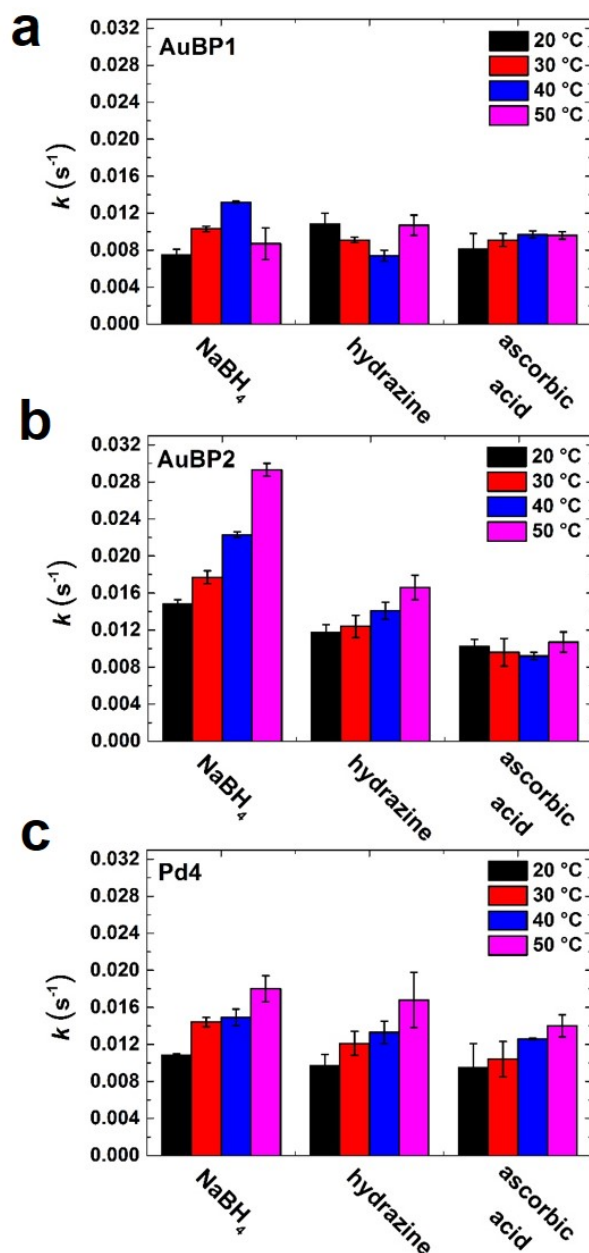


Figure 4.5. Comparison of the pseudo-first order rate constants for the 4-nitrophenol reduction reaction for each of the peptide-capped Au nanoparticle catalysts prepared using the indicated reductants. (a) AuBP1-capped nanoparticles; (b) AuBP2-capped nanoparticles, and (c) Pd4-capped nanoparticles.

When the particles capped with the AuBP2 peptide were employed as catalysts, a monotonic increase in the rate constant with temperature was observed for particles reduced using NaBH₄ and hydrazine. For the NaBH₄ particles capped with AuBP2, the rate

constants ranged from 0.0148 ± 0.0005 to $0.0293 \pm 0.0007 \text{ s}^{-1}$ from 20 – 50 °C, while for the AuBP2-stabilized particles reduced with hydrazine, the rate constants varied from 0.0124 ± 0.0012 to $0.0166 \pm 0.0013 \text{ s}^{-1}$ over the same temperature range. Interestingly, for the AuBP2-capped Au nanoparticles generated using ascorbic acid, no significant change in the rate constant as a function of temperature was evident. For the Pd4-capped nanoparticles, monotonic increases in rate constant with temperature were observed regardless of the reductant used to generate the nanoparticles. Table 3 lists all of the E_a values that were calculated for each of the nanoparticle systems, which ranged from 15.6 ± 2.3 for the Pd4-capped particles prepared using ascorbic acid to $26.2 \pm 0.9 \text{ kJ/mol}$ for the AuBP2-stabilized materials reduced using NaBH_4 .

Differences in the catalytic activity observed between the different Au nanoparticles can be attributed to two factors: nanoparticle stability at elevated temperatures and the structure/morphology of the interface of the peptide-capped nanoparticles. For the AuBP1-capped materials, regardless of the reductant used, and the AuBP2-capped materials reduced with ascorbic acid, the rate constants showed non-Arrhenius behavior, suggesting

Reductant	Peptide Name	Particle Size (nm)	E_a (kJ mol ⁻¹)
NaBH_4	AuBP1	3.2 ± 0.7	---
	AuBP2	3.3 ± 0.7	26.2 ± 0.9
	Pd4	6.9 ± 2.6	18.1 ± 2.3
hydrazine	AuBP1	6.9 ± 2.1 19.7 ± 6.1	---
	AuBP2	4.0 ± 0.9 14.2 ± 3.4	15.4 ± 4.9
	Pd4	4.1 ± 0.8	18.6 ± 2.4
ascorbic acid	AuBP1	53.3 ± 15.0	---
	AuBP2	39.0 ± 18.8	---
	Pd4	11.2 ± 6.4	15.6 ± 2.3

Table 3. Comparison of the activation energies for each NP catalyst

that the materials are not stable during the reaction. This is consistent with previous studies of the AuBP1-capped NPs, indicating that the peptides likely desorb from the particle surface and allow degradation or aggregation that produces a decrease in catalytic activity.⁴⁰ To confirm this instability, the Au nanoparticle spectrum before the catalytic reaction was started was compared with the spectrum at $t = 12$ min (red), which was achieved when the reduction of 4-nitrophenol was complete (Chapter 6.4, Figure 6.12). As seen in these comparisons, a significant shifting and broadening of the LSPR band was observed for all materials for which non-Arrhenius behavior was noted. This broadening is indicative of aggregation of the Au nanoparticles, strongly suggesting that the nanoparticle structure changes as a function of the reaction. For those materials that demonstrated Arrhenius behavior, no change in the LSPR of the Au nanoparticles was noted, indicating no significant material structural changes due to the reaction. Unfortunately, due to the low Au nanoparticle concentration and high salt concentration of the reaction, TEM imaging of the materials post-reaction could not be completed. Conversely, when the AuBP2-peptide was used to cap the nanoparticles, those structures prepared with NaBH_4 and hydrazine were quite reactive, but the rough surfaced materials prepared using ascorbic acid were again unstable. Interestingly, the E_a values for the AuBP2-capped particles varied significantly: 26.2 ± 0.9 kJ/mol for the materials reduced with NaBH_4 and 15.4 ± 4.9 kJ/mol for the hydrazine materials. Because the Au surface is the catalytic material, such changes likely reflect alterations in the surface structure, either through modifications based upon the biological molecules at the interface or through changes in the crystal morphology. Unfortunately, peptide-surface densities cannot be calculated due to the limited quantities of materials that can be prepared. Nevertheless,

both effects are controlled via the peptide, which can alter crystal morphologies based upon its affinity for the metal surface. Finally, for the Pd₄-passivated nanoparticles, all of the materials were stable with rate constants that increased as a function of temperature. From this, three different activation energies were determined that were very similar in magnitude. This indicates that the catalytic surface structure of these materials is quite similar to allow easy access to the Au surface to drive the chemical process.

Recyclability studies of the nanoparticles as catalysts for the reduction of 4-nitrophenol at 20 °C were also conducted with all nine peptide-capped Au nanoparticle systems in which the calculated rate constants are shown in the Chapter 6.4, Figure 6.13. For this process, when the initial reaction period of 12 min was completed, fresh NaBH₄ and 4-nitrophenol were added to reestablish the initial reaction substrate concentration. In this manner, four reduction cycles were completed using the same materials. In general, the rate constants for all systems decreased slightly with consecutive cycles, as observed by slightly reduced k_{obs} values for cycles 2 and 3. Interestingly, an increase was noted in the rate constant for all nanoparticle systems in cycle 4. Previous studies have indicated that this increase could be due to the removal of the capping agent from the metal surface or the exposure of blocked catalytic structures after multiple reaction cycles.^{79, 158} Nevertheless, it is evident that the peptide-capped structures are highly reactive and maintain this reactivity after multiple catalytic cycles.

Direct comparison of the catalytic results for the bio-inspired materials of the present study to other Au nanoparticle systems for 4-nitrophenol reduction reaction can be completed to assess their reactivity. For example, Bhandari *et al.* studied the reaction using Au NPNs formed using the R5 peptide template (SSKKS₂SGSYSGSKGSKRRIL) under

similar conditions.⁴¹ In that report, their measured an E_a value was similar to that obtained here using the AuBP2-capped Au nanoparticles (~ 29.0 kJ/mol for the Au nanoparticle networks versus 26.2 ± 0.9 kJ/mol for the AuBP2-based nanoparticles). Further studies performed by Xia and coworkers examined the effects of changes in Au nanoparticle structure upon catalytic activity for 4-nitrophenol reduction.¹⁵³ They measured activation energies for this reaction catalyzed by Au nanocages, nanoboxes, and partially hollow nanoboxes, showing that the more open structures had higher catalytic activity, as reflected by activation energies of 28.04 ± 1.43 kJ/mol for the nanocages, 44.25 ± 2.62 kJ/mol for the nanoboxes, and 55.44 ± 3.15 kJ/mol for the partially hollow nanoboxes.¹⁵³ Interestingly, the E_a obtained using the nanocages is similar to the E_a measured here for AuBP2-capped nanoparticles produced using NaBH_4 , while the Pd4-capped nanoparticles demonstrated even lower activation energies. This suggests that although the surface area plays a pivotal role in reduction activity, the type of capping ligand, corresponding effects on stability, as well as the degree of Au surface exposure are also key.

4.5 Summary and Conclusions

In conclusion, the results presented above indicate that both the materials directing peptide and the reaction conditions work in concert to control the final morphology and surface state of peptide-capped nanoparticles. Each peptide binds to the growing nanoparticle in solution, and thereby influences the particle size. This influence varies as a function of the binding strength and the number of anchor residues in the sequence. Furthermore, the number of nuclei formed immediately after reductant introduction varies as a function of the reductant strength. From this, the size of the materials can be directly controlled, a goal

which generally remains challenging to achieve via bio-inspired approaches. An interesting rough surface morphology was observed using the weakest reductant, ascorbic acid, indicating that variations in the surface structure are possible. This was supported by changes in the catalytic efficiency of the materials that is strictly dependent upon the nanoparticle surface. Taken together, these results present new avenues to access altered particle morphologies, sizes, and surface structures in a room-temperature peptide-mediated process via control of the reaction conditions and selection of the biological capping agent. Such effects could be important for the design of new nanoparticle systems for applications ranging from catalysis to biosensing and optics.

“Reprinted (adapted) with permission from (Briggs, B.D.; Li, Y.; Swihart, M.T.; Knecht, M.R. Reductant and Sequence Effects on the Morphology and Catalytic Activity of Peptide-Capped Au Nanoparticles *ACS Appl. Mater. Interfaces* **2015**, *7*, 8843-8851). Copyright (2015) American Chemical Society.”

Chapter 5. Towards a Modular Multimaterial Nanoparticle Synthesis and Assembly Strategy via Bionanocombinatorics: Effects of Bifunctional Peptides for Au and Ag Materials

5.1 Overview of Study

Materials-binding peptides represent a unique avenue towards controlling the shape and size of nanoparticles under aqueous conditions. Employing a bionanocombinatorial approach, two such materials-binding peptides were linked to a photoswitchable molecule to control the synthesis of multimetallic Ag and Au nanoparticles under ambient conditions. AgBP1, a Ag-binding peptide was linked to MAM-CAuBP1, a maleimide-azobenzene-maleimide coupled previously with AuBP1, a Au binding peptide. The linked peptides retained their ability to passivate and stabilize Ag and Au nanoparticles, where a distinct assembly formation was most evident at a metal:peptide ratio of 2. Experimental data revealed a tunable materials-binding based upon the isomer and metal employed. This work is the first step in generating an externally actuated biomolecule with specific material-binding properties that could lead to controlled nanoparticle assemblies.

5.2 Motivation

It is well established that materials on the nanoscale possess unique properties based upon their size of < 100 nm.²¹ To address the production of such materials, extensive research has been invested in the development of numerous synthetic strategies;¹⁵⁹⁻¹⁶¹ however, the next grand challenge with nanoscale materials is their controlled organization into intricate 3D assemblies from which emergent properties could be realized for applications in plasmonics, sensing, catalysis, diagnostics, etc.^{139-140, 162} Unfortunately, direct routes to create positionally encoded nanoparticle assemblies over the nano to millimeter length

scales remain limited,^{34, 163} the ability to spatially orient materials of more than one composition into a controlled assembly has also proven to be of significant difficulty.¹⁶⁴ Furthermore, nearly all current assembly strategies produces static structures of a single orientation.¹⁴⁵ To realize the promise that nanoassemblies offer, new, facile, and direct assembly strategies are required that permit the controlled reconfiguration and reorientation of the individual components within the framework via external stimulus.

Bionanocombinatorics is an emerging field with the goal of exploiting biological-based pathways for the creation of 3D nanomaterial assemblies of multiple compositions and arrangements.^{139-140, 162} Such a principle is modeled upon assembly strategies observed in nature, which are driven via the interactions of inorganic materials with biological molecules such as peptides, proteins and DNA.^{2, 133} DNA-based approaches are well known for the generation of nanoparticle assemblies;^{132-134, 165} however, oligonucleotides lack material-specific binding and require a dense DNA overlayer for assembly.¹³³ Conversely, materials-binding peptides are known to be highly specific for nanoparticles of different inorganic composition.^{130, 139-140} These dodecamer sequences are isolated via biocombinatorial selection methods, thus engendering them with great affinity for their target materials.² Using these biomolecules, nanoparticles of controllable sizes, morphologies, and surface structures can be prepared of compositions including metals, metal oxides, and metal sulfides.^{40, 130, 140, 166}

Owing to their material selective affinity, peptides represent optimal biomolecules to drive the controlled assembly of multicomponent materials. For example, Slocik, *et al.*, employed a hybrid peptide consisting of a Au-binding sequence connected to a Pd-binding sequence to deposit small Pd nanoparticles onto the surface of larger Au particles.¹⁶⁷ Rosi

and colleagues have also explored Au-binding peptides for use in creating Au nanoparticle double helices.^{34-35, 37} Through the attachment of an alkyl chain to the N-terminus of the sequence, left- and right-handed Au nanoparticle helices were assembled where the twist was controlled by the chirality of the amino acids in the peptide.^{34-35, 37} While these examples present the opportunities that are possible using peptides, the generation of multimaterial 3D assemblies using peptides has not been realized. Furthermore, based upon the modular nature of peptide synthesis, non-natural components can be readily incorporated into the sequence, thus allowing for the integration of stimuli responsive moieties that controllably change the peptide structure in nanoparticle assemblies, leading or reconfiguration of the 3D material framework.

In Chapter 4, we explored the role of reductant on the formation of Au nanoparticles, capped with three different materials-binding peptides. In this chapter, we will develop further the use of such materials-binding peptides into applications such as assembly. Here we expand upon the bionanocombinatorics principle for multimaterial assembly using a multidomain peptide. For this, two peptides isolated with affinity for Au (AuBP1, WAGAKRLVLRRE)¹³⁵ and Ag (AgBP1, (TGIFKSARAMRN)^{51, 168} were linked with an azobenzene-based spacer to create a Peptide Assembly Responsive Element (PARE). In this arrangement, the N-terminal domain was designed for affinity to Ag surfaces, while the C-terminal domain was anticipated to bind to Au materials. Separating the two inorganic binding domains was the photoactuatable azobenzene species that can isomerize via light. Once the PARE was completely confirmed, the affinity for Au and Ag surfaces was quantified using Quartz Crystal Microbalance (QCM) analyses. The PARE was subsequently employed for Au and Ag nanoparticle fabrication, where the individual

materials were fully analyzed via UV-vis spectroscopy and Transmission Electron Microscopy (TEM). The particle size and morphology was observed to be dependent upon the metal ion concentration and composition.

Next, the formation of Au and Ag nanoparticle assemblies was explored using the PARE. For this, nanoparticles capped with the PARE were synthesized. These materials were then used to drive assembly via production of the second nanoparticle composition. The assembly process was explored as a function of metal composition and concentration, as well as the conformation of the azobenzene unit. Characterization of assembly formation was processed via TEM, Energy Dispersive Spectroscopy (EDS) mapping, and Small Angle X-ray Scattering (SAXS). These results suggested that controlled nanoparticle assembly was possible; however, sample drying appears to be important to achieve assembly formation. These results indicated that multimaterial assembly via peptide-based approaches is possible, which could be explored to generate materials for important optical and sensing applications.

5.3 Methods

5.3.1 Materials

Fmoc (9-fluorenylmethoxycarbonyl) protected amino acids and Wang resins were purchased from Advanced ChemTech, as well as coupling reagents piperidine, DIPEA (*N,N*-diisopropylethylamine), HOBt hydrate (hydroxybenzotriazole) and HBTU (*N,N,N',N'*-tetramethyl-*O*-(1H-benzotriazol-1-yl)uronium hexafluorophosphate). DMF (*N,N*-dimethylformamide), acetonitrile, ethyl ether, H₂O₂ (30% w/w), ammonium

hydroxide (20% v/v) and methanol were supplied from BDH Chemicals, while TFA (trifluoroacetic acid) and thioanisole was obtained from Alfa Aesar. Anisole, AgNO₃, and NaBH₄ were purchased from Acros Organics, while EDT (1,2-ethanedithiol) was from Fluka Analytical. HAuCl₄ was supplied from Sigma Aldrich. Hellmanex was obtained from Hellma, while ethanol was purchased from Koptec. All materials were used as received without further purification.

5.3.2 Peptide Synthesis

CAuBP1 and AgBP1C were synthesized using standard solid phase peptide synthesis protocols⁹⁸ on a Tetras Peptide Synthesizer (Creosalus). Peptides were cleaved using TFA with EDT, thioanisole, and anisole as scavengers. Cleaved peptides were purified using reverse phase HPLC and the molecular weight was verified with MALDI-TOF mass spectrometry.

5.3.3 PARE Molecule Synthesis

Production of the MAM and coupling of the peptides was processed based upon previously published protocols.¹⁶⁹ Briefly, 13.5 mg of CAuBP1 was mixed with 5.8 mg of MAM (1.3:1 MAM:peptide molar ratio) in 1.50 mL of DMF for 3 days, after which any unreacted MAM was removed through washing with ethyl ether; the MAM-CAuBP1 complex forms a yellow precipitate in ethyl ether. This precipitate was then dissolved in water, purified with reverse phase HPLC, and confirmed with MALDI-TOF. The MAM-CAuBP1 was lyophilized to a powder where it was then mixed with AgBP1C at a 1:1.3 molar ratio of MAM-CAuBP1 to AgBP1C. This mixture was stirred in 3.00 mL of water for 3 days,

upon which the solution was again purified via reverse phase HPLC. The final product was verified using MALDI-TOF, lyophilized, and stored at $-80\text{ }^{\circ}\text{C}$ until further use.

5.3.4 QCM Binding Analysis

QCM studies were conducted with a Q-Sense E4 QCM-D system (Biolin Scientific). Commercially available Au sensors were employed for Au binding analyses, while Ag was sputtercoated onto the Au sensors for the Ag binding studies.¹⁴⁰ All binding studies were processed using previously published methods.^{139-140, 169}

5.3.5 Nanoparticle Synthesis

Monometallic nanoparticles were prepared with either *cis* or *trans* PARE, where the *cis* isomer required constant irradiation at 365 nm, while the *trans* isomer occurred under ambient light. The samples were prepared at increasing metal:PARE ratios of 1 – 4. For the 1 ratio, 350 μL of 1.00 mg/mL PARE in 610 μL of water was mixed with 10 μL of either 0.01 M AgNO_3 or HAuCl_4 , and allowed to complex for 15 min. The solutions were then reduced with a 3-fold excess of NaBH_4 overnight. This method was the same for all ratios except for as the metal volume increased, the water volume was decreased due to the volume of metal solution added.

Sequential metal ion addition and reduction into the monometallic solutions was used to form the multimetallic assemblies. The isomer used for the monometallic nanoparticles was conserved throughout the multimetallic nanoparticle synthesis. Also, the same ratio of the metal:PARE was employed for the second metal addition. Thus, for the 1 ratio, 10 μL of either 0.01 M AgNO_3 or HAuCl_4 was added to the monometallic particle solutions. This

was the same for all the ratios prepared (1 – 4). If Au was the second metal, a 3-fold excess of NaBH₄ was added simultaneously, while if Ag was the second metal, 15 min of complexation time was included prior to the addition of NaBH₄. The multimetallic solutions then reduced overnight before further analysis.

5.3.6 Characterization

UV-vis analysis was conducted using an Agilent 8453 UV-vis spectrometer with a 5 mm quartz cuvette (VWR). All cuvettes were cleaned with aqua regia prior to use. All spectra were background subtracted using water as the blank. TEM images were obtained through a JEOL JEM-2010 transmission electron microscope at 200 kV. The samples were prepared by drop casting 5.00 μL of solution onto a 200 mesh carbon-coated Cu grid (Ted Pella).

5.4 Results and Discussion

5.4.1 PARE Synthesis

The PARE molecule was synthesized via the mechanism of Figure 5.1, where the spacer component was synthesized as previously described.¹⁶⁹ For this, an azobenzene was produced that displayed two maleimide groups (molecule termed MAM). With this, thiol/maleimide coupling can be easily processed in solution to generate the full PARE. The individual peptide sequences were fabricated using standard solid phase Fmoc

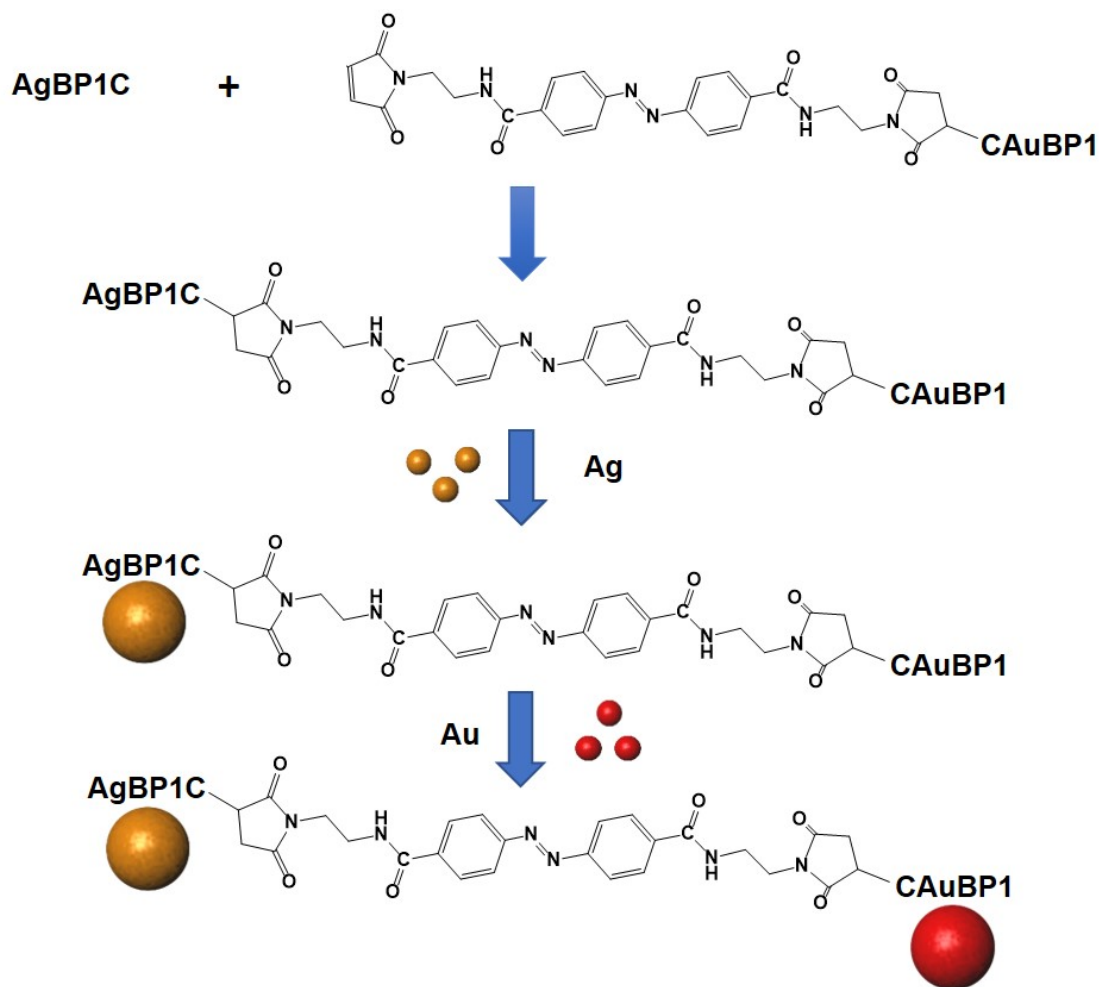


Figure 5.1. Representation of protocol for PARE and multimetallic nanoparticle synthesis.

protocols.⁹⁸ Cysteine residues were incorporated into both sequences to ensure site specific coupling to the maleimides of the MAM unit. For the AuBP1 peptide, the cysteine was incorporated at the N-terminus (CAuBP1), while the cysteine was added at the C-terminus for the AgBP1 peptide (AgBP1C). These two sequences were selected as they were previously shown to be the most selective for their target surfaces.¹⁴⁰

Once the individual components were synthesized, coupling to form the PARE was processed. For this, the AuBP1C was mixed with the MAM unit in DMF. DMF was required as the MAM unit itself was not water soluble. Excess MAM was present to ensure only one coupling event occurred to generate the AuBP1C-MAM species. The coupling

was allowed to stir for 3 days, after which the materials were purified by reverse phase HPLC and confirmed via MALDI-TOF. The AuBP1C-MAM species was now aqueously soluble, thus it was dissolved in water in the presence of the AgBP1C to drive the final coupling process to synthesize the complete PARE. The second coupling was processed for 3 days, purified, and confirmed via mass spectrometry.

5.4.2 Binding Quantification

The binding strength of the PARE was studied to the target Au and Ag surfaces via QCM. The peptides were flowed over the metallic sensors at four concentrations to measure the change in frequency as a function of PARE binding. Langmuir fitting of the data was applied to determine k_{obs} for each concentration, as previously described.^{139, 170} The individual k_{obs} values were then plotted as a function of PARE concentration, where the linear fit provided the association (k_a) and dissociation (k_d) values from the slope and y -intercept, respectively. These values were subsequently employed to calculate the free energy of binding (ΔG), where the ΔG values are reported in Table 4. PARE binding was studied on both the Au and Ag surfaces with the azobenzene in either the *cis* or *trans* conformation. For the *trans* PARE isomer, a ΔG value of -37.9 ± 2.8 kJ/mol was determined for binding to Au, while a value of -34.5 ± 0.7 kJ/mol was quantified for Ag. For the *cis* isomers, similar values were calculated: -34.2 ± 0.7 kJ/mol for Au and -34.9 ± 0.9 kJ/mol for Ag. Interestingly, the binding strength for the *trans* PARE on Au was similar to the free AuBP1 on Au (-37.6 ± 0.9 kJ/mol).¹³⁹ The other situations (*trans* PARE on Ag, *cis* PARE on Au and Ag) have binding affinities more similar to those seen with the free

Peptide	ΔG (kJ/mol) on Au	ΔG (kJ/mol) on Ag
AuBP1*	-37.6 ± 0.9	-35.3 ± 0.8
AgBP1*	-31.6 ± 0.2	-35.9 ± 1.0
<i>trans</i> PARE	-37.9 ± 2.8	-34.5 ± 0.7
<i>cis</i> PARE	-34.2 ± 0.7	-34.9 ± 0.9

Table 4. Binding energies calculated from QCM studies using the PARE peptide.

*Values obtained from refs. 139 – 140.

AuBP1 and AgBP1 on Ag, -35.3 ± 0.8 kJ/mol and -35.9 ± 1.0 kJ/mol, respectively (Table 4).¹⁴⁰ Interestingly, none of the binding affinities were as low as the ΔG determined for the free AgBP1 on Au at -31.6 ± 0.2 kJ/mol (Table 4).¹³⁹ This suggests that the integration of the sequences and the isomerization state of the azobenzene have a noticeable impact on the binding selectivity of the PARE molecule on the two different metallic surfaces.

5.4.3 Nanoparticle Synthesis

Multimaterial structure formation was processed by first generating PARE-capped nanoparticles of a single composition. To these materials, metal ions were added and reduced, thereby generating particles of the second composition to drive the assembly process. In the initial nanoparticle synthesis, two different variables were explored: the isomerization of the MAM in the PARE (*cis* or *trans*) and the metal:PARE ratio. For the effects of isomerization, the peptide was in the *trans* form in ambient light, which was confirmed via UV-vis spectroscopy. To generate the *cis* isomer, the PARE stock solution was irradiated with 365 nm light for at least 30 min. Formation of the *cis* isomer was identified via a decrease in the π - π^* transition at 330 nm as observed via UV-vis

spectroscopy.¹⁷¹ To ensure that the azobenzene remained in the *cis* conformation during nanoparticle synthesis, the reaction was conducted under continual illumination at 365 nm.

To prepare Au or Ag nanoparticles capped with the PARE, the desired isomer was mixed with Ag⁺ or Au³⁺ ions in water at a metal:PARE ratio of 1-4. The metal ions were allowed to complex with the biomolecule for 15 min prior to reduction with excess NaBH₄. The materials were allowed to stand overnight to ensure production of stable structures. In this situation, four different monometallic particles were generated: Au and Ag particles capped with the PARE in the *cis* and *trans* form.

Once the materials were prepared, their optical properties were examined via UV-vis spectroscopy. As presented in Figure 5.2a, Ag nanoparticles capped with the *trans* PARE showed a distinct Localized Surface Plasmon Resonance (LSPR) at 430 nm. The intensity of the LSPR increased as a function of the Ag⁺ concentration, as anticipated. The absorbance for the azobenzene moiety was also clearly observed at 330 nm. When the Ag nanoparticles were prepared using the *cis* PARE (Figure 5.2b) an LSPR at 430 nm was again observed whose intensity was dependent upon the Ag concentration. The difference between the Ag particles prepared with the *trans* and *cis* PARE was evident in the intensity of the absorbance for MAM at 330 nm, as the latter spectra showed a significantly decreased absorbance, indicative of the *cis* confirmation.¹⁶⁹

The PARE-capped Au nanoparticles were also examined via UV-vis for their optical properties. Interestingly, for the Au materials capped with both the *trans* and *cis* PARE, only the absorbance associated with the azobenzene was noted with no LSPR band for Au particles (Figure 5.2c-d). This suggests that the materials fabricated under these conditions are sufficiently small enough to not generate an LSPR (<2 nm for Au) or that the intensity

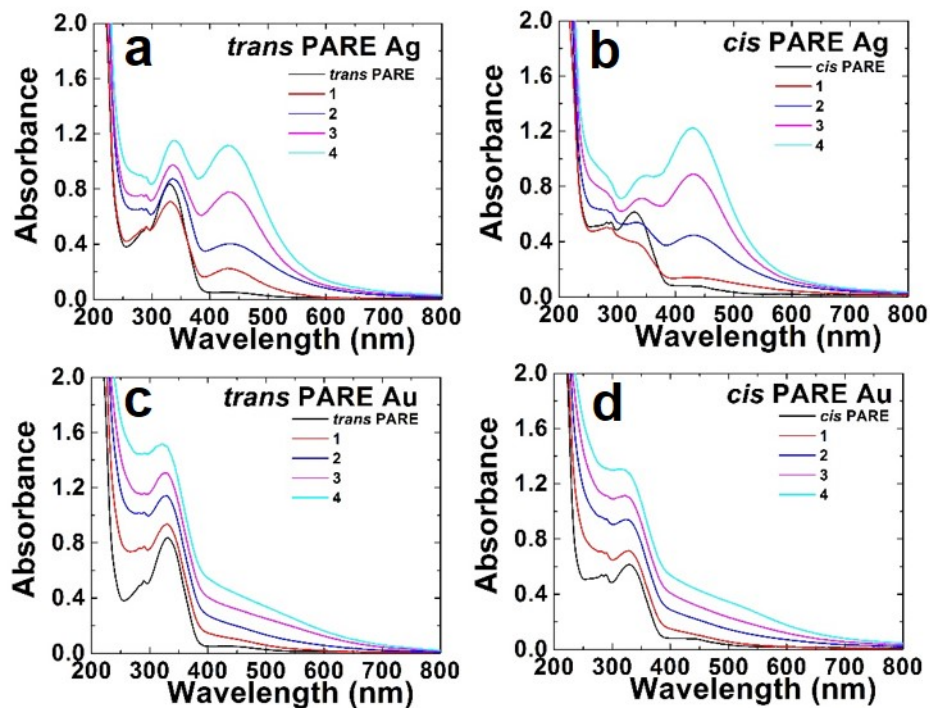


Figure 5.2. UV-vis spectra of PARE-capped monometallic nanoparticles. All samples were prepared at ratios of metal:PARE from 1-4. Part (a) shows *trans* PARE with Ag while part (b) depicts *cis* PARE with Ag. Part (c) is *trans* PARE with Au while part (d) shows *cis* PARE with Au.

of the plasmon is sufficiently small to be masked by particle light scattering. Note that the intensity of the azobenzene peak at 330 nm was consistent with the isomerization state of the molecule. Such an event with both the Au and Ag particles indicates that the azobenzene is able to photoisomerize when the PARE is bound to the metallic surface.

TEM analysis was conducted to determine the size and morphology of the Ag and Au nanoparticles capped with the PARE (Figure 5.3). To determine particle size distributions, a minimum of 100 nanoparticles were sized and averaged over different regions on the grid surface. For the Ag particles capped with the *trans* PARE, the size distributions ranged over a narrow window of 10.9 ± 4.7 nm for the material prepared at a metal:PARE ratio of 3 to 11.8 ± 4.6 nm generated at a ratio of 1. When the PARE was in the *cis* state, the Ag

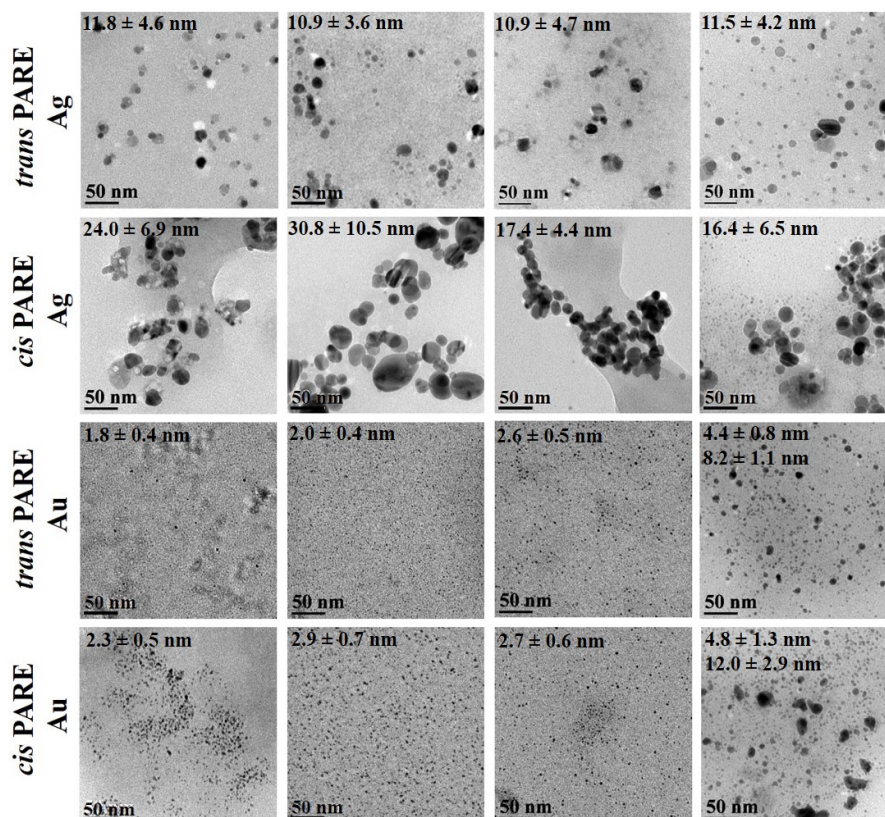


Figure 5.3. TEM images of the PARE-capped monometallic nanoparticles. Metal:PARE ratio increases in the columns left to right, from 1 – 4.

nanoparticles displayed unique differences in size distributions; for the materials generated at a ratio of 1 and 2, sizes of 24.0 ± 6.9 nm and 30.8 ± 10.5 nm, respectively, were noted, but at higher ratios of 3 and 4, sizes of 17.4 ± 4.4 nm and 16.4 ± 6.5 nm were observed, respectively.

TEM analysis of the PARE-capped Au nanoparticles demonstrated the production of substantially smaller materials as compared to the Ag structures. As seen in Figure 5.3, the Au nanoparticles generated with the *trans* PARE at a metal:PARE ratio of 1 and 2 displayed average diameters of 1.8 ± 0.4 and 2.0 ± 0.4 nm, respectively. As the metal loading increased to a ratio of 3, the particle size slightly increased to 2.6 ± 0.5 nm. Interestingly, at the greatest ratio studied, 4, a bimodal nanoparticle distribution was

observed where 80% had an average diameter of 4.4 ± 0.8 nm with the remaining 20% being 8.2 ± 1.1 nm.

When the Au nanoparticles were fabricated using the PARE in the *cis* conformation, similar material sizes were observed. In this regard, the particles prepared at a ratio of 1 were measured to have an average diameter of 2.3 ± 0.5 nm. As the metal loading increased in the samples generated at a ratio of 2 or 3, the particle size slightly increased to 2.9 ± 0.7 and 2.7 ± 0.6 nm, respectively. A bimodal material set was again observed with the PARE-capped Au nanoparticles at a ratio of 4. In this regard, 87% of the nanoparticles had an average diameter of 4.8 ± 1.3 nm, while the remaining 13% was 12.0 ± 2.9 nm.

When comparing the nanoparticles fabricated using the PARE, clear trends based upon the metallic composition and azobenzene isomerization state are noted. In this regard, in all cases, the Au nanoparticles are substantially smaller than the Ag nanoparticles capped with the same biomolecule. Such effects are consistent with previous studies.¹⁴⁰ Furthermore, for the Ag nanoparticles, significantly smaller materials are generated using the PARE in the *trans* state over *cis*. Interestingly, for the Au materials, no similar trend was noted based upon the azobenzene conformation. This suggests that the binding event of the biomolecule is more sensitive to the Ag surface over the Au based upon the PARE structural. In general, these results are consistent with the effect of peptide surface binding where the number of anchor residues, as determined by computational modeling, is anticipated to control the particle size.⁴⁰

5.4.4 Multimaterial Nanostructures

Once the monometallic nanoparticles were examined, the generation of multimetallic nanostructures was explored. To the PARE-capped nanoparticles, new metal ions of a different composition were added and subsequently reduced to drive the formation of multimetallic structures. The isomer of PARE employed in the monometallic nanoparticle synthesis was conserved in the multimetallic synthesis, so that *trans* PARE would remain *trans* upon addition of the second metal. With regards to metal composition, the identity of the second metal ion was varied to contrast the first metal nanoparticle formed (*i.e.* if PARE-capped Ag nanoparticles were used, then Au would be added second). To distinguish between the samples and order of production, the materials are labeled as *trans/cis* PARE (X, Y) where X and Y are either Ag or Au listed in the order of addition. Furthermore, the metal:PARE ratio was maintained throughout, from 1 to 4. To this end, the Au:Ag ratio was constant, but the metal:PARE ratio varied. This was achieved such that X equivalents of Au, X equivalents of Ag, and 1 equivalent of PARE were used where the X values ranged from 1-4.

To prepare (Ag, Au) multimetallic materials, Au^{3+} was added to PARE-capped Ag nanoparticles and was simultaneously reduced to limit galvanic exchange between the Au^{3+} ions and Ag nanoparticles; however, to prepare (Au, Ag), Ag^+ was complexed with the PARE-capped Au nanoparticles for 15 mins prior to reduction. As with the monometallics, the multimetallic materials were allowed to reduce overnight before further use. In this manner, four different systems were generated: *trans* PARE (Ag, Au), *cis* PARE (Ag, Au), *trans* PARE (Au, Ag), and *cis* PARE (Au, Ag).

Initial characterization of the multimetallic materials was processed using UV-vis spectroscopy (Figure 5.4). When considering (Ag, Au), a broad plasmon was evident, as seen in Figure 5.4a with *trans* PARE (Ag, Au). The LSPR resulting from the newly generated Au nanoparticles merged with the Ag LSPR at 430 nm and was seen to extend to 530 nm. As the metal:PARE ratio increased, an increased intensity of the merged LSPRs was observed, as well as a noted red-shifting to near 550 nm. Interestingly, the SPR for Ag at 430 nm remained in the materials formed at a metal:PARE ratio of 4, with another small peak for Au at 550 nm. In comparison to *trans*, the *cis* isomer of PARE (Ag, Au) yielded an expected absorbance decrease at 330 nm due to the conformation of MAM, but otherwise there were only minor absorbance differences between the isomers for (Ag, Au)

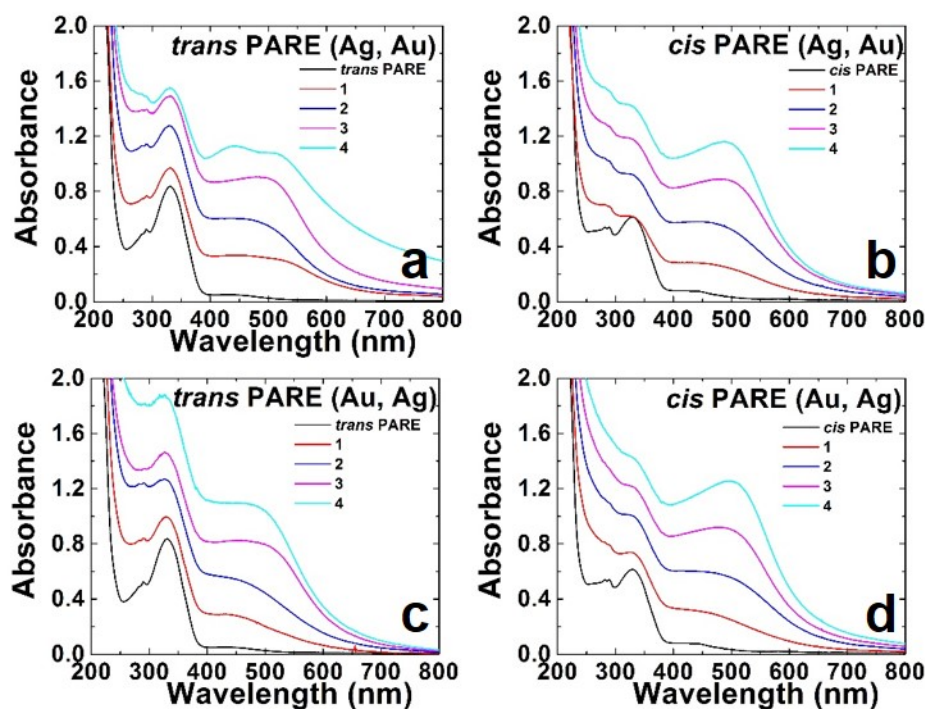


Figure 5.4. UV-vis spectra of PARE-capped multimetallic assemblies. All samples were prepared at ratios of metal:PARE from 1-4. Part (a) shows *trans* PARE (Ag, Au) while part (b) depicts *cis* PARE (Ag, Au). Part (c) is *trans* PARE (Au,Ag) while part (d) shows *cis* PARE (Au,Ag).

(Figure 5.4b). The most notable difference is the lack of two distinct LSPRs in the 4 sample; however, this is a very minor difference that may arise from minor particle size changes.

UV-vis analysis of the (Au, Ag) multimetallic materials (Figure 5c-d) revealed the emergence of a wide LSPR band at 430 – 530 nm. Such an event is quite notable since the PARE-capped Au nanoparticles did not form an LSPR. This band increased in intensity and red-shifted towards 550 nm with increasing the metal loading, similar to the (Ag, Au) materials. The shifting to longer wavelengths suggests that the materials are increasing in size or aggregation as additional metal is added. The expected decrease at 330 nm from the absorbance of MAM based upon isomerization was again noted, where *cis* isomers have a decreased intensity versus *trans*. Like the (Ag, Au) materials, the (Au, Ag) multimetallic structures did not show any significant optical differences between isomers.

While the UV-vis provided intriguing spectroscopic results, confirmation of the multimaterial structure was processed using TEM (Figure 5.5). For the *trans* PARE (Ag, Au) sample at a metal:PARE ratio of 1, a mixture of two material populations was observed: a great amount of individual nanoparticles and a noticeable number of small nanoparticle assemblies. As the metal loading increased to a ratio of 2, larger nanoparticle assemblies were observed mixed in the presence of individual particles. At the 3 and 4 ratios, larger aggregated nanoparticle superstructures were noted, but again a significant amount of individual nanoparticles were observed.

For the multimetallic materials generated in the *cis* PARE (Ag, Au) samples, Figure 5.5, highly distinct organized structures were noted. While present in small amounts in ratio of 1 system, the formation of assemblies was mostly seen at the ratio of 2. As observed with

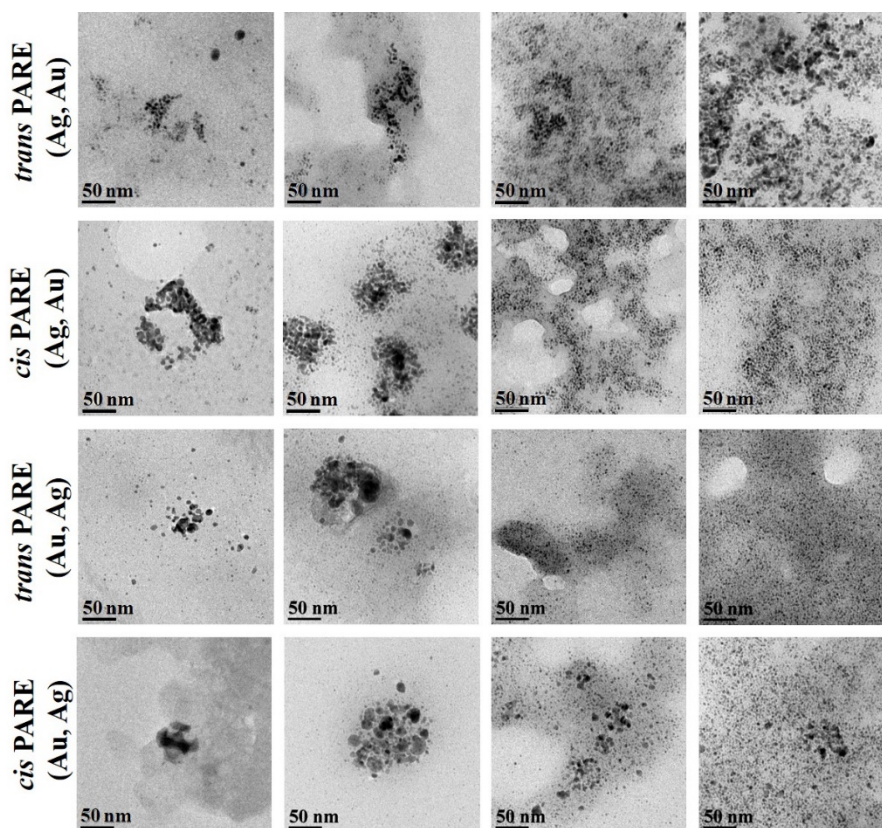


Figure 5.5. TEM images of the PARE-capped multimetallic assemblies. Metal ratio increases in the columns left to right, in ratios of 1-4.

the *trans* PARE system, as the metal:PARE ratio increased to 3 and 4, greater degrees of assembly were noted leading to aggregated structures.

When the multimetallic materials were generated with the PARE molecules using Au first followed by Ag (Au, Ag – Figure 5.5), similar organized structures were generated at lower ratios, while lesser degrees of aggregated assemblies were noted at the higher ratios. Such an effect was observed for the systems that employed the biomolecule in either the *cis* or *trans* form, and suggested that optimized multimetallic materials were generated by forming the Ag structures first, followed by Au. This is likely due to the differences in the binding of the PARE to the materials, where Ag binding is entropically controlled, which may facilitate secondary interactions with the Au materials.

To confirm the multimetallic composition of the small nanoparticle assemblies/aggregates, dark-field TEM with EDS mapping was conducted (Figure 5.6). For this analysis, the *cis* PARE (Ag, Au) sample generated at a ratio of 2 was studied. The dark field micrograph displayed several sets of assemblies dispersed amongst individual nanoparticles (Figure 5.6a). EDS mapping of the indicated region was subsequently processed, where the Ag and Au regions are presented in Figures 5.6b and c, respectively. The overlay of these two images (Figure 5.6d) revealed that the assemblies were indeed composed of both Au and Ag nanoparticles. Note that the white portions in the overlaid image represent regions where both Au and Ag are present in the assembly, further demonstrating the intimate interactions between the two metallic structures as a function of the PARE. The dark-field TEM images and EDS mapping of the three other conditions studied are included in Chapter 6.5, Figures 6.14-6.16.

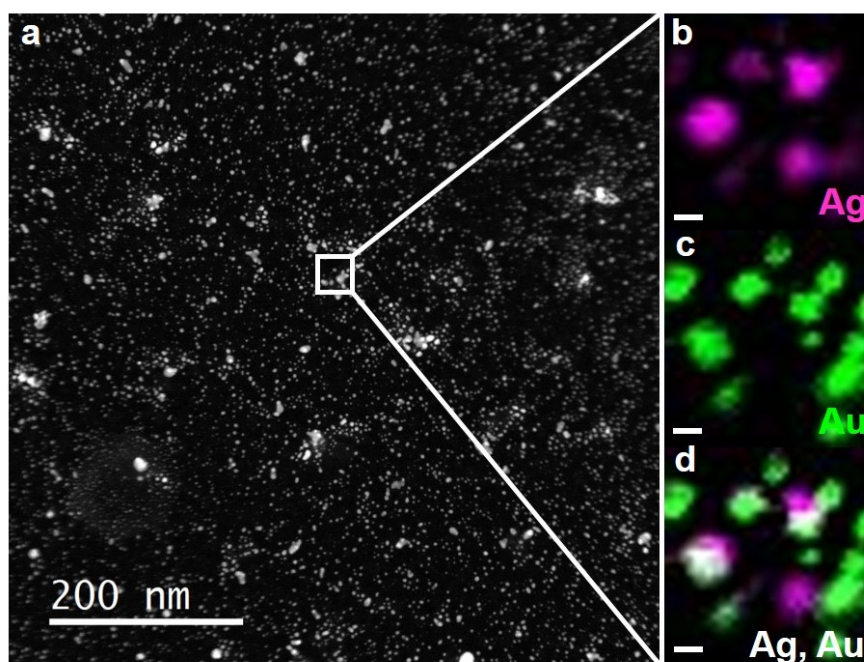


Figure 5.6. Dark-field TEM imaging and EDS mapping of *cis* PARE (Ag, Au) at a 2 ratio. Part (a) is the dark-field images while parts (b-d) show the EDS mapping. The scale bar for part (b-d) is 5 nm.

While the above TEM and elemental analyses suggest the formation of multimetallic structures/assemblies, the results are achieved in the solid state. Solvent evaporation is known to participate in the nanoparticle assembly,¹⁷² thus to ascertain information on the solution state structure of the materials, SAXS studies were conducted at the Advanced Photon Source at Argonne National Laboratory. The scattering of the PARE-based multimetallic materials prepared at a metal:biomolecule ratio of 2 were measured at 18 keV. The resultant scattering data were background subtracted, averaged, and analyzed using the Igor Pro software.¹⁰⁰ All four conditions (*cis* or *trans* PARE, Au or Ag first) showed a broad feature at $\sim 0.1 \text{ \AA}^{-1}$ in the scattering curves (Figure 5.7) which were modeled using a spherical form factor to determine material size. Modeling for *trans* and *cis* PARE (Ag, Au) revealed a large peak at $\sim 20 \text{ \AA}$ with a smaller peak at $\sim 40 \text{ \AA}$. Interestingly for the materials that generated with Au first (*trans* and *cis* PARE Au, Ag) revealed only one peak, at $\sim 20 \text{ \AA}$. Note that none of the features modeled from the SAXS analysis were large enough to correlate to the size expected for assembly formation. This suggests that drying effects play a pivotal role in the production of assemblies, where evaporation of the water from the sample while drying inverted influences the interactions between the nanoparticles.

From studying the UV-vis and TEM results of the PARE-capped monometallic nanoparticles, it is evident that the identity of the metal ion and the concentration affect particle size and morphology. When Ag is the first metal employed, larger nanoparticles resulted where the *trans* PARE appears to control the size with increasing metal concentration, but *cis* PARE does not exhibit the same level of control. When Au was the first component, small nanoparticles were formed, regardless of isomer, and no LSPR is

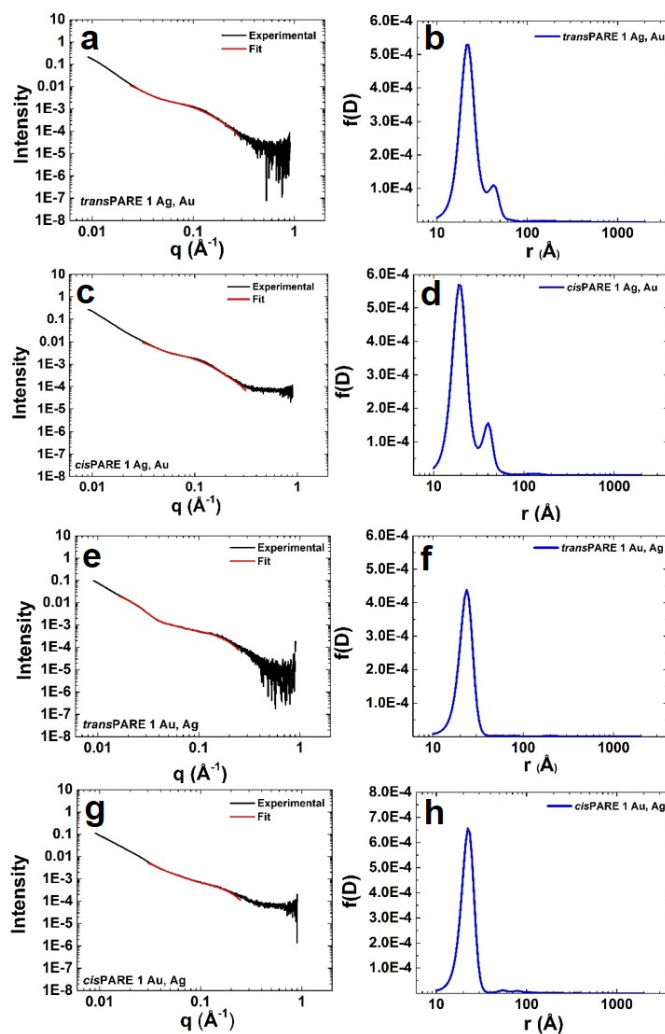


Figure 5.7. SAXS analysis of PARE assemblies at the 2 ratio. Parts a, c, e, and g show the scattering data with theoretical fitting (red line) while parts b, d, f, and h show the corresponding modeled nanoparticle diameter.

seen. The smaller Au nanoparticle formation seen is similar to previous studies.¹⁴⁰ Furthermore, the change in size between the isomers with regards to the Ag nanoparticle formation compared to the Au nanoparticle formation suggests that the PARE molecule is more sensitive to the Ag surface over Au.

Considering the analysis of the PARE-capped multimetallic assemblies, it is apparent that the order of metal addition or isomer employed has only a negligible effect on the

formation of assemblies. The LSPR bands observed for (Ag, Au) and (Au, Ag) assemblies are similar, as is the morphology of the particles prepared at a metal:peptide ratio of 2. All sets of data show increasing levels of aggregation with increasing metal concentration, although the (Au, Ag) materials appear to be less aggregated than (Ag, Au). This would be anticipated if the PARE peptide had a weaker binding affinity for Ag versus Au as it would lead to stronger Au interactions when Au is the second metal introduced, resulting in more control over particle formation at higher metal concentrations. Drying effects are likely a major contributor to the presence of observed assemblies, where the capillary forces from water evaporation on the TEM grids drive assembly, much like that seen in studies by El-Sayed and colleagues.¹⁷² The lack of control over forming solely assemblies is likely due to the length of the MAM between the two materials binding peptides, where a longer molecule would allow for more freedom to bind to the metal surface at a distance that is distinguishable through UV-vis and TEM analysis. Similar conclusions were made by Sidhaye *et al.* where Au nanoparticles were prepared for assembly using an azobenzene moiety and three varying molecules as ligands: benzyldimethylstearylammmonium chloride, octadecylamine, and dodadecylamine.¹⁷³ The ligands were prepared by adding the three molecules, individually, on both sides of the azobenzene, much like the peptides were added to the MAM molecule in the present study. Nanoparticles capped with the longest molecule, benzyldimethylstearylammmonium chloride, were found to have the most notable difference between the *cis* and *trans* isomer, as seen by examining the LSPRs and TEM images.¹⁷³

To further elucidate the role of the PARE biomolecule during metal nanoparticle synthesis, control experiments were conducted on materials prepared without PARE. In

this manner, the formation of both monometallic and multimetallic nanoparticles was replicated based on previous descriptions with the exception of the PARE molecule being excluded, where the volume of PARE was replaced with water to maintain the same metal concentrations. The control nanoparticles were prepared at the equivalent metal concentrations as the 2 ratio. To mimic the *trans* isomer, solutions were prepared in ambient light (termed ambient conditions), while to mimic *cis*, solutions were prepared under constant illumination at 365 nm (termed UV conditions).

Once stability of the controls was confirmed, UV-vis spectroscopy was used to explore the LSPR formation. As seen in the Chapter 6.5, Figure 6.17, the Ag monometallics resulted in LSPRs at 400 nm while the Au monometallics yielded LSPRs at 530 nm. The (Ag, Au) multimetallic solutions revealed broad absorption for the Ag component with a distinct peak for Au at 530 nm. Conversely, the (Au, Ag) multimetallic controls retained a notable LSPR at 530 nm for the Au component and also produced a new absorbance shoulder at 430 nm, corresponding to the Ag LSPR. Further TEM imaging (Chapter 6.5, Figure 6.18) show some discrete nanoparticles are visible for the Au monometallics while the remainder of the images, despite metal or condition employed, show no shape or size control resulting in general nanoparticle aggregation with no assembly. SAXS analysis (Chapter 6.5, Figure 6.19) showed a broad feature in the scattering curve at $\sim 0.1 \text{ \AA}^{-1}$ with diverse sizes ranging from 20 \AA to 100 \AA .

All in all, these results indicate that the PARE biomolecule is responsible for coordinating assembly in the multimetallic nanoparticles. The UV-vis for the controls maintain distinct LSPRs for the individual metals where the PARE-capped materials have merged LSPRs, suggesting a degree of spatial control in the assembled nanoparticles. TEM

images of the control samples show lack of shape and size control without any evidence of assembly, versus the general spherical shape in the monometallic nanoparticles and evidence of assembly in the multimetallic PARE systems. Furthermore, SAXS analysis indicates that the control samples have larger and more varied size distributions based upon the spherical form factor results, compared to the modeled sizes seen with the PARE materials.

Further control studies were conducted employing physical mixtures of the monometallic PARE nanoparticles at the 2 ratio. UV-vis spectroscopy (Chapter 6.5, Figure 6.20) showed LSPR formation for Ag at 430 nm but no LSPR formation for Au. TEM images of the mixtures (Chapter 6.5, Figure 6.21) revealed that the *trans* isomer mixture had limited formation of assemblies while the *cis* isomer mixture resulted in the formation of distinct nanoparticles only. SAXS studies of the mixtures (Chapter 6.5, Figure 6.22) showed the *trans* isomer having a broad feature in the scattering curve at $\sim 0.2 \text{ \AA}^{-1}$ with a corresponding peak from the spherical form factor model at $\sim 40 \text{ \AA}$ as well as additional peaks at $>100 \text{ \AA}$. Meanwhile the *cis* isomer had a broad feature at $\sim 0.1 \text{ \AA}^{-1}$ with a calculated size of $\sim 20 \text{ \AA}$ and $\sim 40 \text{ \AA}$.

The UV-vis analysis from the physical mixtures further indicates that sequential reduction of the metals in presence of the PARE molecule results in a broadened LSPR to include 550 nm, as the physical mixtures did not yield any peaks beyond 430 nm. This suggests that some level of spatial control, as well as facilitation of LSPR formation, is occurring in the original PARE-mediated formation of nanoparticles. The TEM images support that sequential reduction is optimal, as seen by minimal assembly formation, if any, among the physical mixtures. Also, while the SAXS analysis for the physical mixture

controls was similar to the PARE-capped systems, there were subtle differences between the two, particularly in the size modeling, indicating that assembly formation may be better promoted by sequential metal addition and reduction. Further studies of the physical mixtures may be required to equivocally state which method is optimal for assembly.

5.5 Summary and Conclusions

In summary, this study shows that the formation of a photoactuatable materials-binding molecule using a bionanocombinatorics approach is possible through the simple linking of the AuBP1 and AgBP1 peptides to an azobenzene spacer. This PARE peptide was then capable of mediating the synthesis of monometallic nanoparticles with Ag and Au individually, where UV-vis and TEM results reveal an effect on nanoparticle size and morphology based upon the metal ion concentration and composition. In this manner, the Ag nanoparticles showed more fluctuation in size and shape, while the Au nanoparticle morphologies were more tightly controlled by the PARE peptide. These PARE-capped nanoparticles were further used to synthesize multimetallic assemblies of both Ag and Au together. Assembly was evident in all four conditions studied, although drying effects appear to be driving the assembly process. Furthermore, no notable difference was discernable between materials with regards to the *cis* and *trans* isomer of the MAM. This lack of difference is likely due to the length of the MAM linker not being sufficient enough to allow for such changes in the morphology based upon isomerization to be visible. Regardless, this work remains an important first step in using a bionanocombinatorics approach for generating materials with controlled assembly.

Chapter 6. Additional Information

6.1 Supporting Information for Chapter 1

Peptide Name	Sequence	Inorganic Material	Reference
Q7	QQSWPIS	Pd	34
Pd4	TSNAVHPTLRHL	Pd	9, 24, 36, 38
R5	SSKKSGSYSGSKGSKRRIL	Pd	28, 40
BP7A	TLHVSSY	Pt	42, 43
T7	TLTTLTN	Pt	41, 43
S7	SSFPQPN	Pt	41, 43
<i>Cha's</i>	PWxxQRELSV	Pt	44
E5	CGGEVSALEKEVSALEKEVSALEKEVSALEKEVSALEK	Au	14
FlgA3	DYKDDDDKPAYSSGAPP-MPPF	Au	14
A3	AYSSGAPPMPFF	Au	51-53
D6	DDDDDD	Ag	15
E6	EEEEEE	Ag	15
Ge8	SLKMPHWPHLLP	Ag	10
Z1	GLHVMHKVAPPRGGGC	ZnO	64
G-12	GLHVMHKVAPPR	ZnO	65
GT-16	GLHVMHKVAPPRGGGC	ZnO	65
Ti-1	RKKRTKNPTHKLGGGW	TiO ₂	16
Ti-2	MRMIRRFPSLKGGGW	TiO ₂	16
Ti-3	KSLSRHDHIIHHGW	TiO ₂	16
Ti-4	TQHLSHPRYATKGGGW	TiO ₂	16
dTi-1 (H/R)	RKKRTKNPTRKLGGGW	TiO ₂	16
dTi-1 (RKK)	RKKRKKRKKRKKGGGW	TiO ₂	16
Ti(Si)-1	YPSAPPQWLTNT	TiO ₂	66
Ti(Si)- 4	ATTLHPPRTSLP	TiO ₂	66
BT1	HQPANDPSWYTG	BaTiO ₃	17
BT2	NTISGLRYAPHM	BaTiO ₃	17

Table 5. Materials-directing peptides discussed in Chapter 1.

6.2 Supporting Information for Chapter 2

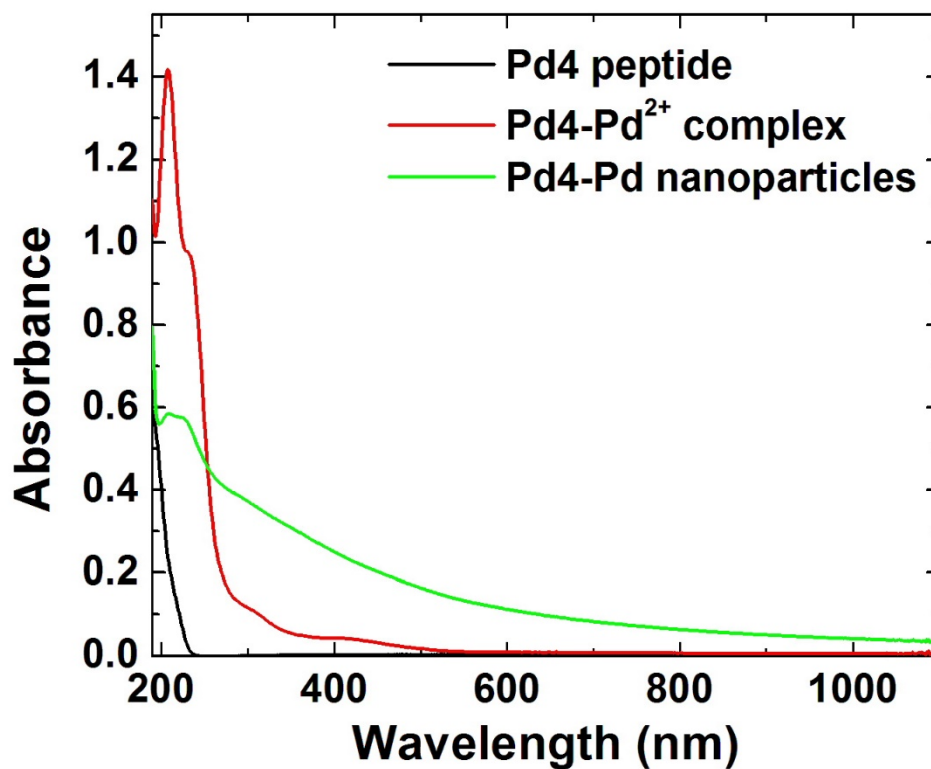


Figure 6.1. UV-vis analysis of the Pd4-capped Pd nanoparticless before and after reduction.

6.3 Supporting Information for Chapter 3

Conc. (M)	KOH	K ₃ PO ₄	Na ₂ CO ₃
0.10	Soluble	Soluble	Soluble
0.50	Soluble	Soluble	Soluble
0.75	Soluble	Soluble	Soluble
1.50	Soluble	Not Soluble	Not Soluble
1.87	Soluble	Not Soluble	Not Soluble
2.25	Soluble	Not Soluble	Not Soluble

Table 6. Solubility of 4-iodobenzoic acid in varying base concentrations.

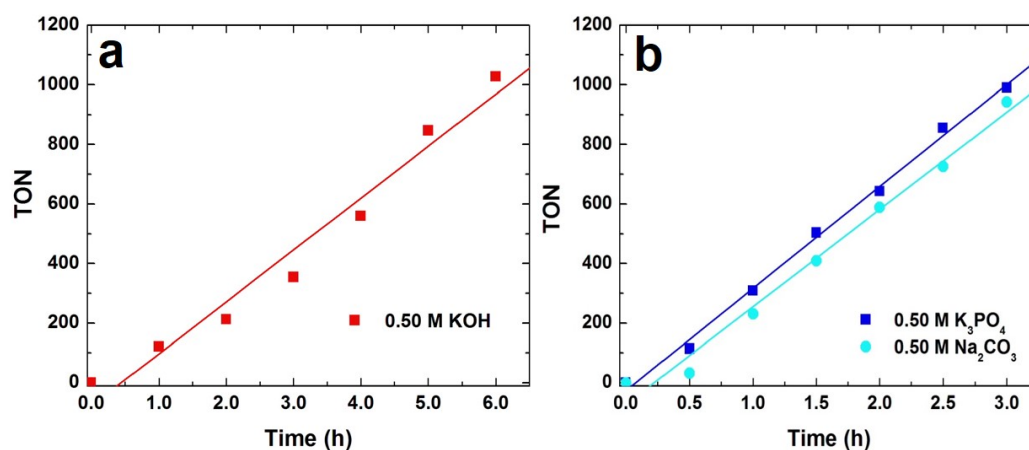


Figure 6.2. Biphenylcarboxylic acid product formation over time with all three bases at 0.5 M. Note that the times for the KOH system are longer due to slower reactivity. These plots were used to determine TOF values.

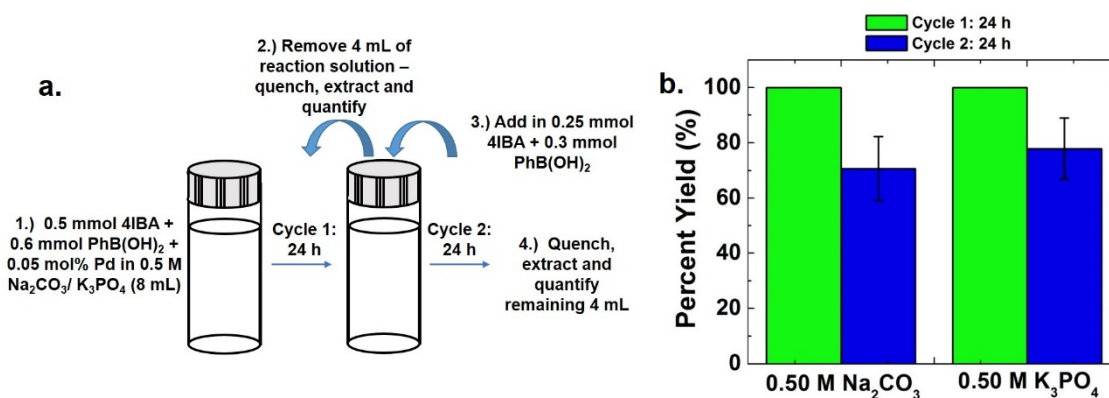


Figure 6.3. Recycling analysis. Part (a) presents the schematic description of how the Suzuki recycling studies were performed (note that the catalyst loading was maintained at 0.05 mol% over both cycles), while part (b) presents the resulting recycling yields done using the two bases that showed the highest activity.

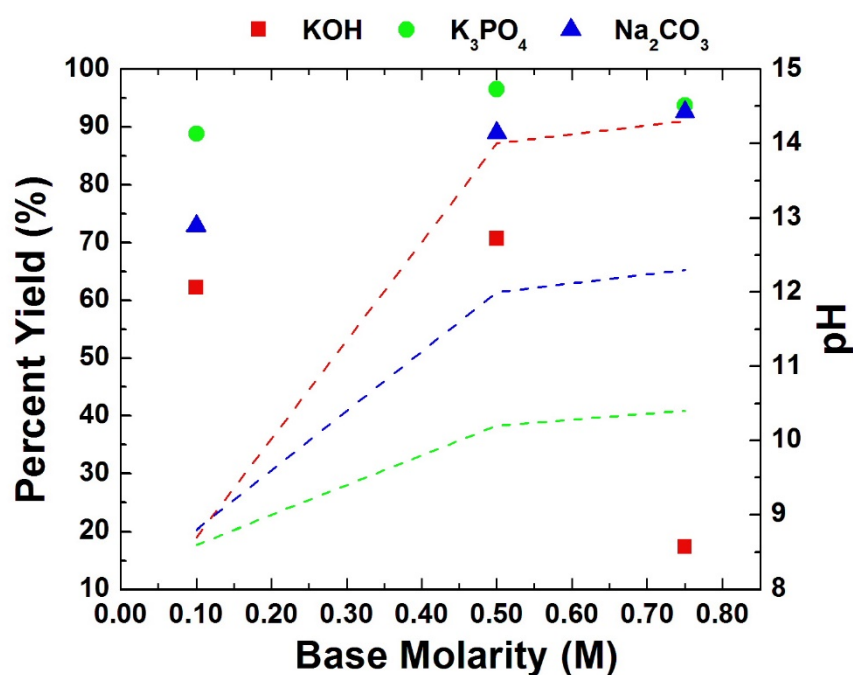


Figure 6.4. Graphical representation of product yield with varying base molarity and pH. The individual markers represent the yields from Suzuki coupling (left axis) while the dashed lines represent the corresponding pH (right axis). Note that at high KOH concentrations (> 0.1 M), accurate pH determination is not possible.

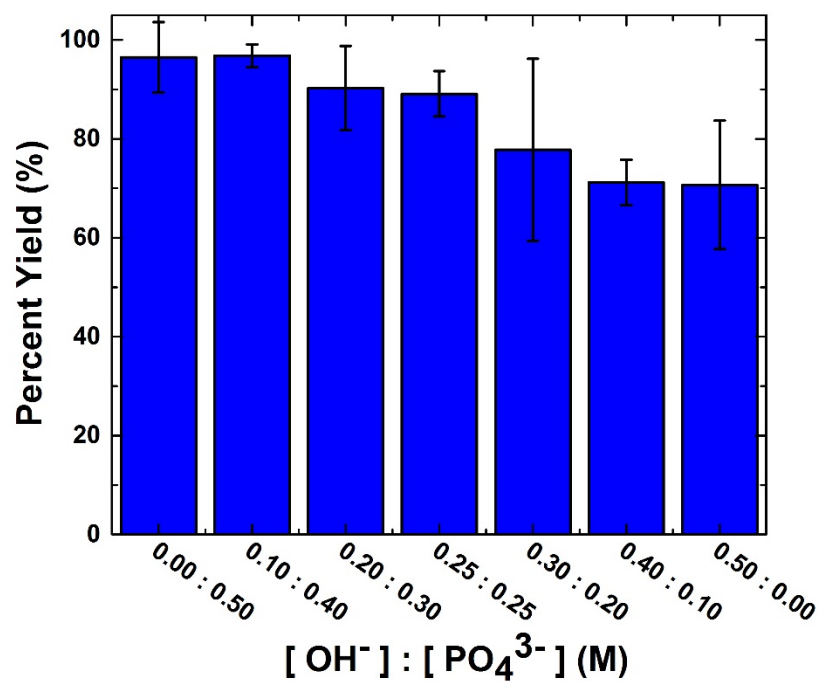


Figure 6.5. Suzuki coupling studies varying the ratio of KOH and K₃PO₄ while keeping overall base concentration constant at 0.50 M.

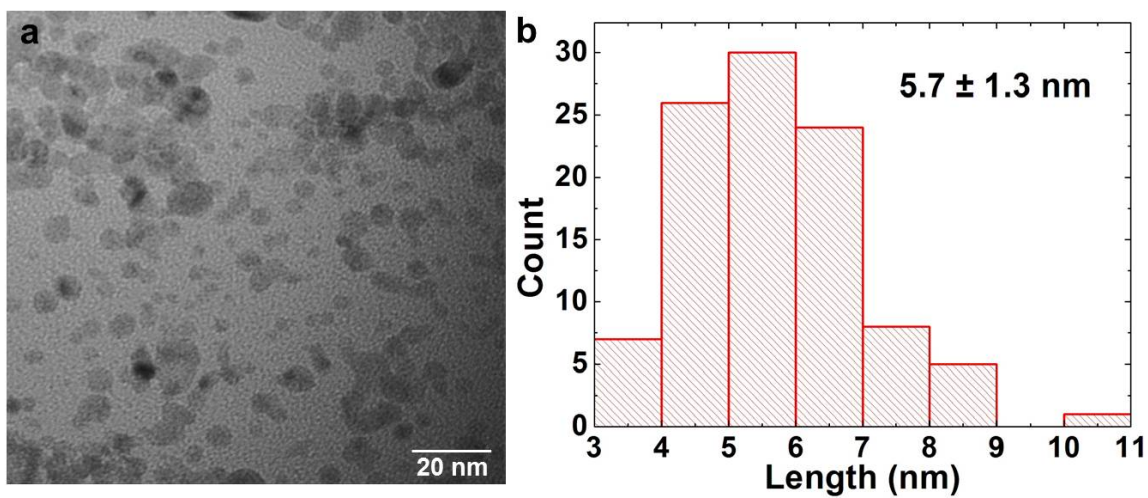


Figure 6.6. Characterization of the citrate-capped Pd nanoparticles. Part (a) presents a TEM image of the particles, while part (b) displays the particle sizing analysis.

6.4 Supporting Information for Chapter 4

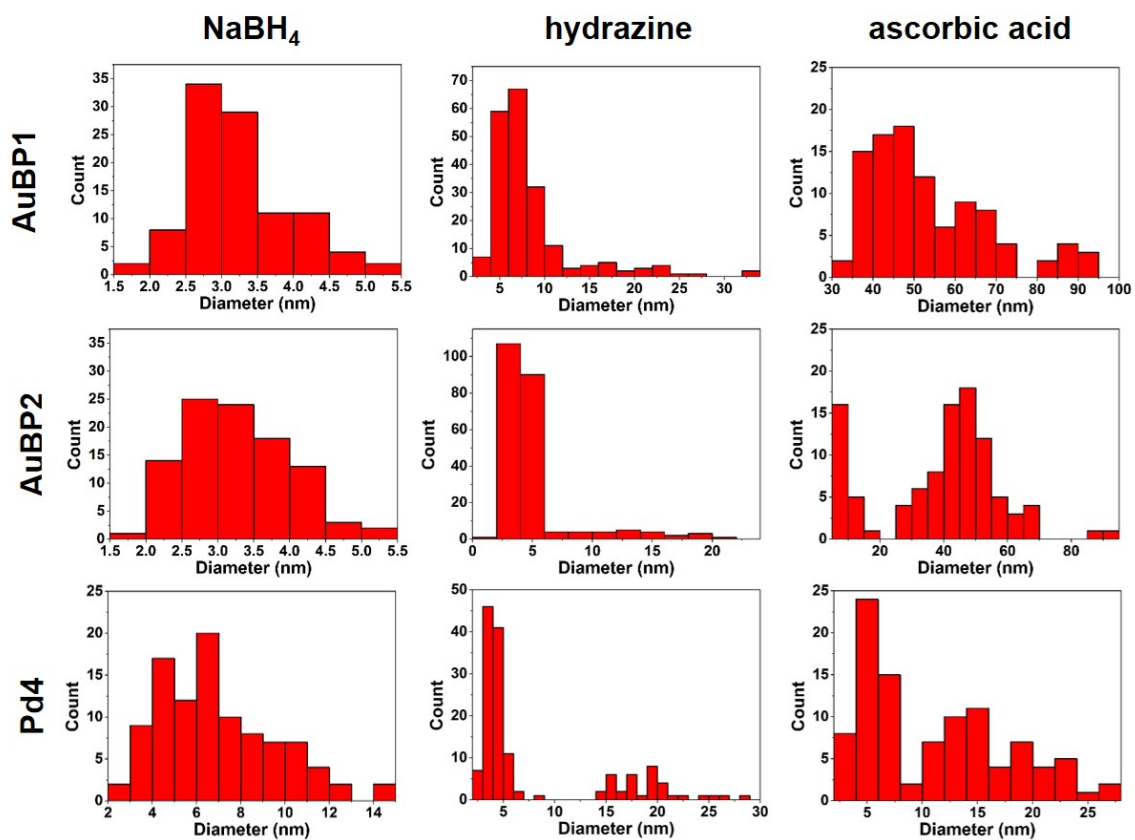


Figure 6.7. Au nanoparticle particle sizing analysis histograms.

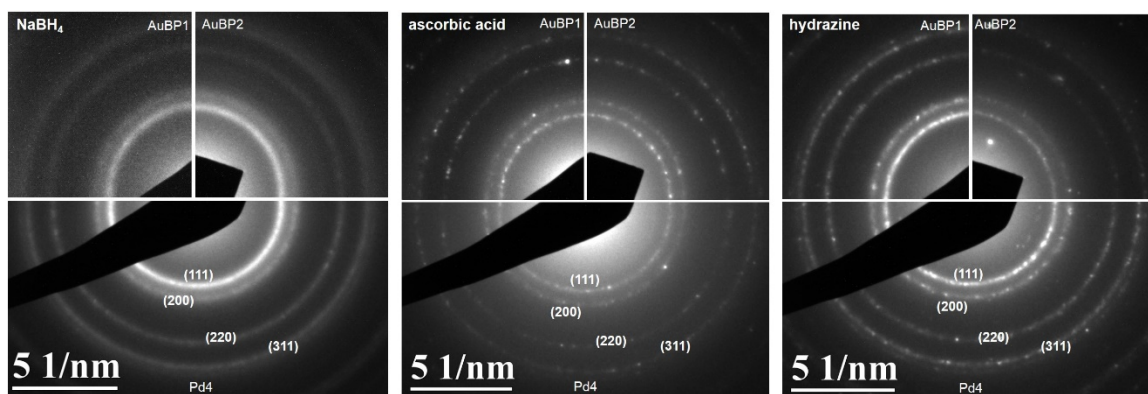


Figure 6.8. SAED patterns for the peptide-capped Au nanoparticles reduced with (left) NaBH_4 , (center) ascorbic acid, and (right) hydrazine. The peptide used to cap the nanoparticle is indicated in the image.

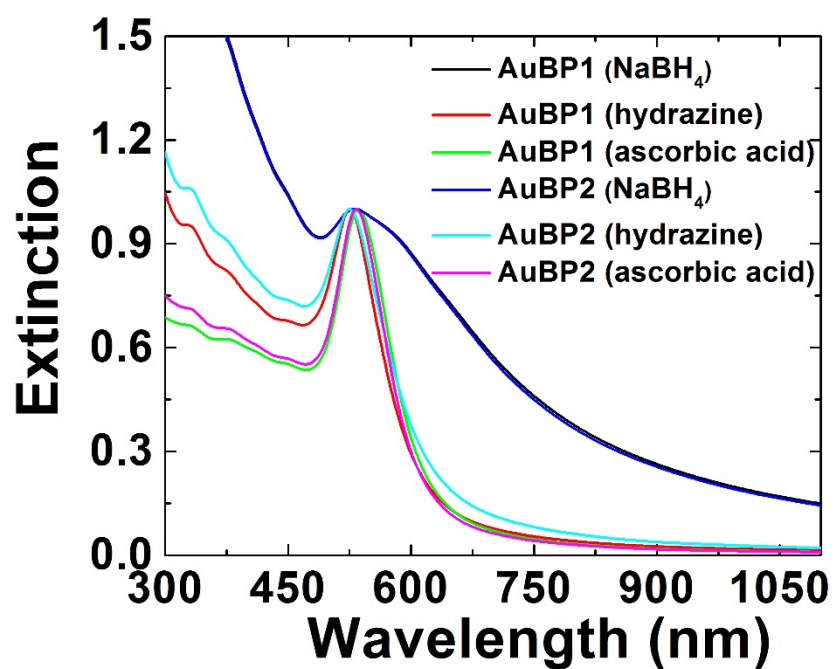


Figure 6.9. Calculated UV-vis spectra for AuBP1 and AuBP2-capped nanoparticles.

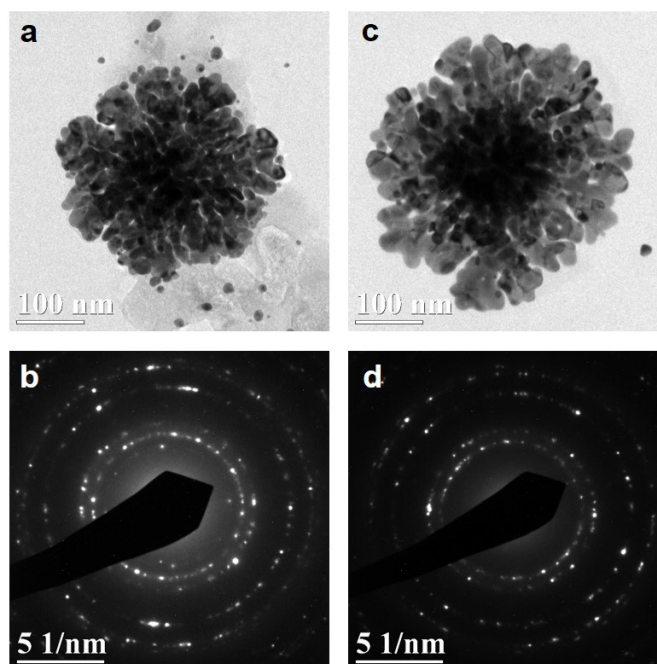


Figure 6.10. Analysis of AuBP1 and AuBP2 with Au and no reductant. Figures (a-b) show the TEM and SAED pattern of Au complexed with AuBP1 while (c-d) show AuBP2.

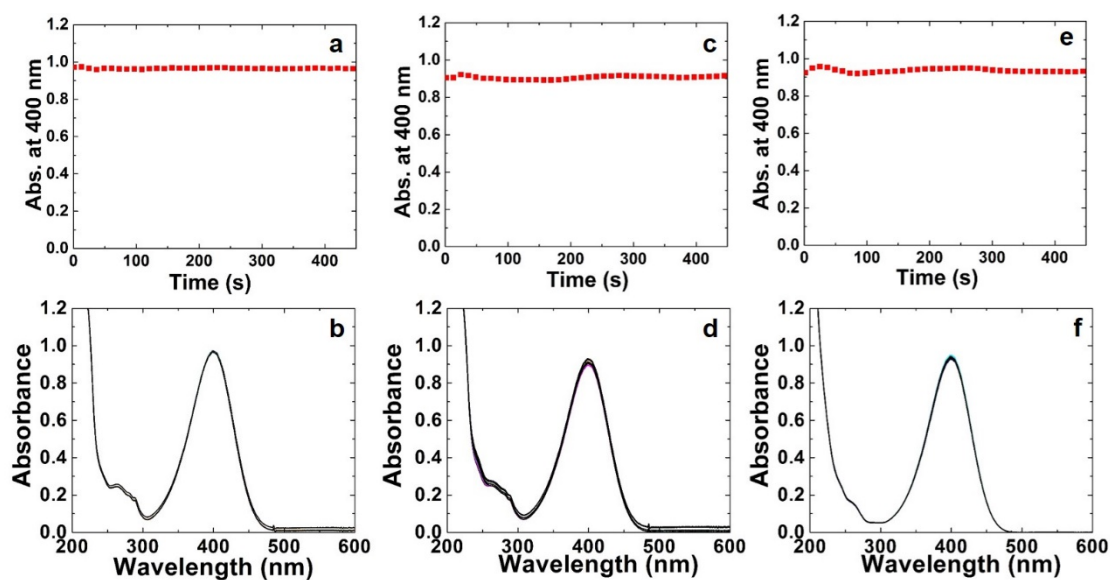


Figure 6.11. Control 4-nitrophenol reduction studies conducted using the peptide only. Figures (a, c, and e) show the change in absorbance at 400 nm over a 12 min time frame for the AuBP1, AuBP2 and Pd4 peptides, respectively, while Figures (b, d, and f) are the corresponding UV-vis spectra taken over the monitored time frame.

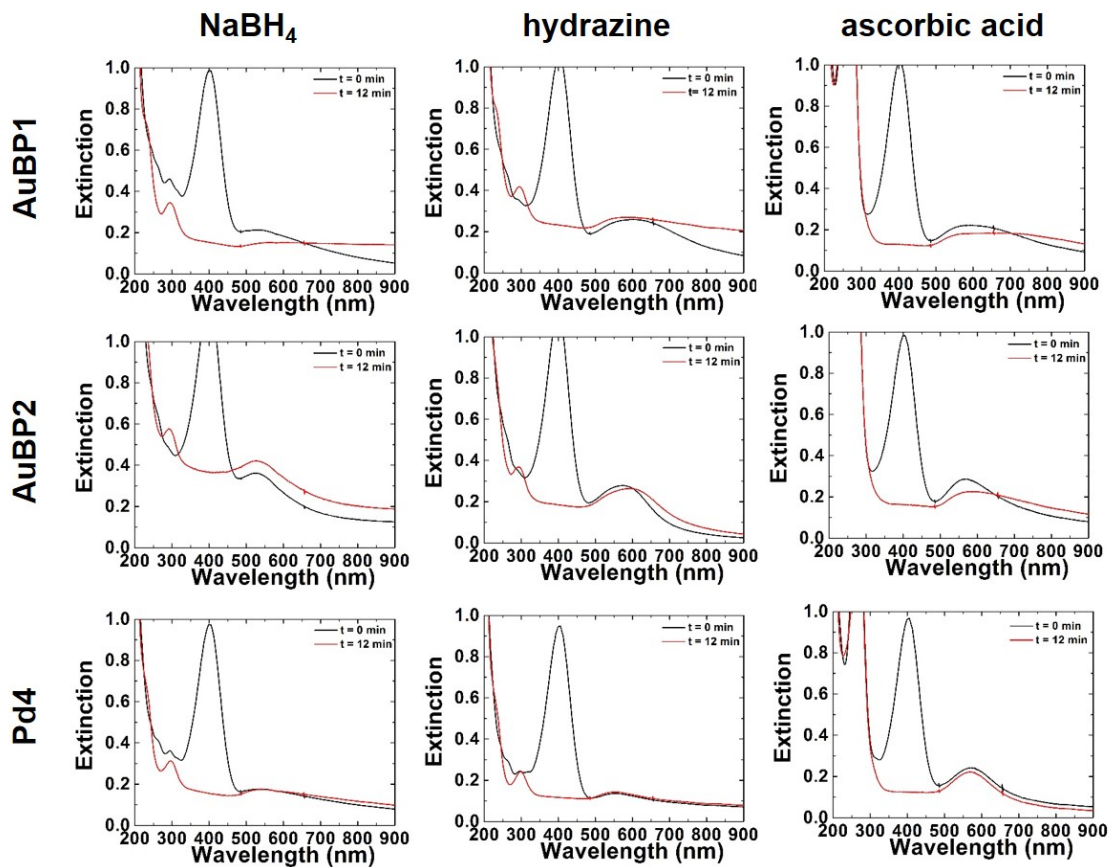


Figure 6.12. UV-vis of the first and last spectra during the 4-nitrophenol reduction reaction, where the black spectrum is from $t = 0$ min and the red spectrum is from $t = 12$ min.

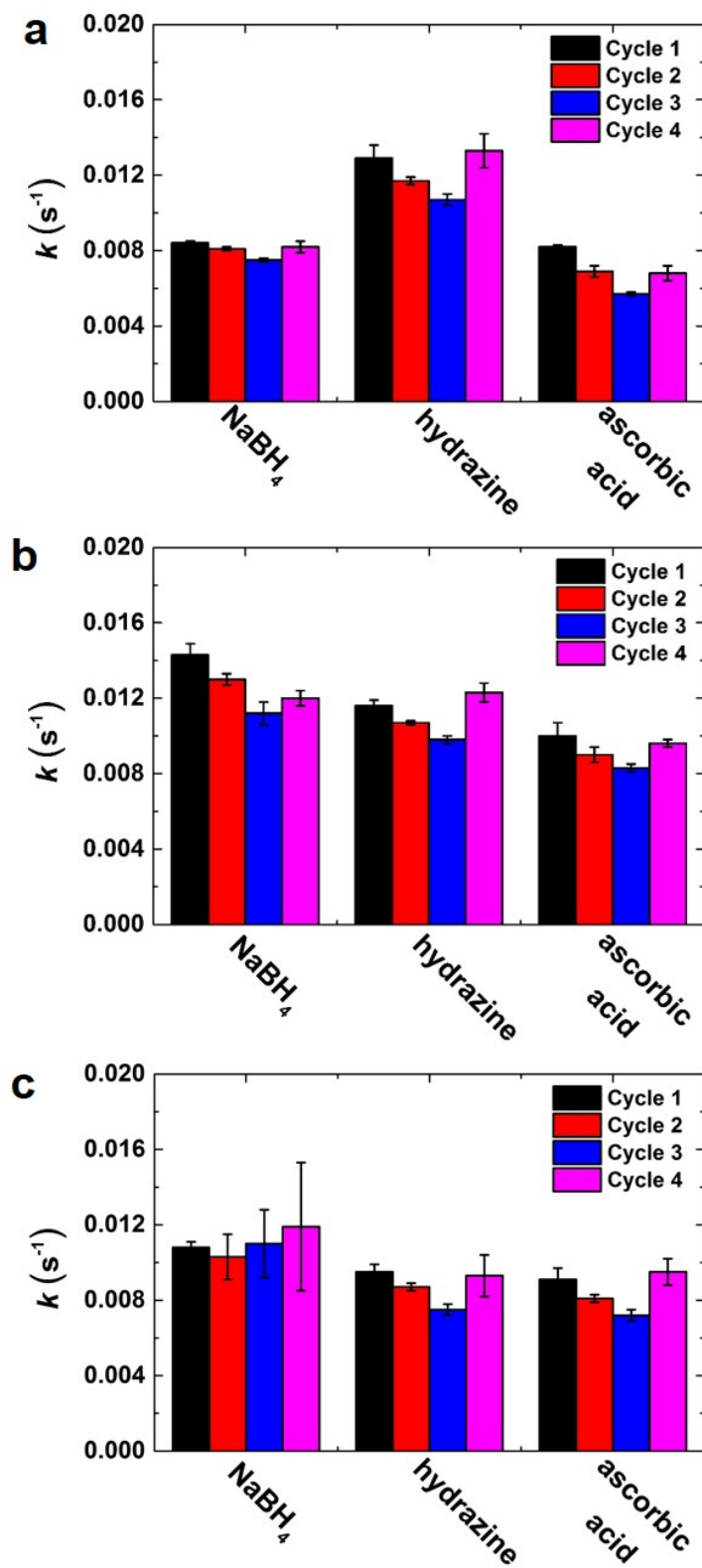


Figure 6.13. k values obtained from recycling studies of 4-nitrophenol reduction @ 20 °C. The Au nanoparticles in the study are capped with (a) AuBP1, (b) AuBP2, and (c) Pd4.

6.5 Supporting Information for Chapter 5

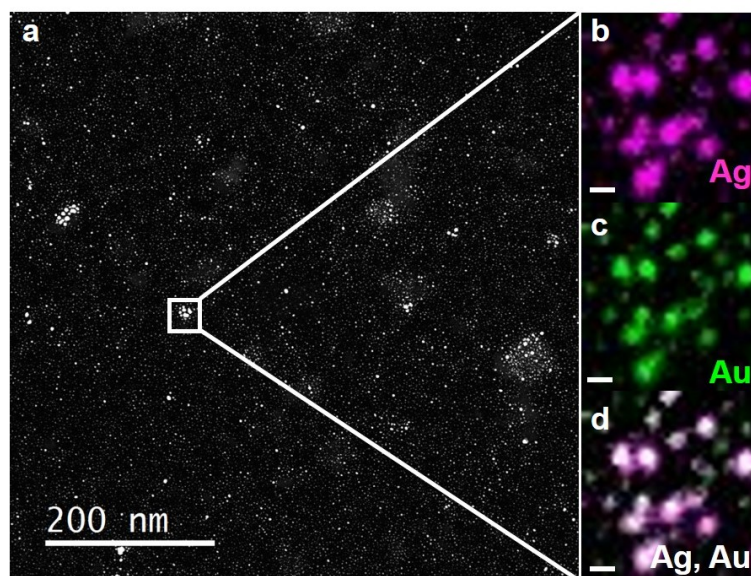


Figure 6.14. Dark-field TEM imaging and EDS mapping of *trans* PARE (Ag, Au) at a 2 ratio. Part (a) is the dark-field images while parts (b-d) show the EDS mapping. The scale bar for part (b-d) is 5 nm.

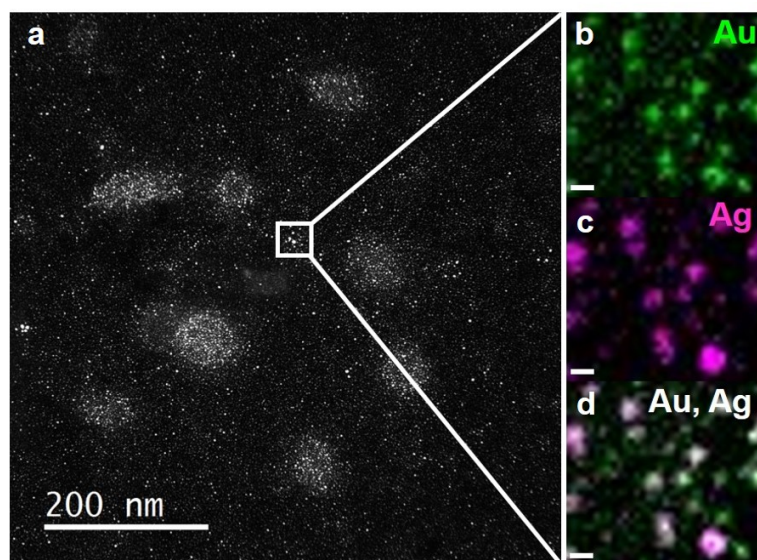


Figure 6.15. Dark-field TEM imaging and EDS mapping of *trans* PARE (Au, Ag) at a 2 ratio. Part (a) is the dark-field images while parts (b-d) show the EDS mapping. The scale bar for part (b-d) is 5 nm.

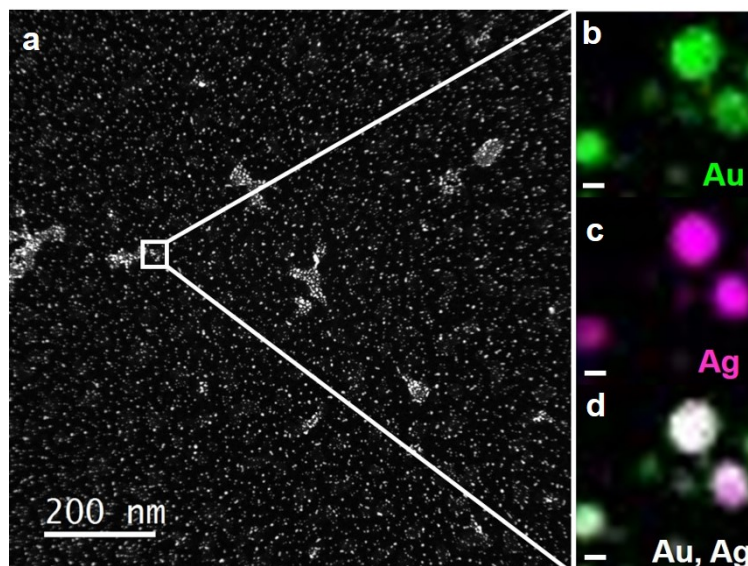


Figure 6.16. Dark-field TEM imaging and EDS mapping of *cis* PARE (Au, Ag) at a 2 ratio. Part (a) is the dark-field images while parts (b-d) show the EDS mapping. The scale bar for part (b-d) is 5 nm.

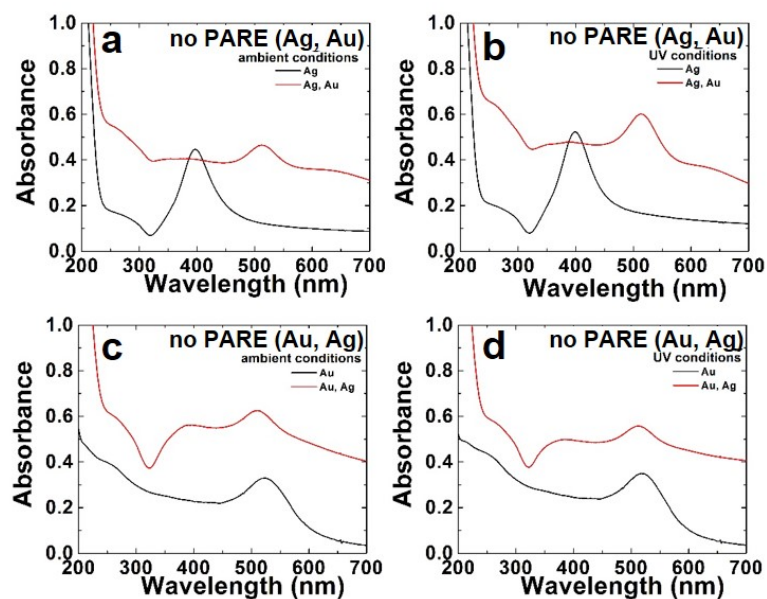


Figure 6.17. UV-vis spectra of no PARE control samples, prepared at the same concentration as the 2 ratio for the PARE samples. Part (a) corresponds to no PARE (Ag, Au) under ambient conditions while part (b) is the same under UV conditions. Part (c) shows no PARE (Au, Ag) under ambient conditions while part (d) is the same under UV conditions.

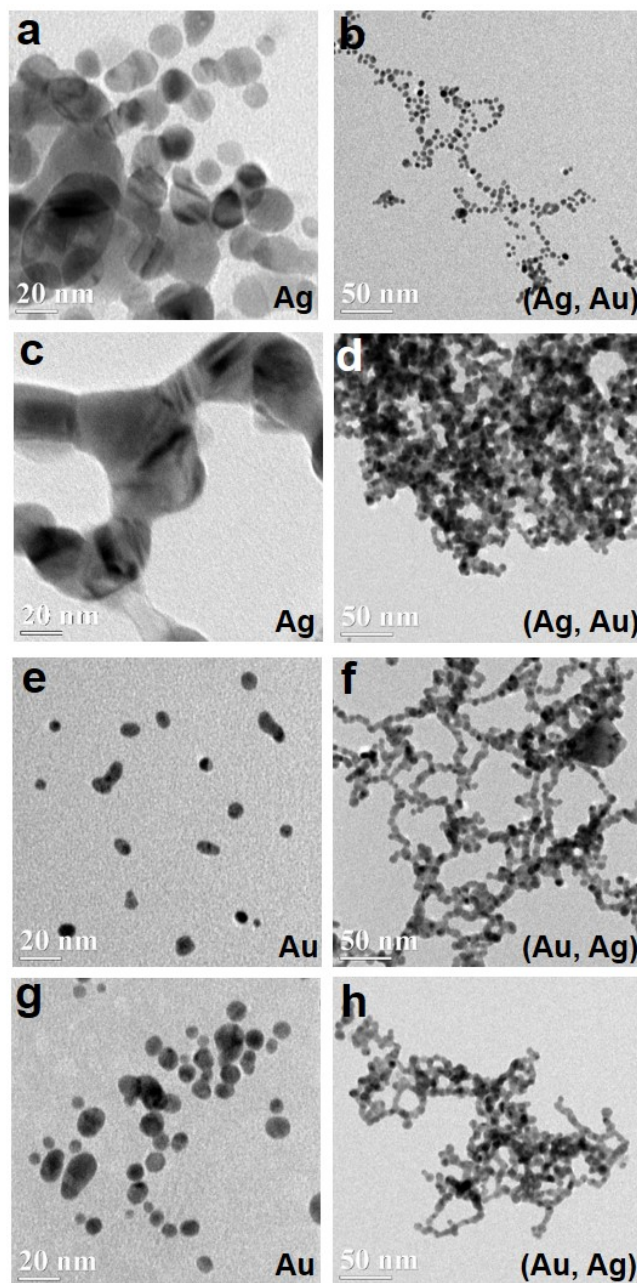


Figure 6.18. TEM of no PARE control samples. All samples were prepared at identical metal concentrations as the 2 ratio for the PARE assemblies. Part (a) is Ag under ambient conditions while (b) is (Ag, Au). Part (c) shows Ag under UV conditions while (d) is (Ag, Au). Part (e) is Au under ambient conditions while (f) is (Au, Ag). Part (g) shows Au under UV conditions while (h) is (Au, Ag).

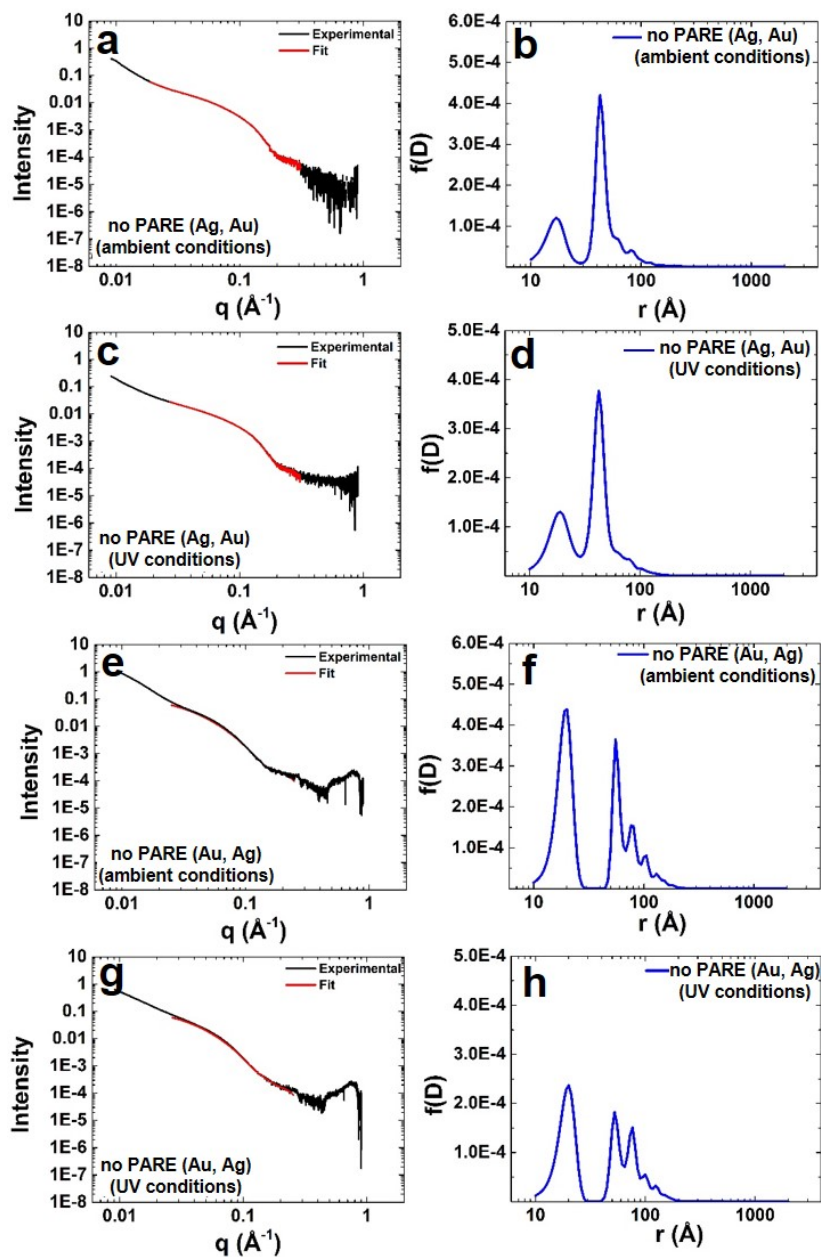


Figure 6.19. SAXS analysis of no PARE controls prepared at metal concentrations identical to the 2 ratio for the PARE samples. Parts (a, c, e and f) show the scattering with corresponding experimental fitting for no PARE controls while parts (b, d, f and h) are the extrapolated sizes from the fitting.

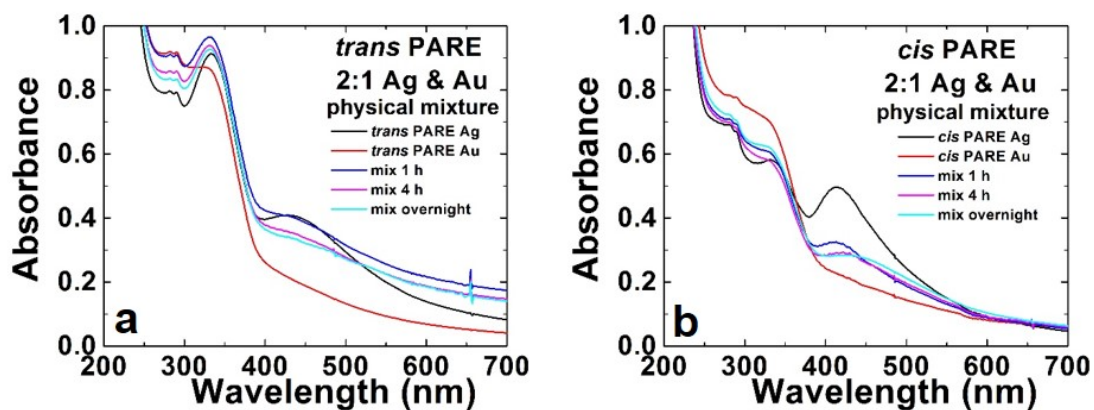


Figure 6.20. UV-vis spectra of physical mixture controls at metal:PARE ratio of 2. Part (a) shows the physical mixture of *trans* PARE Ag and *trans* PARE Au. Part (b) shows the physical mixture of *cis* PARE Ag and *cis* PARE Au.

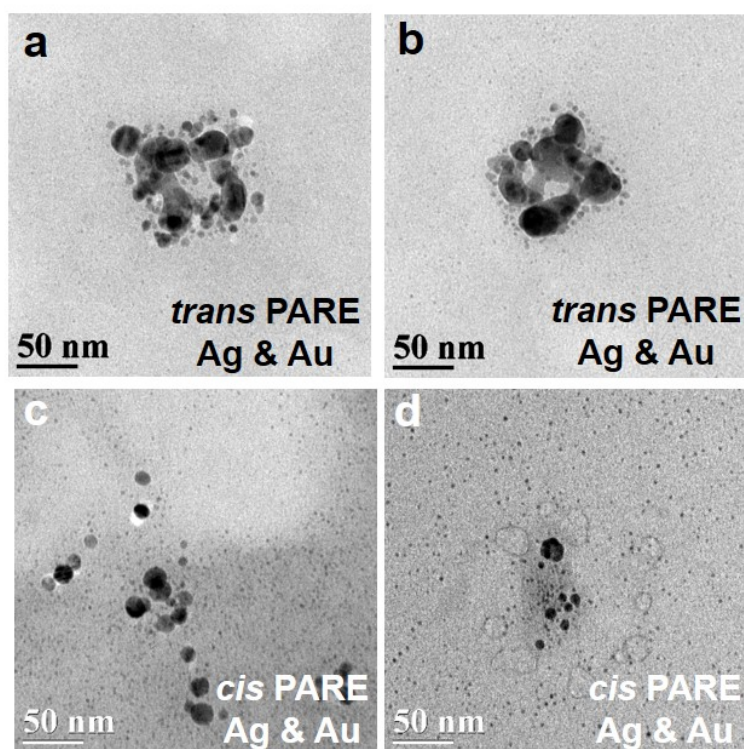


Figure 6.21. TEM images of physical mixture controls at a metal:PARE ratio of 2. Part (a) shows particles formed from the physical mixture of *trans* PARE Ag and *trans* PARE Au after 1 h while part (b) is overnight. Part (c) shows particles formed from the physical mixture of *cis* PARE Ag and *cis* PARE Au after 1 h while part (d) is overnight.

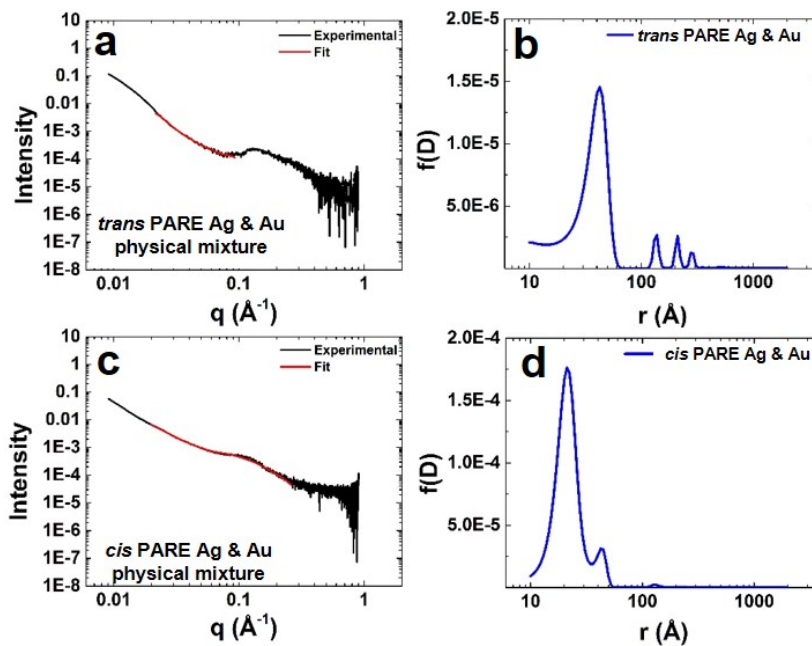


Figure 6.22. SAXS analysis of physical mixture control samples. All assemblies were prepared at a metal:PARE ratio of 2. Parts (a) and (c) show the scattering data and corresponding experimental fitting. Parts (b) and (d) show the size determined from the fitting.

References

1. Kröger, N.; Deutzmann, R.; Sumper, M., *Science* **1999**, *286*, 1129-1132.
2. Dickerson, M. B.; Sandhage, K. H.; Naik, R. R., *Chem. Rev.* **2008**, *108*, 4935-4978.
3. Sewell, S. L.; Wright, D. W., *Chem. Mater.* **2006**, *18*, 3108-3113.
4. Cole, K. E.; Ortiz, A. N.; Schoonen, M. A.; Valentine, A. M., *Chem. Mater.* **2006**, *18*, 4592-4599.
5. Sarikaya, M.; Tamerler, C.; Jen, A. K.-Y.; Schulten, K.; Baneyx, F., *Nat. Mater.* **2003**, *2*, 577-585.
6. Vodnik, M.; Zager, U.; Strukelj, B.; Lunder, M., *Molecules* **2011**, *16*, 790-817.
7. Narayanan, R.; El-Sayed, M. A., *Nano Lett.* **2004**, *4*, 1343-1348.
8. Narayanan, R.; El-Sayed, M. A., *Langmuir* **2005**, *21*, 2027-2033.
9. Pandey, R. B.; Heinz, H.; Feng, J.; Farmer, B. L.; Slocik, J. M.; Drummy, L. F.; Naik, R. R., *Phys. Chem. Chem. Phys.* **2009**, *11*, 1989-2001.
10. Chiu, C.-Y.; Li, Y.; Huang, Y., *Nanoscale* **2010**, *2*, 927-930.
11. Si, S.; Mandal, T. K., *Chem. Eur. J.* **2007**, *13*, 3160-3168.
12. Pacardo, D. B.; Sethi, M.; Jones, S. E.; Naik, R. R.; Knecht, M. R., *ACS Nano* **2009**, *3*, 1288-1296.
13. Coppage, R.; Slocik, J. M.; Briggs, B. D.; Frenkel, A. I.; Heinz, H.; Naik, R. R.; Knecht, M. R., *J. Am. Chem. Soc.* **2011**, *133*, 12346-12349.
14. Frenkel, A. I.; Nemzer, S.; Pister, I.; Soussan, L.; Harris, T.; Sun, Y.; Rafailovich, M. H., *J. Chem. Phys.* **2005**, *123*, 184701-184706.
15. Coppage, R.; Slocik, J. M.; Sethi, M.; Pacardo, D. B.; Naik, R. R.; Knecht, M. R., *Angew. Chem. Int. Ed.* **2010**, *49*, 3767-3770.
16. Pacardo, D. B.; Slocik, J. M.; Kirk, K. C.; Naik, R. R.; Knecht, M. R., *Nanoscale* **2011**, *3*, 2194-2201.
17. Pacardo, D. B.; Knecht, M. R., *Catal. Sci. Technol.* **2013**, *3*, 745-753.
18. Coppage, R.; Slocik, J. M.; Briggs, B. D.; Frenkel, A. I.; Naik, R. R.; Knecht, M. R., *ACS Nano* **2012**, *6*, 1625-1636.

19. Coppage, R.; Slocik, J. M.; Ramezani-Dakhel, H.; Bedford, N. M.; Heinz, H.; Naik, R. R.; Knecht, M. R., *J. Am. Chem. Soc.* **2013**, *135*, 11048-11054.
20. Janairo, J. I. B.; Sakaguchi, T.; Hara, K.; Fukuoka, A.; Sakaguchi, K., *Chem. Commun.* **2014**, *50*, 9259-9262.
21. Burda, C.; Chen, X.; Narayanan, R.; El-Sayed, M. A., *Chem. Rev.* **2005**, *105*, 1025-1102.
22. Bhandari, R.; Knecht, M. R., *ACS Catal.* **2011**, *1*, 89-98.
23. Jakhmola, A.; Bhandari, R.; Pacardo, D. B.; Knecht, M. R., *J. Mater. Chem.* **2010**, *20*, 1522-1531.
24. Chiu, C.-Y.; Li, Y.; Ruan, L.; Ye, X.; Murray, C. B.; Huang, Y., *Nat. Chem.* **2011**, *3*, 393-399.
25. Li, Y.; Huang, Y., *Adv. Mater.* **2010**, *22*, 1921-1925.
26. Ruan, L.; Chiu, C.-Y.; Li, Y.; Huang, Y., *Nano Lett.* **2011**, *11*, 3040-3046.
27. Forbes, L. M.; Goodwin, A. P.; Cha, J. N., *Chem. Mater.* **2010**, *22*, 6524-6528.
28. Bhandari, R.; Pacardo, D. B.; Bedford, N. M.; Naik, R. R.; Knecht, M. R., *J. Phys. Chem. C.* **2013**, *117*, 18053-18062.
29. Pacardo, D. B.; Ardman, E.; Knecht, M. R., *J. Phys. Chem. C* **2014**, *118*, 2518-2527.
30. Bedford, N. M.; Bhandari, R.; Slocik, J. M.; Seifert, S.; Naik, R. R.; Knecht, M. R., *Chem. Mater.* **2014**, *26*, 4082-4091.
31. Maity, I.; Rasale, D. B.; Das, A. K., *RSC Adv.* **2014**, *4*, 2984-2988.
32. Kelly, K. L.; Coronado, E.; Zhao, L. L.; Schatz, G. C., *J. Phys. Chem. B.* **2003**, *107*, 668-677.
33. Slocik, J. M.; Govorov, A. O.; Naik, R. R., *Nano Lett.* **2011**, *11*, 701-705.
34. Chen, C.-L.; Zhang, P.; Rosi, N. L., *J. Am. Chem. Soc.* **2008**, *130*, 13555--13557.
35. Chen, C.-L.; Rosi, N. L., *J. Am. Chem. Soc.* **2010**, *132*, 6902-6903.
36. Song, C.; Zhao, G.; Zhang, P.; Rosi, N. L., *J. Am. Chem. Soc.* **2010**, *132*, 14033-14035.
37. Song, C.; Blaber, M. G.; Zhao, G.; Zhang, P.; Fry, H. C.; Schatz, G. C.; Rosi, N. L., *Nano Lett.* **2013**, *13*, 3256-3261.

38. Zhang, C.; Song, C.; Fry, H. C.; Rosi, N. L., *Chem. Eur. J.* **2014**, *20*, 941-945.
39. Zhang, C.; Zhou, Y.; Merg, A.; Song, C.; Schatz, G. C.; Rosi, N. L., *Nanoscale* **2014**, *6*, 12328-12332.
40. Li, Y.; Tang, Z.; Prasad, P. N.; Knecht, M. R.; Swihart, M. T., *Nanoscale* **2014**, *6*, 3165-3172.
41. Bhandari, R.; Knecht, M. R., *Catal. Sci. Technol.* **2012**, *2*, 1360-1366.
42. de la Rica, R.; Chow, L. W.; Horejs, C.-M.; Mazo, M.; Chiappini, C.; Pashuck, E. T.; Bitton, R.; Stevens, M. M., *Chem. Commun.* **2014**, *50*, 10648-10650.
43. Kim, J.; Sadowsky, M. J.; Hur, H.-G., *Biomacromolecules* **2011**, *12*, 2518-2523.
44. Ray, S.; Das, A. K.; Banerjee, A., *Chem. Commun.* **2006**, 2816-2818.
45. Nam, K. T.; Lee, Y. J.; Krauland, E. M.; Kottmann, S. T.; Belcher, A. M., *ACS Nano* **2008**, *2*, 1480-1486.
46. Joly, S.; Kane, R.; Radzilowski, L.; Wang, T.; Wu, A.; Cohen, R. E.; Thomas, E. L.; Rubner, M. F., *Langmuir* **2000**, *16*, 1354-1359.
47. Lee, Y. J.; Yi, H.; Kim, W.-J.; Kang, K.; Yun, D. S.; Strano, M. S.; Ceder, G.; Belcher, A. M., *Science* **2009**, *324*, 1051-1055.
48. Dickerson, M. B.; Naik, R. R.; Stone, M. O.; Cai, Y.; Sandhage, K. H., *Chem. Commun.* **2004**, 1776-1777.
49. Carter, C. J.; Ackerson, C. J.; Feldheim, D. L., *ACS Nano* **2010**, *4*, 3883-3888.
50. Diamanti, S.; Elsen, A.; Naik, R.; Vaia, R., *J. Phys. Chem. C* **2009**, *113*, 9993-9997.
51. Hall Sedlak, R.; Hnilova, M.; Grosh, C.; Fong, H.; Baneyx, F.; Schwartz, D.; Sarikaya, M.; Tamerler, C.; Traxler, B., *Appl. Environ. Microbiol.* **2012**, *78*, 2289-2296.
52. Cha, J. N.; Shimizu, K.; Zhou, Y.; Christiansen, S. C.; Chmelka, B. F.; Stucky, G. D.; Morse, D. E., *Proc. Natl. Acad. Sci.* **1999**, *96*, 361-365.
53. Tomczak, M. M.; Gupta, M. K.; Drummy, L. F.; Rozenzhak, S. M.; Naik, R. R., *Acta Biomaterialia* **2009**, *5*, 876-882.
54. Liang, M.; Deschaume, O.; Patwardhan, S. V.; Perry, C. C., *J. Mater. Chem.* **2011**, *21*, 80-89.
55. Dickerson, M. B.; Jones, S. E.; Cai, Y.; Ahmad, G.; Naik, R. R.; Kröger, N.; Sandhage, K. H., *Chem. Mater.* **2008**, *20*, 1578-1584.

56. Fang, Y.; Poulsen, N.; Dickerson, M. B.; Cai, Y.; Jones, S. E.; Naik, R. R.; Kröger, N.; Sandhage, K. H., *J. Mater. Chem.* **2008**, *18*, 3871-3875.
57. Ahmad, G.; Dickerson, M. B.; Cai, Y.; Jones, S. E.; Ernst, E. M.; Vernon, J. P.; Haluska, M. S.; Fang, Y.; Wang, J.; Subramanyam, G.; Naik, R. R.; Sandhage, K. H., *J. Am. Chem. Soc.* **2008**, *130*, 4-5.
58. Umetsu, M.; Mizuta, M.; Tsumoto, K.; Ohara, S.; Takami, S.; Watanabe, H.; Kumagai, I.; Adschiri, T., *Adv. Mater.* **2005**, *17*, 2571-2575.
59. Nagaveni, K.; Hedge, M. S.; Ravishankar, N.; Subbanna, G. N.; Madras, G., *Langmuir* **2004**, *20*, 2900-2907.
60. Astruc, D., *Inorg. Chem.* **2007**, *46*, 1884-1894.
61. Ataee-Esfahani, H.; Wang, L.; Nemoto, Y.; Yamauchi, Y., *Chem. Mater.* **2010**, *22*, 6310-6318.
62. Stille, J. K., *Angew. Chem. Int. Ed. Engl.* **1986**, *25*, 508-524.
63. Espinet, P.; Echavarren, A. M., *Angew. Chem. Int. Ed.* **2004**, *43*, 4704-4734.
64. Ramezani-Dakhel, H.; Mirau, P. A.; Naik, R. R.; Knecht, M. R.; Heinz, H., *Phys. Chem. Chem. Phys.* **2013**, *15*, 5488-5492.
65. Calò, V.; Nacci, A.; Monopoli, A.; Montingelli, F., *J. Org. Chem.* **2005**, *70*, 6040-6044.
66. Fihri, A.; Bouhrara, M.; Nekoueishahraki, B.; Basset, J.-M.; Polshettiwar, V., *Chem. Soc. Rev.* **2011**, *40*, 5181-5203.
67. Miyaura, N.; Suzuki, A., *Chem. Rev.* **1995**, *95*, 2457-2483.
68. Smith, G. B.; Dezeny, G. C.; Hughes, D. L.; King, A. O.; Verhoeven, T. R., *J. Org. Chem.* **1994**, *59*, 8151-8156.
69. Phan, N. T. S.; Sluys, M. V. D.; Jones, C. W., *Adv. Synth. Catal.* **2006**, *348*, 609-679.
70. Amatore, C.; Le Duc, G.; Jutand, A., *Chem. Eur. J.* **2013**, *19*, 10082-10093.
71. Braga, A. A. C.; Morgon, N. H.; Ujaque, G.; Maseras, F., *J. Am. Chem. Soc.* **2005**, *127*, 9298-9307.
72. Carrow, B. P.; Hartwig, J. F., *J. Am. Chem. Soc.* **2011**, *133*, 2116-2119.
73. T. Crisp, G., *Chem. Soc. Rev.* **1998**, *27*, 427-436.
74. de Vries, J. G., *Dalton Trans.* **2006**, 421-429.

75. Ananikov, V. P.; Beletskaya, I. P., *Organometallics* **2012**, *31*, 1595-1604.
76. Balanta, A.; Godard, C.; Claver, C., *Chem. Soc. Rev.* **2011**, *40*, 4973-4985.
77. Zhao, P.; Feng, X.; Huang, D.; Yang, G.; Astruc, D., *Coord. Chem. Rev.* **2015**, *287*, 114-136.
78. Wunder, S.; Polzer, F.; Lu, Y.; Mei, Y.; Ballauff, M., *J. Phys. Chem. C* **2010**, *114*, 8814-8820.
79. Saha, S.; Pal, A.; Kundu, S.; Basu, S.; Pal, T., *Langmuir* **2010**, *26*, 2885-2893.
80. Diallo, A. K.; Ornelas, C.; Salmon, L.; Aranzaes, J. R.; Astruc, D., *Angew. Chem. Int. Ed.* **2007**, *46*, 8644-8648.
81. Reetz, M. T.; de Vries, J. G., *Chem. Commun.* **2004**, 1559-1563.
82. Briggs, B. D.; Pekarek, R. T.; Knecht, M. R., *J. Phys. Chem. C* **2014**, *118*, 18543-18553.
83. Crabtree, R. H., *The Organometallic Chemistry of the Transition Metals*. 3rd ed.; John Wiley & Sons, Inc.: New York, NY, 2001.
84. de Vries, J. G., *Dalton Trans.* **2006**, 421-429.
85. Ellis, P. J.; Fairlamb, I. J. S.; Hackett, S. F. J.; Wilson, K.; Lee, A. F., *Angew. Chem. Int. Ed.* **2010**, *49*, 1820-1824.
86. Narayanan, R.; El-Sayed, M. A., *J. Phys. Chem. B* **2004**, *108*, 8572-8580.
87. Narayanan, R.; El-Sayed, M. A., *J. Am. Chem. Soc.* **2003**, *125*, 8340-8347.
88. Lee, A. F.; Ellis, P. J.; Fairlamb, I. J. S.; Wilson, K., *Dalton Trans.* **2010**, *39*, 10473-10482.
89. Sanchez-Sanchez, C.; Orozco, N.; Holgado, J. P.; Beaumont, S. K.; Kyriakou, G.; Watson, D. J.; Gonzalez-Elipé, A. R.; Feria, L.; Fernández Sanz, J.; Lambert, R. M., *J. Am. Chem. Soc.* **2014**, *137*, 940-947.
90. Kanuru, V. K.; Kyriakou, G.; Beaumont, S. K.; Papageorgiou, A. C.; Watson, D. J.; Lambert, R. M., *J. Am. Chem. Soc.* **2010**, *132*, 8081-8086.
91. Sánchez-Sánchez, C.; Yubero, F.; González-Elipé, A. R.; Feria, L.; Sanz, J. F.; Lambert, R. M., *J. Phys. Chem. C* **2014**, *118*, 11677-11684.
92. Wang, F.; Li, C.; Sun, L.-D.; Wu, H.; Ming, T.; Wang, J.; Yu, J. C.; Yan, C.-H., *J. Am. Chem. Soc.* **2011**, *133*, 1106-1111.

93. Wang, F.; Li, C.; Chen, H.; Jiang, R.; Sun, L.-D.; Li, Q.; Wang, J.; Yu, J. C.; Yan, C.-H., *J. Am. Chem. Soc.* **2013**, *135*, 5588-5601.
94. Niu, Z.; Peng, Q.; Zhuang, Z.; He, W.; Li, Y., *Chem. Eur. J.* **2012**, *18*, 9813-9817.
95. Gaikwad, A. V.; Holuigue, A.; Thathagar, M. B.; ten Elshof, J. E.; Rothenberg, G., *Chem. Eur. J.* **2007**, *13*, 6908-6913.
96. Reetz, M. T.; Westermann, E., *Angew. Chem. Int. Ed.* **2000**, *39*, 165-168.
97. Bedford, N. M.; Ramezani-Dakhel, H.; Slocik, J. M.; Briggs, B. D.; Ren, Y.; Frenkel, A. I.; Petkov, V.; Heinz, H.; Naik, R. R.; Knecht, M. R., *ACS Nano* **2015**, *9*, 5082-5092.
98. Chan, W. C.; White, P. D., *Fmoc Solid Phase Peptide Synthesis: A Practical Approach*. Oxford University Press: New York, NY, 2000.
99. Newville, M., *J. Synchrotron Rad.* **2001**, *8*, 322-324.
100. Ilavsky, J.; Jemian, P. R., *J. Appl. Cryst.* **2009**, *42*, 347-353.
101. Heinz, H.; Lin, T.-J.; Mishra, R. K.; Emami, F. S., *Langmuir : the ACS journal of surfaces and colloids* **2013**, *29*, 1754-1765.
102. Heinz, H.; Vaia, R. A.; Farmer, B. L.; Naik, R. R., *J. Phys. Chem. C* **2008**, *112*, 17281-17290.
103. Ramezani-Dakhel, H.; Ruan, L. Y.; Huang, Y.; Heinz, H., *Adv. Funct. Mater.* **2015**, *25*, 1374-1384.
104. Zabinsky, S. I.; Rehr, J. J.; Ankudinov, A.; Albers, R. C.; Eller, M. J., *Phys. Rev. B* **1995**, *52*, 2995-3009.
105. Frenkel, A. I.; Hills, C. W.; Nuzzo, R. G., *J. Phys. Chem. B* **2001**, *105*, 12689-12703.
106. Sanchez, S. I.; Menard, L. D.; Bram, A.; Kang, J. H.; Small, M. W.; Nuzzo, R. G.; Frenkel, A. I., *J. Am. Chem. Soc.* **2009**, *131*, 7040-7054.
107. Behafarid, F.; Matos, J.; Hong, S.; Zhang, L.; Rahman, T. S.; Roldan Cuenya, B., *ACS Nano* **2014**, *8*, 6671-6681.
108. Thomas, J. M.; Raja, R., *Annu. Rev. Mater. Res.* **2005**, *35*, 315-350.
109. Beletskaya, I. P.; Cheprakov, A. V., *Chem. Rev.* **2000**, *100*, 3009-3066.
110. Slagt, V. F.; de Vries, A. H. M.; de Vries, J. G.; Kellogg, R. M., *Org. Process Res. Dev.* **2010**, *14*, 30-47.

111. Byers, P. K.; Canty, A. J.; Crespo, M.; Puddephatt, R. J.; Scott, J. D., *Organometallics* **1988**, *7*, 1363-1367.
112. Kirchhoff, J. H.; Netherton, M. R.; Hills, I. D.; Fu, G. C., *J. Am. Chem. Soc.* **2002**, *124*, 13662-13663.
113. Amatore, C.; Jutand, A.; Le Duc, G., *Chem. Eur. J.* **2011**, *17*, 2492-2503.
114. Martin, R.; Buchwald, S. L., *Acc. Chem. Res.* **2008**, *41*, 1461-1473.
115. Miura, M., *Angew. Chem. Int. Ed.* **2004**, *43*, 2201-2203.
116. Ornelas, C.; Diallo, A. K.; Ruiz, J.; Astruc, D., *Adv. Synth. Catal.* **2009**, *351*, 2147-2154.
117. Pérez-Lorenzo, M., *J. Phys. Chem. Lett.* **2012**, *3*, 167-174.
118. Xu, J.; Wilson, A. R.; Rathmell, A. R.; Howe, J.; Chi, M.; Wiley, B. J., *ACS Nano* **2011**, *5*, 6119-6127.
119. Miyaura, N., *J. Organomet. Chem.* **2002**, *653*, 54-57.
120. Henglein, A., *J. Phys. Chem. B* **2000**, *104*, 6683-6685.
121. Creighton, J. A.; Eadon, D. G., *J. Chem. Soc., Faraday Trans.* **1991**, *87*, 3881-3891.
122. Khalily, M. A.; Ustahuseyin, O.; Garifullin, R.; Genc, R.; Guler, M. O., *Chem. Commun.* **2012**, *48*, 11358-11360.
123. Sawoo, S.; Srimani, D.; Dutta, P.; Lahiri, R.; Sarkar, A., *Tetrahedron* **2009**, *65*, 4367-4374.
124. Mondal, M.; Bora, U., *Green Chem.* **2012**, *14*, 1873-1876.
125. Fihri, A.; Luart, D.; Len, C.; Solhy, C.; Chevrin, C.; Polshettiwar, V., *Dalton Trans.* **2011**, *40*, 3116-3121.
126. Dewar, M. J. S.; Jones, R., *J. Am. Chem. Soc.* **1967**, *89*, 2408-2410.
127. Butters, M.; Harvey, J. N.; Jover, J.; Lennox, A. J. J.; Lloyd-Jones, G. C.; Murray, P. M., *Angew. Chem. Int. Ed.* **2010**, *49*, 5156-5160.
128. Brady, J. E.; Russell, J. W.; Holum, J. R., *Chemistry Matter and Its Changes*. 3rd ed.; John Wiley & Sons, Inc.: New York, NY, 2000.
129. Darwent, B. d., *Bond Dissociation Energies in Simple Molecules*. U.S. Department of Commerce, National Bureau of Standards: Washington, DC, 1970.

130. Briggs, B. D.; Knecht, M. R., *J. Phys. Chem. Lett.* **2012**, *3*, 405-418.
131. Han, M. S.; Lytton-Jean, A. K. R.; Oh, B.-K.; Heo, J.; Mirkin, C. A., *Angew. Chem. Int. Ed.* **2006**, *45*, 1807-1810.
132. Huo, F.; Lytton-Jean, A. K. R.; Mirkin, C. A., *Adv. Mater.* **2006**, *18*, 2304-2306.
133. Nykypanchuk, D.; Maye, M. M.; van der Lelie, D.; Gang, O., *Nature* **2008**, *451*, 549-552.
134. Maye, M. M.; Nykypanchuk, D.; van der Lelie, D.; Gang, O., *J. Am. Chem. Soc.* **2006**, *128*, 14020-14021.
135. Hnilova, M.; Oren, E. E.; Seker, U. O. S.; Wilson, B. R.; Collino, S.; Evans, J. S.; Tamerler, C.; Sarikaya, M., *Langmuir* **2008**, *24*, 12440-12445.
136. Lévy, R.; Thanh, N. T. K.; Doty, R. C.; Hussain, I.; Nichols, R. J.; Schiffrin, D. J.; Brust, M.; Fernig, D. G., *J. Am. Chem. Soc.* **2004**, *126*, 10076-10084.
137. Flynn, C. E.; Mao, C.; Hayhurst, A.; Williams, J. L.; Georgiou, G.; Iverson, B.; Belcher, A. M., *J. Mater. Chem.* **2003**, *13*, 2414-2421.
138. Banerjee, I. A.; Yu, L.; Matsui, H., *J. Am. Chem. Soc.* **2005**, *127*, 16002-16003.
139. Tang, Z.; Palafox-Hernandez, J. P.; Law, W.-C.; Hughes, Z. E.; Swihart, M. T.; Prasad, P. N.; Knecht, M. R.; Walsh, T. R., *ACS Nano* **2013**, *7*, 9632-9646.
140. Palafox-Hernandez, J. P.; Tang, Z.; Hughes, Z. E.; Li, Y.; Swihart, M. T.; Prasad, P. N.; Walsh, T. R.; Knecht, M. R., *Chem. Mater.* **2014**, *26*, 4960-4969.
141. Saha, K.; Agasti, S. S.; Kim, C.; Li, X.; Rotello, V. M., *Chem. Rev.* **2012**, *112*, 2739-2779.
142. Bhandari, R.; Coppage, R.; Knecht, M. R., *Catal. Sci. Technol.* **2012**, *2*, 256-266.
143. Hvolbæk, B.; Janssens, T. V. W.; Clausen, B. S.; Falsig, H.; Christensen, C. H.; Nørskov, J. K., *Nano Today* **2007**, *2*, 14-18.
144. Rosi, N. L.; Mirkin, C. A., *Chem. Rev.* **2005**, *105*, 1547-1562.
145. Macfarlane, R. J.; Jones, M. R.; Lee, B.; Auyeung, E.; Mirkin, C. A., *Science* **2013**, *341*, 1222-1225.
146. Lee, K.-S.; El-Sayed, M. A., *J. Phys. Chem. B* **2006**, *110*, 19220-19225.
147. Brown, K. R.; Walter, D. G.; Natan, M. J., *Chem. Mater.* **2000**, *12*, 306-313.
148. Sau, T. K.; Murphy, C. J., *J. Am. Chem. Soc.* **2004**, *126*, 8648-8649.

149. Grzelczak, M.; Pérez-Juste, J.; Mulvaney, P.; Liz-Marzán, L. M., *Chem. Soc. Rev.* **2008**, *37*, 1783-1791.
150. LaMer, V. K.; Dinegar, R. H., *J. Am. Chem. Soc.* **1950**, *72*, 4847-4854.
151. Hostetler, M. J.; Wingate, J. E.; Zhong, C.-J.; Harris, J. E.; Vachet, R. W.; Clark, M. R.; Londono, J. D.; Green, S. J.; Stokes, J. J.; Wignall, G. D.; Glish, G. L.; Porter, M. D.; Evans, N. D.; Murray, R. W., *Langmuir* **1998**, *14*, 17-30.
152. Pradhan, N.; Pal, A.; Pal, T., *Colloid Surf. A* **2002**, *196*, 247-257.
153. Zeng, J.; Zhang, Q.; Chen, J.; Xia, Y., *Nano Lett.* **2010**, *10*, 30-35.
154. Cushing, B. L.; Kolesnichenko, V. L.; O'Connor, C. J., *Chem. Rev.* **2004**, *104*, 3893-3946.
155. Borsook, H.; Keighley, G., *Proc. Natl. Acad. Sci.* **1933**, *19*, 875-878.
156. Jana, N. R.; Gearheart, L.; Murphy, C. J., *Chem. Mater.* **2001**, *13*, 2313-2322.
157. Srisombat, L.; Jamison, A. C.; Lee, T. R., *Colloid Surf. A* **2011**, *390*, 1-19.
158. Shivhare, A.; Ambrose, S. J.; Zhang, H.; Purves, R. W.; Scott, R. W. J., *Chem. Commun.* **2013**, *49*, 276-278.
159. Crookes-Goodson, W. J.; Slocik, J. M.; Naik, R. R., *Chem. Soc. Rev.* **2008**, *37*, 2403-2412.
160. Daniel, M.-C.; Astruc, D., *Chem. Rev.* **2004**, *104*, 293-346.
161. Jones, M. R.; Osberg, K. D.; Macfarlane, R. J.; Langille, M. R.; Mirkin, C. A., *Chem. Rev.* **2011**, *111*, 3736-3827.
162. Kaur, P.; Maeda, Y.; Mutter, A. C.; Matsunaga, T.; Xu, Y.; Matsui, H., *Angew. Chem. Int. Ed.* **2010**, *49*, 8375-8378.
163. Park, S. Y.; Lytton-Jean, A. K. R.; Lee, B.; Weigand, S.; Schatz, G. C.; Mirkin, C. A., *Nature* **2008**, *451*, 553-556.
164. Zhang, Y.; Lu, F.; Yager, K. G.; van der Lelie, D.; Gang, O., *Nature Nanotech.* **2013**, *8*, 865-872.
165. Xu, X.; Rosi, N. L.; Wang, Y.; Huo, F.; Mirkin, C. A., *J. Am. Chem. Soc.* **2006**, *128*, 9286-9287.
166. Briggs, B. D.; Li, Y.; Swihart, M. T.; Knecht, M. R., *ACS Appl. Mater. Interfaces* **2015**, *7*, 8843-8851.
167. Slocik, J. M.; Naik, R. R., *Adv. Mater.* **2006**, *18*, 1988-1992.

168. Hnilova, M.; Liu, X.; Yuca, E.; Jia, C.; Wilson, B.; Karatas, A. Y.; Gresswell, C.; Ohuchi, F.; Kitamura, K.; Tamerler, C., *ACS Appl. Mater. Interfaces* **2012**, *4*, 1865-1871.
169. Tang, Z.; Lim, C.-K.; Palafox-Hernandez, J. P.; Drew, K. L. M.; Li, Y.; Swihart, M. T.; Prasad, P. N.; Walsh, T. R.; Knecht, M. R., *Submitted* **2015**.
170. Tamerler, C.; Oren, E. E.; Duman, M.; Venkatasubramanian, E.; Sarikaya, M., *Langmuir* **2006**, *22*, 7712-7718.
171. Bandara, H. M. D.; Burdette, S. C., *Chem. Soc. Rev.* **2012**, *41*, 1809-1825.
172. Nikoobakht, B.; Wang, Z. L.; El-Sayed, M. A., *J. Phys. Chem. B* **2000**, *104*, 8635-8640.
173. Sidhaye, D. S.; Kashyap, S.; Sastry, M.; Hotha, S.; Prasad, B. L. V., *Langmuir* **2005**, *21*, 7979-7984.